

TECHNISCHE UNIVERSITÄT MÜNCHEN

PHYSIK-DEPARTMENT

Studies on the top quark mass measurement in the all-hadronic $t\bar{t}$ decay channel with ATLAS

Dissertation

von

Paola Giovannini

CERN-THESIS-2011-069
14/07/2011



MAX-PLANCK-INSTITUT FÜR PHYSIK

WERNER-HEISENBERG-INSTITUT

TECHNISCHE UNIVERSITÄT MÜNCHEN

Max-Planck-Institut für Physik
(Werner-Heisenberg-Institut)

Studies on the top quark mass measurement in the all-hadronic $t\bar{t}$ decay channel with ATLAS

Paola Giovannini

Vollständiger Abdruck der von der Fakultät für Physik
der Technischen Universität München
zur Erlangung des akademischen Grades eines
Doktors der Naturwissenschaften (Dr. rer. nat.)
genehmigten Dissertation.

Vorsitzender: Univ.-Prof. Dr. A.J. Buras

Prüfer der Dissertation: 1. Hon.-Prof. Dr. S. Bethke

2. Univ.-Prof. Dr. St. Paul

Die Dissertation wurde am 05.05.2011
bei der Technischen Universität München eingereicht und
durch die Fakultät für Physik am 04.07.2011 angenommen.

*Finirai per trovarla la Via
se hai il coraggio di perderti.*

T.Terzani

Abstract

Prospects for measuring the top quark mass in the $t\bar{t}$ all-hadronic channel with the ATLAS detector are investigated. A robust analysis is developed on Monte Carlo simulations at $\sqrt{s} = 10$ TeV, considering 200 pb^{-1} of integrated luminosity. The event selection is based on a set of topological variables and on two b -tagged jets. The top quark mass is measured by a χ^2 fitting procedure on the reconstructed invariant mass distribution and the fit result is corrected for missing b -jet energy calibration. With a top quark mass of $m_t^{MC} = 172.5$ GeV as input to the simulation, the proposed method yields to a result of $m_t = 173.4 \pm 2.1|_{stat} \pm 7.3|_{sys}$ GeV for a typical pseudo-experiment. The main contribution to the systematic error comes from the jet energy scale uncertainty. Studies on the performance of the jet calibration method used, called Local Hadron Calibration, are performed both with Monte Carlo simulations and with first ATLAS data collected for pp collisions at $\sqrt{s} = 900$ GeV.

Acknowledgements

The research presented in this thesis was carried out at the MPI for Physics in Munich. Working at MPI was an incredibly enriching experience. I could join the IMPRS graduate school, which gave me the opportunity to be in close contact with the other MPI graduate students and to follow a very interesting programme of lectures and training courses. At the same time, this work was partially supported by the European Commission, through the ARTEMIS Research Training Network (contract number MRTN-CT-2006-035657). By being part of the ARTEMIS network I could meet scientists outside my home institute and collaborate with them. Moreover I could participate in international schools and in dedicated training events. I am very grateful for these opportunities of scientific and personal growth, which led to the completion of this PhD thesis. Among all the people that made this possible, I would like to especially thank a few.

I would like to thank my Supervisor, Prof. Dr. Siegfried Bethke, for having followed the development of my work very closely and for having helped me in taking the right direction in difficult moments.

I wish to thank my day-to-day Supervisor, Dr. Sven Menke, for having shared with me his innovative insight into physics. I very much appreciated our discussions, where I felt my point of view was always taken into deep consideration. I also cannot forget the many situations where he helped me with some magic computing potion, thanks!

I am grateful to Dr. Richard Nisius for his participation to the Advisory Panel meetings. I felt that he always tried to give the best suggestions for my career and for the quality of the thesis.

I would like to thank Dr. Giorgio Cortiana for having given me a lot of ideas and explanations on top physics. His experience with the top all-hadronic phenomenology was very precious to me.

I wish to thank all the ATLAS-HEC group members for their constant support. In particular I would like to thank Dr. Teresa Barillari for her warm welcome in Munich

and for her careful reading of the thesis.

I am very grateful to my officemates Gennady and Andreas for the very enjoyable time spent together. I owe a lot to Genna for all the times he helped me out of computing and calorimeter problems with patience and care. I would like to thank Andi for his collaboration on the top mass analysis and for all our discussions on physics, on philosophy or on economics, which widened my horizons. I also would like to thank him a lot for all the times he helped me with settling down in Germany. But mainly I would like to thank them both for having always been friends to me ... especially during the last year when it became much harder!

Finally I would like to thank all the MPI colleagues for making my staying at the institute so pleasant. In particular a big thanks goes to Sophio for being such a good friend, she introduced me most of the people and places that I know in Munich! I would also like to thank Silke and Maïke for having involved me in the organization of the various MPI public outreach events, collaborating with them was really interesting and enjoyable.

This work would not have been possible without my family and friends behind the scenes. I want to thank my mum for her unconditional support during these years. I know they have been hard for her, but she always stood at my side.

A big thanks goes as well to my cousin Raffy for her vital and enthusiastic support, which reached me even from so far away!

I want to thank my friends Mary and Rita for having encouraged me to look for the Unknown Island at the beginning of this journey. Thanks for having brought me here, for having come to visit at any occasion and for having kept listening to me as if we never lived apart a single day.

I'm happy now, because I'm not alone any longer in my journey. I want to thank Edo for having chosen to be part of this and of what will come.

Contents

Abstract	i
Acknowledgements	iii
Introduction	1
1 Top Quark Physics	5
1.1 The Standard Model	6
1.1.1 The Standard Model Lagrangian	7
1.1.2 Coupling Constants	11
1.1.3 Beyond the Standard Model	12
1.2 The Top Quark	15
1.2.1 Top Quark Production	16
1.2.2 Top Quark Decay	20
1.2.3 Top Quark Mass	21
1.3 Monte Carlo Generators	22
2 The ATLAS Experiment	25
2.1 The Large Hadron Collider	26
2.2 The ATLAS Detector	28
2.2.1 Magnetic System	30
2.2.2 Inner Detector	31
2.2.3 Calorimeters	32
2.2.4 Muon Spectrometer	36
2.2.5 Forward Detectors	37
2.2.6 Trigger System	38
2.3 Worldwide LHC Computing Grid	39

3	Jets and Calibration	43
3.1	Jet Algorithm	43
3.2	Particle showers	46
3.3	Cluster Algorithm	49
3.4	Jet Calibration	52
3.4.1	Global Calibration	54
3.4.2	Local Hadron Calibration	54
4	Local Hadron Calibration Studies	59
4.1	Resolution for nonlinear energy response	59
4.2	Monte Carlo performance studies for jets	63
4.2.1	Performance studies with the true particle jet	65
4.2.2	Performance studies with calibration hits	77
4.3	Monte Carlo performance studies for MET	85
4.4	Validation on ATLAS data	89
5	All-Hadronic Top Quark Mass	93
5.1	Monte Carlo samples	95
5.2	Event selection	97
5.2.1	Object reconstruction	97
5.2.2	Event selection	102
5.2.3	Trigger	107
5.3	Top quark reconstruction	109
5.3.1	Combinatorics	109
5.3.2	Top quark mass reconstruction	111
5.3.3	Background shape	115
5.4	Pseudo-experiments and fit	117
5.5	Systematic uncertainties	119
5.6	Results	128
	Conclusions	133
	Appendices	135
	A Derivation of resolution relations	137
	References	141

Introduction

Philosophical questions have inspired the development of human knowledge since antiquity. In our times, philosophy is strictly related to the development of natural sciences. In fact, in the past century, natural sciences have incredibly improved our understanding of nature and have radically changed our way of thinking¹. At the same time, science, via its practical application as technology, has strongly influenced the course of human history in the past century in a way that contemporary life cannot be conceived without technology anywhere in the world.

Physics can be seen as the queen of natural sciences, because it studies the fundamental laws of nature together with the global structure of the universe. The advancements in physics achieved during the past century have been extraordinary. Up to the end of the 19th century, physics was mainly an empirical science driven by experimental results, which could be explained with elegant and intuitive classical theories. Physics was deterministic and its concepts were somehow understandable in terms of common sense². From the beginning of the 20th century on, developments in physics have been more and more driven by a fruitful interplay of theory and experiments. The theories of the 20th century, as quantum mechanics, have introduced revolutionary concepts, as anti-matter or the uncertainty principle, to explain the fundamental laws of nature. These concepts, which from one hand are non-intuitive and disconnected from the day-to-day experience, have shown an incredible predictive power. In fact, the predictions of these theories have been tested in more and more sophisticated experiments.

In particular, from the second half of the past century on, a branch of physics, called particle physics, has developed as an interplay of quantum field theories and experiments based on nuclear and particle collisions. Particle physics concerns the study of the most fundamental building blocks of matter and their interactions. At the energies explored up to now, the fundamental building blocks of matter are considered

¹From Claude Lèvi-Strauss quotation in Chapter XVIII in [1].

²As discussed in detail in Chapter XVIII in [1].

to be quarks and leptons, whose interactions are described in terms of the Standard Model of particle physics.

In order to explore new energy regimes, the Large Hadron Collider (LHC) has been built during the last 10 years at CERN (the European Organisation for Nuclear Research). The LHC is the most powerful accelerator ever built, it produces proton-proton collisions at a design centre of mass energy of 14 TeV and with large instantaneous luminosity. The LHC has started stable operations in December 2009 and it is now functioning at a centre of mass energy of 7 TeV. Four particle detectors have been installed around the LHC collision points and among those ATLAS (A Toroidal LHC ApparatuS) is one of the two multipurpose detectors. The main aim of ATLAS is the search for the Higgs boson, which is the last missing particle predicted by the Standard Model theory, and the search for experimental evidences of new theories, which can resolve some of the problems of the Standard Model itself.

The work presented in this thesis concerns the study of the top quark mass in the $t\bar{t}$ all-hadronic channel. Studying the top quark is fundamental at the LHC, because it allows to test the precision of the Standard Model predictions and because it offers an insight into new physics, both as a background and as a possible decay product. The all-hadronic channel is very challenging, because of the high QCD multi-jet background rate, but it offers an unique opportunity to cross check the measurements performed in the $t\bar{t}$ semi and di-leptonic channels. The LHC can be considered a top quark factory, because of the high rate of top quark production expected at its centre of mass energy. Therefore most measurements of top quark properties will be soon limited by systematic uncertainty. For the top quark mass measurement, the largest uncertainty comes from the jet energy scale uncertainty. The study of jet calibration, in particular of the Local Hadron Calibration approach, together with the main sources of jet energy scale systematic uncertainty is the second topic of this thesis. The thesis is organised in five Chapters.

In Chapter 1 a brief description of the Standard Model of particle physics is given, together with a discussion on the main problems of the theory. Special focus is set on top quark physics. An introduction to Monte Carlo generators is provided as well.

In Chapter 2 the LHC machine and the ATLAS detector are described. A discussion on the principles underlying the design of ATLAS is given and each ATLAS sub-detector is presented in terms of the expected performance and of the technical specifications.

In Chapter 3 the concept of jet is introduced and different jet algorithms are de-

scribed. The process of jet reconstruction is explained, from the measurement of the calorimeter signal to the various approaches to jet calibration available in ATLAS. In particular the Local Hadron Calibration method is described in terms of cluster level and jet level corrections.

In Chapter 4 performance studies on the Local Hadron Calibration are presented. These studies are based on Monte Carlo simulations for collisions at 10 TeV centre of mass energy. The jet energy linearity and jet energy resolution achieved by the cluster level corrections are studied. For the evaluation of the resolution performance, the resolution is corrected for nonlinear energy effects, as described at the beginning of the Chapter and in Appendix A. Performance studies on the linearity achieved for Missing Transverse Energy reconstruction are included as well. Finally, validation studies on ATLAS data collected for collisions at $\sqrt{s} = 900$ GeV are presented.

In Chapter 5 the prospects for measuring the top quark mass in the $t\bar{t}$ all-hadronic channel with the ATLAS detector are investigated. The analysis presented is based on Monte Carlo simulations for collisions at 10 TeV centre of mass energy and 200 pb⁻¹ of integrated luminosity. The development of an event selection, based on a set of topological variables and on 2 b -tagged jets, is described together with the trigger efficiency for various trigger configurations. A study on combinatorics and on the top quark candidate selection criteria is performed. A χ^2 fitting procedure is developed on typical pseudo-experiment distributions of the top quark candidate invariant mass, in order to extract the measured top quark mass. The systematic uncertainty on this measurement is then evaluated with respect to various sources as jet energy and b -jet energy scale uncertainty and b -tagging efficiency uncertainty. The consistency of the result obtained is tested with respect to the true Monte Carlo top quark mass with the use of a pull distribution. Finally the result is corrected for a bias of the pull distribution due to the missing b -jet energy scale calibration.

The results achieved in the thesis are summarised in the Conclusions both for the studies on Local Hadron Calibration and for the top quark mass analysis.

Chapter 1

Top Quark Physics

Great advances in particle physics have been achieved in the last century. Many new ideas were developed successfully in quantum field theory to describe the strong, electromagnetic and weak interactions. In the late 1960's those ideas converged into a single theory, known as the Standard Model, which is extremely successful in describing a wide range of phenomena of elementary particles. However it is believed that the Standard Model is not the ultimate theory because it shows open problems, which should be solved in physics beyond the Standard Model. The search for evidences of this new physics is the most urgent issue for particle physics in the 21st century.

The top quark plays an important role in the Standard Model. Its existence was predicted since 1973 by Kobayashi and Maskawa, who extended the quark mixing matrix from two to three families, in order to incorporate CP violation into the Standard Model [2]. Because of its large mass the top quark was directly observed only in 1995 by the CDF and D0 experiments at TEVATRON [3,4]. It is a very interesting object to study, as input to precision electroweak analysis and as a possible exotic particle itself. Moreover the top quark may be useful to discover new particles, for example the Higgs boson couples most strongly to the top quark and could be produced in association with a top anti-top pair.

The purpose of this Chapter is to provide the theoretical framework to the studies presented in Chapters 4 and 5. In particular, an introduction to the Standard Model is given in Section 1.1. In Section 1.2 the top quark production and decay mechanism together with the definition of its mass are discussed. Finally Section 1.3 gives a description of the Monte Carlo generators used to simulate the Standard Model processes under investigation.

1.1 The Standard Model

Elementary particles are the most fundamental building blocks of matter. What has been called elementary changed in the course of the development of physics from atoms to nuclei and electrons, from nuclei to nucleons and finally to quarks. In our times quarks and leptons are considered elementary and they constitute all the known luminous matter in the universe. Six types (flavours) of quarks are known to exist: up u , down d , strange s , charm c , top t and bottom b . For quarks u , c and t the electric charge is $Q = 2/3e$, while for quarks d , s and b the electric charge is $Q = -1/3e$, where e is the elementary charge carried by a proton. Six types of leptons are known to exist: electron e , muon μ , tau τ , with $Q = -e$ and the corresponding neutrinos ν_e , ν_μ , ν_τ , with no electric charge. Quarks and leptons are spin 1/2 fermions. There are four fundamental interactions between elementary particles, which are mediated by integer spin bosons:

- electromagnetic interaction mediated by photons γ , with mass $m_\gamma = 0$, spin 1 and no electric charge;
- weak interaction mediated by the W^\pm and Z bosons, with masses $m_W = 80.4 \text{ GeV}/c^2$, $m_Z = 91.19 \text{ GeV}/c^2$, spin 1 and electric charge $\pm e$ for the W^\pm bosons and zero for the Z boson;
- strong interaction mediated by gluons g , with mass $m_g = 0$, spin 1 and no electric charge;
- gravitational interaction mediated by gravitons G , with mass $m_G = 0$, spin 2 and no electric charge.

At the energies explored up to now the gravitational interaction is negligible for particle physics, because it is extremely weak in comparison to the other interactions. All particles but photons and gluons experience the weak interaction and all electrically charged particles experience the electromagnetic interaction. Only quarks and gluons experience the strong interaction and thus possess colour charge. For each particle an antiparticle with opposite values of the quantum numbers (like the electric charge) exists. However some particles can be self-conjugate, in the sense that the particle and its antiparticle are the same. This can only happen for electrically neutral particles. Among the elementary particles of the Standard Model, the photon and the Z boson

are self-conjugate. Neutrinos are the only electrically neutral fermions and could be self-conjugate if they were Majorana particles, but this is still an open question [5,6].

The Standard Model describes the electromagnetic, weak and strong interactions among elementary particles (and antiparticles) by mean of quantum field theories, which combine quantum mechanics and special relativity. The Standard Model is based on the gauge group $SU(3)_C \times SU(2)_L \times U(1)_Y$. The product $SU(2)_L \times U(1)_Y$ is a symmetry with respect to the third component of the weak isospin T^3 and with respect to the weak hypercharge Y . It accounts for the electroweak interaction [7–10]. The group $SU(2)_L \times U(1)_Y$ is spontaneously broken into $U(1)_{em}$, via the so called Higgs mechanism [11–15]. $U(1)_{em}$ is a symmetry with respect to the electric charge $Q = T^3 + Y/2$ and accounts for the electromagnetic interaction alone. This was the first renormalizable quantum field theory proposed and is known as Quantum Electrodynamics (QED) [16,17]. $SU(3)_C$ is an unbroken symmetry with respect to the colour charge C and accounts for the strong interaction. This part of the Standard Model is known as Quantum Chromodynamics (QCD) [18–23].

1.1.1 The Standard Model Lagrangian

In the Standard Model, fermions are represented by fermion fields arranged in three generations of $SU(2)_L$ left-handed doublets and right-handed singlets. The three quark generations are:

$$\begin{aligned}
 1: & \quad \begin{pmatrix} u \\ d \end{pmatrix}_L, \quad u_R, \quad d_R, \\
 2: & \quad \begin{pmatrix} c \\ s \end{pmatrix}_L, \quad c_R, \quad s_R, \\
 3: & \quad \begin{pmatrix} t \\ b \end{pmatrix}_L, \quad t_R, \quad b_R,
 \end{aligned} \tag{1.1}$$

and the three lepton generations are:

$$\begin{aligned}
 1: & \quad \begin{pmatrix} \nu_e \\ e \end{pmatrix}_L, \quad e_R, \\
 2: & \quad \begin{pmatrix} \nu_\mu \\ \mu \end{pmatrix}_L, \quad \mu_R, \\
 3: & \quad \begin{pmatrix} \nu_\tau \\ \tau \end{pmatrix}_L, \quad \tau_R,
 \end{aligned} \tag{1.2}$$

where, for a generic field, $\psi_{L,R} = \frac{1}{2}(1 \mp \gamma_5)\psi$. The neutrinos are considered to be massless and thus have no right-handed component. It is possible to introduce a more compact notation:

$$Q_L^i = \begin{pmatrix} u^i \\ d^i \end{pmatrix}_L, \quad u_R^i, \quad d_R^i \quad (i = 1, 2, 3), \quad (1.3)$$

where the index i indicates the generation, so $u^1 = u$, $d^1 = d$, $u^2 = c$ and so on. In the same way, for the leptons:

$$L_L^i = \begin{pmatrix} \nu^i \\ e^i \end{pmatrix}_L, \quad e_R^i, \quad (i = 1, 2, 3). \quad (1.4)$$

Once the gauge symmetries and the fields are specified, the Lagrangian of the Standard Model is fixed by requiring it to be gauge invariant, local and renormalizable. It can be written as a sum of 4 terms [24], [25]:

$$\mathcal{L}_{SM} = \mathcal{L}_{Gauge} + \mathcal{L}_{Matter} + \mathcal{L}_{Higgs} + \mathcal{L}_{Yukawa}. \quad (1.5)$$

The term \mathcal{L}_{Gauge} accounts for the kinetic energy of the gauge fields and their self-interactions:

$$\mathcal{L}_{Gauge} = \frac{1}{2g_s^2} \text{Tr} G^{\mu\nu} G_{\mu\nu} + \frac{1}{2g^2} \text{Tr} F^{\mu\nu} F_{\mu\nu} - \frac{1}{4g'^2} B^{\mu\nu} B_{\mu\nu}, \quad (1.6)$$

where g_s , g and g' are the gauge couplings of the three gauge interactions. $G^{\mu\nu}$, $F^{\mu\nu}$ and $B^{\mu\nu}$ are the field strength tensors of the gluon, weak and hypercharge boson fields. In particular, there are 8 gauge boson fields G_μ^i $i = 1 \dots 8$ associated with $SU(3)_C$, 3 gauge boson fields A_μ^i $i = 1 \dots 3$ associated with $SU(2)_L$ and 1 gauge boson field B_μ associated with $U(1)_Y$. The term \mathcal{L}_{Matter} contains the kinetic energy of the fermions and their interactions with the gauge fields:

$$\mathcal{L}_{Matter} = \sum_{i=1}^3 i \bar{Q}_L^i \not{D} Q_L^i + i \bar{u}_R^i \not{D} u_R^i + i \bar{d}_R^i \not{D} d_R^i + i \bar{L}_L^i \not{D} L_L^i + i \bar{e}_R^i \not{D} e_R^i, \quad (1.7)$$

where $\not{D} = \gamma^\mu D_\mu$ and D_μ is the gauge covariant derivative. The Lagrangian terms \mathcal{L}_{Gauge} and \mathcal{L}_{Matter} do not contain mass terms for the fermion fields, because a mass term would connect the L_L and e_R fields and thus violate the $SU(2)_L \times U(1)_Y$ in-

variance. The Lagrangian terms written so far contain only 3 parameters g_s , g and g' .

The mechanism of electroweak symmetry breaking generates the masses of the gauge bosons and fermions without breaking gauge invariance. In the Standard Model, electroweak symmetry breaking is achieved by introducing another field into the model, the Higgs field ϕ . In the simplest (minimal) model the field is represented by an $SU(2)$ doublet of 2 complex scalar fields:

$$\phi = \begin{pmatrix} \phi^+ \\ \phi^0 \end{pmatrix}. \quad (1.8)$$

The \mathcal{L}_{Higgs} term of the Standard Model Lagrangian contains the kinetic energy, potential and gauge interaction of the Higgs field:

$$\mathcal{L}_{Higgs} = (D^\mu \phi)^\dagger D_\mu \phi + \mu^2 \phi^\dagger \phi - \lambda (\phi^\dagger \phi)^2, \quad (1.9)$$

where D_μ is the gauge covariant derivative and the remaining terms represent the negative of the Higgs potential. The potential with positive λ and positive μ^2 has a set of minima at the values of ϕ determined by:

$$\phi^\dagger \phi = \frac{v^2}{2}, \quad \text{with } v = \sqrt{\frac{\mu^2}{\lambda}}. \quad (1.10)$$

Spontaneous symmetry breaking occurs when the scalar doublet ϕ develops the vacuum expectation value:

$$\langle 0 | \phi | 0 \rangle = \begin{pmatrix} 0 \\ v/\sqrt{2} \end{pmatrix}. \quad (1.11)$$

It is convenient to parametrize the scalar doublet ϕ in terms of the fields denoting the shifts from the vacuum state $\langle 0 | \phi | 0 \rangle$:

$$\phi = e^{i\vec{\tau} \cdot \vec{\xi}/2v} \begin{pmatrix} 0 \\ (v + H)/\sqrt{2} \end{pmatrix}, \quad (1.12)$$

where the real scalar fields ξ_i $i = 1 \dots 3$ represent the Goldstone bosons and the real scalar field H represents the Higgs boson. The last term of the Standard Model La-

grangian \mathcal{L}_{Yukawa} contains the interaction of the Higgs field with the fermions:

$$\mathcal{L}_{Yukawa} = -\Gamma_u^{ij} \bar{Q}_L^i \epsilon \phi^* u_R^j - \Gamma_d^{ij} \bar{Q}_L^i \phi d_R^j - \Gamma_e^{ij} \bar{L}_L^i \phi e_R^j + h.c. \quad (1.13)$$

where ϵ is the total anti-symmetric tensor in 2 dimension, and the $\Gamma_{u,d,e}$ are complex matrices that contain most of the parameters of the Standard Model.

In order to make the physical content of the theory manifest, the Lagrangian of the Standard Model is rewritten in the unitary gauge, where the three Goldstone bosons disappear and the physical particle spectra become apparent. In the unitary gauge, the electroweak boson fields and their masses can be identified as:

$$W_\mu^\pm = \frac{A_\mu^{1'} \mp A_\mu^{2'}}{\sqrt{2}}, \text{ with mass } m_W = \frac{1}{2} g v, \quad (1.14)$$

for the neutral fields :

$$\begin{pmatrix} Z_\mu \\ P_\mu \end{pmatrix} = \begin{pmatrix} \cos \theta_W & -\sin \theta_W \\ \sin \theta_W & \cos \theta_W \end{pmatrix} \begin{pmatrix} A_\mu^{3'} \\ B_\mu' \end{pmatrix}, \quad (1.15)$$

$$\text{with masses} \quad m_Z = \frac{1}{2} v \sqrt{g^2 + g'^2} \quad m_P = 0,$$

where $A_\mu^{i'}$ and B_μ' are the $SU(2)_L$ and $U(1)_Y$ boson fields in the unitary gauge, W_μ^\pm and Z_μ are the weak interaction boson fields, P_μ is the photon boson field and θ_W is the weak mixing angle. Finally, the mass of the physical Higgs boson H is:

$$m_H = \sqrt{2\mu^2}. \quad (1.16)$$

In order to identify the masses of the quarks, it is necessary to diagonalize the quark mass matrix. The quark eigenstates for which the mass matrix is diagonal are connected to the flavour quark states via the Cabibbo Kobayashi Maskawa (CKM) matrix [2, 26]. This process is known as flavour mixing and is the mechanism that explains CP violation. The diagonalization doesn't have the same effect in the lepton sector, because the rotation can always be reabsorbed if the neutrinos are massless.

Neutrinos were considered massless in the original formulation of the Standard Model, but recent experiments with solar, atmospheric, reactor and accelerator neutrinos have provided evidences for neutrino oscillations. This phenomena can be explained in terms of nonzero neutrino masses and neutrino mixing [5]. The question is still open

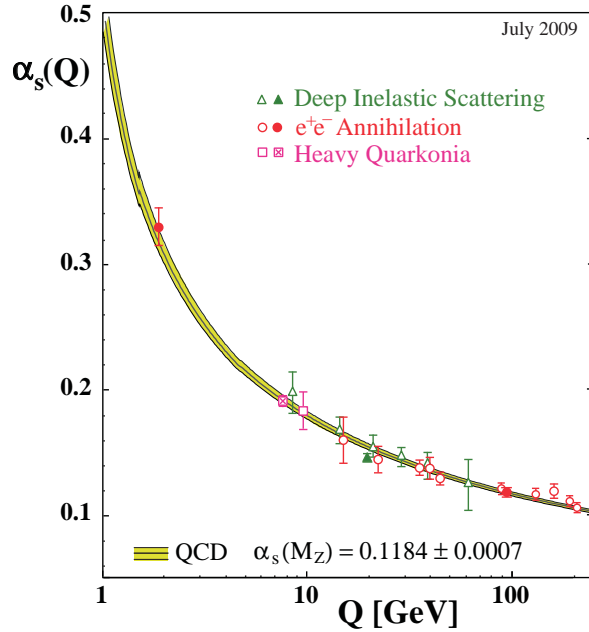


Figure 1.1: Summary of measurements of α_s as a function of the momentum transfer Q , in comparison with QCD predictions (yellow bands) [27].

if the massive neutrinos are of Dirac or of Majorana nature. Nevertheless, in the case of massive neutrinos, similar effects, like flavour mixing and CP violation, can emerge in the lepton sector as in the quark sector.

The mechanism of electroweak symmetry breaking is the only aspect of the Standard Model that has not yet been fully verified experimentally. The missing piece is the discovery of the Higgs boson particle, that is one of the main goals of the LHC experiments, as discussed in Chapter 2.

1.1.2 Coupling Constants

In the framework of the Standard Model it is possible to calculate the transition probability for the interaction between elementary particles. The calculation starts from non-interactive fields, which represent the incoming and outgoing particles. The interaction is described in terms of perturbation theory, as a sum of each possible interaction history over all possible intermediate particle states. This sum can be written as a sum of Feynman diagrams: to each diagram corresponds a prescription (Feynman rule) for calculating the amplitude from the Lagrangian. The terms of the perturbation theory sum are of increasing orders in the parameter α . If $\alpha \ll 1$ only the lower terms are

significant and the higher order effects can be neglected. In the Standard Model case the parameters of the expansions are correlated to the coupling constants g , g' and g_s , whose values depend on the momentum transfer squared Q^2 of the interaction. This effect is known as running coupling constant and has been experimentally measured in terms of

$$\alpha_{em} = \frac{1}{4\pi} \frac{g^2 g'^2}{g^2 + g'^2} \quad \text{and} \quad \alpha_s = \frac{g_s^2}{4\pi} \quad (1.17)$$

from which it is possible to determine the value of the gauge couplings g , g' and g_s , providing that the weak angle θ_w (for which $\tan \theta_w = g'/g$) is measured as well. The coupling α_{em} refers to the electromagnetic interaction and the coupling α_s to the strong interaction. In the framework of perturbation theory, it is possible to calculate the coupling constant dependence on Q^2 . The value of α_{em} decreases with decreasing Q^2 , or decreases with increasing distance: this effect is intuitively explained in terms of the charge screening from the virtual electron-positron pairs that surround a bare charge. The value of α_s shows the opposite behaviour, it decreases with increasing Q^2 , so it becomes larger at large distances. The dependence of α_s on Q^2 is shown in Figure 1.1 for both experimental data and theory. In summary, for large values of Q^2 , α_s becomes small and the strong interaction can be treated perturbatively. In this regime, called asymptotic freedom, quarks and gluons behave as free particles. On the other hand, for small Q^2 , α_s becomes large and the perturbative calculation cannot be justified: because of the large coupling constant, quarks and gluons are confined into bound states, called hadrons.

Experimentally quarks and gluons cannot be observed as free particles, but only in terms of hadrons or bunches of hadrons, generically called jets. Jets give an insight into the fascinating world of QCD. They are the central object of study for this thesis: jet reconstruction and calibration are discussed in Chapter 3 and 4 and subsequently jets are used as the main ingredient of the top quark mass studies discussed in Chapter 5.

1.1.3 Beyond the Standard Model

The Standard Model describes the elementary particles and their interactions down to $\sim 10^{-16}$ cm. With the exception of the Higgs sector, the consistency between theory and experiment has been verified up to a 0.1% precision. However the theory is too arbitrary to be considered the ultimate theory. In fact, the minimal version of the

model has 20 parameters and other 7 (9) for massive Dirac (Majorana) neutrinos. More in detail, the Standard Model is affected by a number of different problems [28].

The dark matter problem The Standard Model can not provide the cold dark matter necessary to explain the formation of large structures in the early universe, because its dark matter candidates, the neutrinos, are relativistic particles. An attractive solution to this problem is the existence of Weakly Interactive Massive Particles, that could be associated to Supersymmetric models or Little Higgs models or Extra Dimensions models.

The baryon asymmetry problem Even if the measured CP violation is well described by the CKM matrix mechanism, this is not sufficient to account for the baryon asymmetry in the universe. Almost any model for physics beyond the Standard Model is likely to lead to new sources of CP violation.

The gravity problem Gravity cannot be integrated with the other interactions in the Standard Model, because it cannot be described in terms of quantum field theory. Even if it is possible to combine the Standard Model with the classical theory of general relativity, the latter is not a quantum theory. In general, relativistic quantum mechanical theories of gravity have shown to be not renormalizable. Possible solutions are String and Superstring models.

The gauge symmetry problem The Standard Model is built on a complicated symmetry group $SU(2)_L \times U(1)_Y \times SU(3)_C$ and provides no explanation of why only the electroweak part of the theory is chiral (distinguishes between left-handed and right-handed fermions). This structure suggests the existence of some underlying unification of interactions, which would be realised in a Superstring theory or in a Grand Unified theory.

The fermion problem All matter under ordinary conditions can be built out of the fermions of the first family (e , ν_e , u and d). Experimentally three families of fermions have been discovered, but the Standard Model gives no explanation of the existence of the heavier families nor any prediction on their number nor on the fermion masses. Many of these questions could find an answer in String theory models, even if there is yet no compelling model or detailed prediction.

The hierarchy problem The Standard Model is presumably the effective theory of some larger theory that includes new physics at a scale Λ . For example, if the

new physics is gravity, then Λ is of the order of the Plank scale $\sim 10^{19}$ GeV. The renormalized Higgs mass, as calculated in the new theory, will include loop corrections of the order of Λ^2 . Because the Higgs mass is constrained to be much smaller ($m_H \ll 700$ GeV) with respect to the scale Λ , fine-tuning is expected to cancel out the loop corrections. One solution to the problem is TeV scale Supersymmetry, for which fermion and boson loop corrections cancel, leaving out some smaller effects. There are as well non-supersymmetric models in which fermion and boson loops cancel, like the Little Higgs models and Twin-Higgs models. Another possibility is to replace the Higgs mechanism with a dynamical symmetry breaking mechanism, as for the Technicolor, Top-colour and Composite Higgs models. Large Extra Dimensions models can also solve these difficulties.

The strong CP problem The QCD Lagrangian allows for an extra term that would break P, T , and CP symmetries. Because none of these violations have been observed yet, the coefficient for the Lagrangian term, θ_{QCD} , is extremely small. This implies fine-tuning cancellations to appear in the calculation of θ_{QCD} . A possible solution is the introduction of an extra global $U(1)$ symmetry, in a way that θ_{QCD} is a dynamical variable that is 0 at the minimum of the potential. This is the so called Peccei-Quinn mechanism that predicts the existence of axions.

Many of the possible extensions of the Standard Model predict experimental signatures detectable at the LHC [29, 30]. For example, models that offer dark matter candidates, as Supersymmetry with R-parity conservation, predict signatures with large missing transverse momentum in the final state. Several models predict the existence of heavy partners of Standard Model particles, generally referred to as W' , Z' or t' . This is the case in Little Higgs, Grand Unified theories, Technicolor or Extra Dimensions models (where the new particles are Kaluza-Klein excitations). Finally, possible scenarios in Extra Dimensions models predict that gravity can become strong at the TeV scale and that microscopic black holes can be produced at the LHC. These would be short-lived and decay rapidly through thermal (Hawking) radiation emitting high energy particles.

This summary does not pretend to be a comprehensive discussion of the Standard Model limitations and its possible extensions. Instead it wants to simply give an idea of the enormous range of possibilities for physics beyond the Standard Model that are opening up in particle physics. This is an incredible exciting moment, waiting for the LHC answer on which is the one actually realised in Nature.

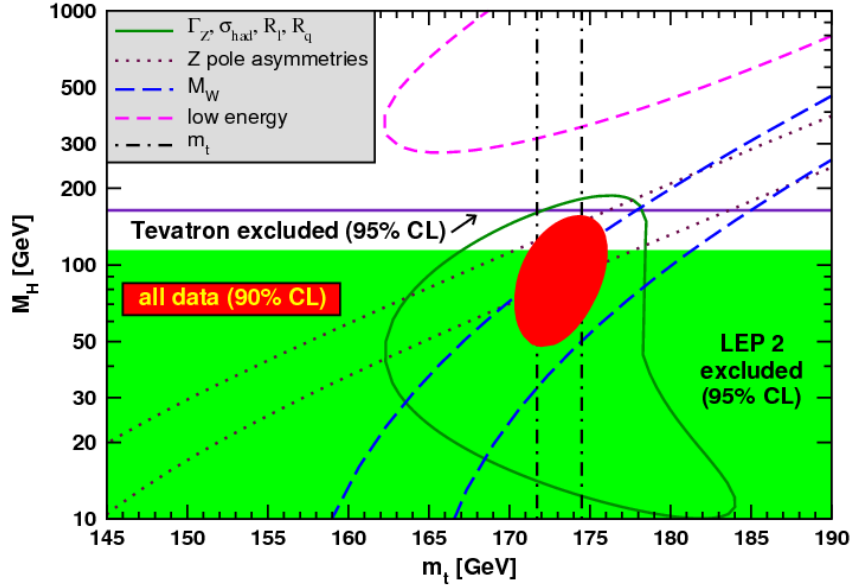


Figure 1.2: One-standard-deviation (39.35 %) uncertainties in m_H as a function of m_t for various inputs, and the 90 % CL region allowed by all data [31].

1.2 The Top Quark

The top quark is a very interesting and worthwhile object to study. Because of its relatively recent discovery, it is less well studied than the other quarks and leptons. For example the electric charge of the top quark has not yet been measured, leaving open the possibility that the observed particle is some type of exotic particle with electric charge else than $2/3e$. However this scenario is already excluded at a 92% CL [32]. At the LHC, it is expected that the top quark electric charge can be measured with a precision of 10% [31].

On the other hand, thanks to the success of perturbative calculations, it has been possible to predict with good accuracy the value of the top quark mass, before its discovery. This is because, in the Standard Model, the top quark contributes to the calculation of the W mass with a one loop correction that is proportional to the top quark mass squared m_t^2 . Instead the Higgs boson gives a one loop correction that is proportional only to the logarithm of the Higgs boson mass squared m_H^2 [25]. The weak dependence of the one loop corrections on the unknown Higgs boson mass allows for a very precise top mass prediction $m_t = 179^{+12}_{-7.8}$ GeV, that is well in agreement with the measured world average value $m_t = 172 \pm 0.9 \pm 1.3$ GeV [5]. On the other hand, a

precise measurement of the top quark mass and of the W boson mass can be used to predict the Higgs boson mass. In Figure 1.2 the relation between the uncertainty on m_H and m_t is shown for various inputs and the 90 % confidence level region is drawn taking all data into account [5]. In this respect, a further precision improvement in the top quark mass measurement would be a precious input to the electroweak precision analyses.

The top quark is by far the heaviest of all quarks. Because it has the largest coupling to the Higgs boson, it is possible to speculate that it could play a role in the mechanism of electroweak symmetry breaking. But even if the top quark turned out to be a Standard Model particle, the consequences of its large mass and its short lifetime are interesting by its own, as discussed in Sections 1.2.2 and 1.2.3.

The top quark is involved in many ways in searches for physics beyond the Standard Model. Top quarks can appear in the decay chain of new physics particles, as supersymmetric particles, and be used for inclusive searches. At the same time, the top quark itself can decay into a new particle, if its mass m_N is smaller than m_t . This is the case, for example, of the supersymmetric charged Higgs boson search via the process $t \rightarrow bH^+$. Finally, Standard Model events containing the top quark are background for almost all new physics searches, so precise understanding of the top signal is crucial to claim discoveries.

1.2.1 Top Quark Production

The production of top quarks at hadron colliders is described in terms of the so called factorisation theorem. The phenomenology of hadron collisions can be separated into a short distance process, called hard scattering, and into a long distance part. The hard scattering is the result of the interactions between quarks and gluons (called partons all together), which form the incoming hadrons. The long distance part is the actual modelling of the constituents of the colliding hadrons and it is independent of the hard scattering. The hard scattering is described by a partonic cross section $\sigma^{ij \rightarrow ab}$ for the interaction of partons i and j leading to the final state particles a and b and can be calculated in perturbation theory. The modelling of the hadron is described by a Parton Distribution Function (PDF) $f_i(x, \mu_F^2)$, which is the probability density to observe a parton i , with momentum fraction x in the incoming hadron, when probed at a scale μ_F^2 . The description of how partons are distributed into hadrons is out of the regime of perturbative calculation, so PDFs have to be extracted from data, using

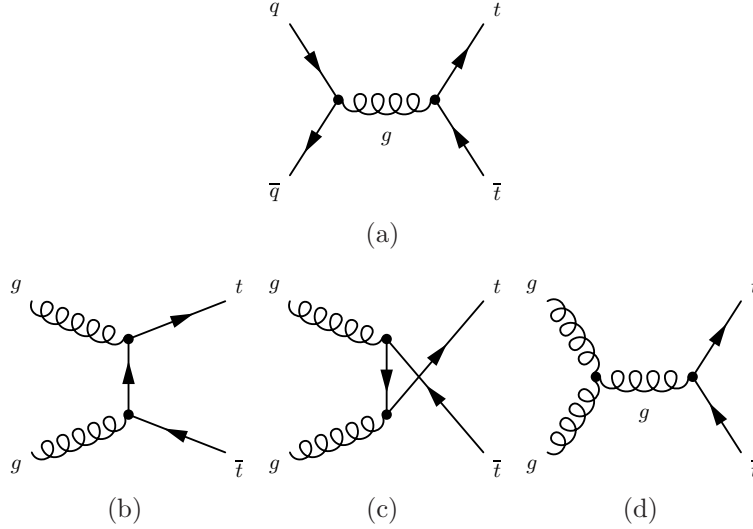


Figure 1.3: Leading order processes for $t\bar{t}$ production via strong interactions through quark-antiquark annihilation (a) and gluon fusion (b), (c), (d).

complex fits to deep-inelastic scattering and QCD measurements. In general, the total production cross section for the final state particles a and b can be written as [5]:

$$\sigma(\sqrt{s})^{pp \rightarrow ab} = \sum_{i,j=q,\bar{q},g} \int dx_1 dx_2 f_i(x_1, \mu^2) f_j(x_2, \mu^2) \sigma^{ij \rightarrow ab}(x_1 x_2 s, \alpha(\mu^2), \mu^2) \quad (1.18)$$

where \sqrt{s} is the centre of mass energy of the hadron collision and α is the coupling constant for the partonic process. In Equation 1.18 the renormalization scale μ_R and the factorisation scale μ_F are chosen to be equal $\mu \equiv \mu_F \equiv \mu_R$. If the final state particles a or b are top quarks, the partonic cross section depends as well on the top quark mass squared m_t^2 .

Top quarks at hadron colliders are mainly produced in $t\bar{t}$ pairs via the strong interaction through quark-antiquark annihilation or gluon fusion. The leading order Feynman diagrams for these processes are shown in Figure 1.3. In order to have a $t\bar{t}$ pair production, the typical minimum value of the momentum fraction x for the interacting partons is $x_{min} \approx 2m_t/\sqrt{s}$. This corresponds to $x_{min} = 0.18$ at the TEVATRON and to $x_{min} = 0.025$ at the LHC ($\sqrt{s} = 14$ TeV). For the different types of partons, the proton PDF parameterization from the CTEQ collaboration is shown in Figure 1.4. From this distribution it is possible to appreciate that, at the typical x values for the LHC, gluon initiated processes dominate ($\sim 90\%$) with respect to quark-antiquark annihilation processes ($\sim 10\%$). On the other hand, at the typical x values for the

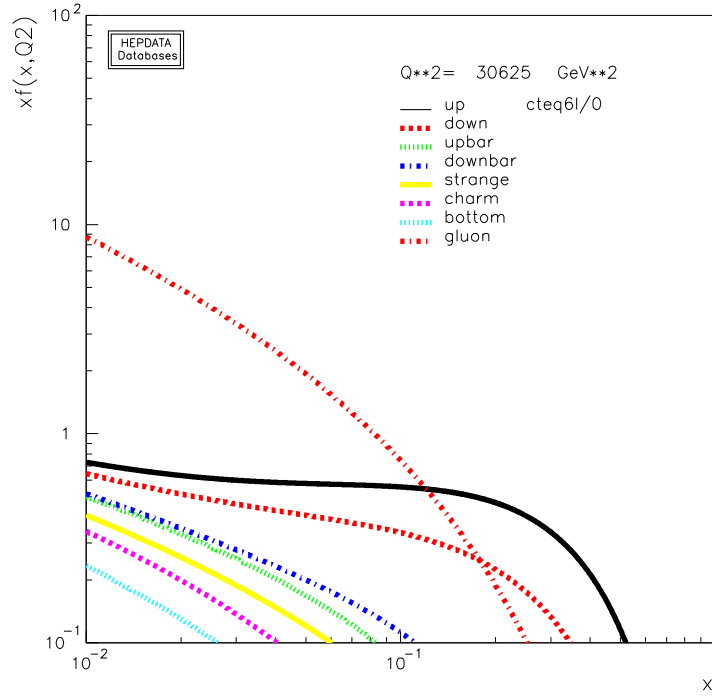


Figure 1.4: The quarks, antiquarks and gluon momentum densities in the proton as a function of the longitudinal proton momentum fraction x , for the scale relevant to top quark production $Q^2 = m_t^2$ with $m_t = 175$ GeV, from the CTEQ6 parameterization [33, 34].

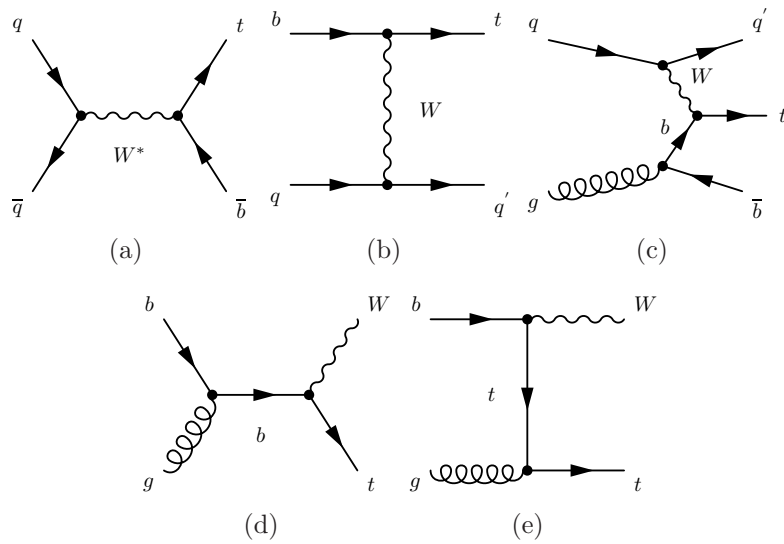


Figure 1.5: Leading order processes for single top production via the electroweak interaction: s-channel (a), t-channel (b), (c) and Wt associated production (d),(e).

Channel	σ at the LHC
$t\bar{t}$ pair production	830_{-40}^{+50} pb
single top s -channel	$7.2_{-0.5}^{+0.6}$ pb
single anti-top s -channel	$4.0_{-0.2}^{+0.1}$ pb
single top t -channel	146 ± 5 pb
single anti-top t -channel	89 ± 4 pb
single top and anti-top Wt -channel	82 ± 8 pb

Table 1.1: Predictions for top quark production cross sections at the LHC for $m_t = 175$ GeV and $\sqrt{s} = 14$ TeV [37, 38]. The calculations are performed at NLO, including NLL resummation of corrections from soft gluons near threshold. The uncertainties reported are relative to the variation of the renormalization scale value.

TEVATRON, the up quark and down quark distributions are larger than the gluon distribution. In addition, the TEVATRON is a $p\bar{p}$ collider and the anti-proton PDF distribution looks the same as the proton PDF, but for antiparticles. For this reason at the TEVATRON quark-antiquark annihilation processes dominate ($\sim 90\%$) with respect to gluon initiated processes ($\sim 10\%$). However, the total $t\bar{t}$ production cross section at the LHC increases by a factor 100 with respect to the TEVATRON cross section because of the steeply raising gluon PDF at low x . In this respect it is possible to consider the LHC a top quark factory.

Top quarks can also be produced via electroweak interaction through three different channels, the s -channel, the t -channel and the Wt associated production. The leading order Feynman diagrams for these processes are shown in Figure 1.5. The final state includes a single top quark and, because of the large background, single top events have only recently been observed [35, 36].

The calculation of the $t\bar{t}$ and single top production cross sections is performed at next-to-leading order (NLO) level of precision, including next-to-leading-log (NLL) resummations of higher order corrections. The cross section values for the LHC at $\sqrt{s} = 14$ TeV and for $m_t = 175$ GeV are reported in Table 1.1.

1.2.2 Top Quark Decay

One of the remarkable features of the top quark is its extremely short lifetime τ_t . The lifetime is obtained as the inverse of the width Γ_t that for the top quark can be calculated at NLO and is $\Gamma_t = 1.29 \text{ GeV}$ [5], corresponding to $\tau_t \approx 0.5 \times 10^{-24} \text{ s}$. Γ_t has to be compared to the typical scale $\Lambda_{QCD} \approx 200 \text{ MeV}$ at which quarks create hadrons together with quarks and anti-quarks from the vacuum. The top quark doesn't live long enough to hadronise, instead it is expected to decay before top-flavoured hadrons or $t\bar{t}$ quarkonium bound states can form.

The top quark decaying modes are determined by the square of the elements V_{tb} , V_{ts} , V_{td} of the CKM matrix. Imposing the unitarity of the three generations, the first two elements are estimated to be $V_{ts} < 0.043$ and $V_{td} < 0.014$, implying a value of $V_{tb} > 0.999$ [5]. With a mass above the Wb threshold the top quark is expected to decay almost exclusively in the two body channel $t \rightarrow Wb$. The W boson further decays either leptonically into $e\nu_e$, or $\mu\nu_\mu$ or $\tau\nu_\tau$ or hadronically into a $q\bar{q}'$ pair, where $q = u, d, s, c^1$. The $t\bar{t}$ pair decay topologies can be divided into three categories, depending on the W bosons decay.

Di-leptonic channel In this channel both W decay leptonically, leading to a branching ratio of 10.3%. Only events where the W decays involve e or μ are considered, reducing the branching ratio to 4.5%. These events are relatively easy to identify, thanks to the presence of two leptons and high missing transverse momentum in the final state. However none of the top quarks is fully reconstructed, so kinematical constrained fits have to be used in order to measure the top quark mass.

Semi-leptonic channel In this channel one W decays leptonically and the other W hadronically, leading to a branching ratio of 43.5%. Only events where the leptonic W decay involves e or μ are considered, reducing the branching ratio to 29%. These events are identified via the lepton and missing transverse momentum coming from the leptonic W . The top quark mass is measured from the hadronically decaying top quark. Because of the relative low background and of the full reconstruction of one of the top quarks, the mass measurements performed in this channel are the most precise.

¹The W decay channels $W \rightarrow ub$ and $W \rightarrow cb$ can be neglected because their decay rates are quadratic in $V_{ub} = 3.89 \cdot 10^{-3}$ and $V_{cb} = 40.6 \cdot 10^{-3}$, while the decay $W \rightarrow tb$ is kinematically forbidden.

All-hadronic channel In this channel both W decay hadronically, leading to a branching ratio of 46.2%. These events contain 6 jets, no leptons and no significant missing transverse energy in the final state. They are relatively hard to identify, because of the large background coming from multi-jet events. However the top mass measurement can profit from the full event reconstruction.

Performing the top mass measurement in all three decay channels is crucial, in order to cross check the results and to search for signs of effects beyond the Standard Model. The main topic of this thesis is the study of $t\bar{t}$ pairs in the all-hadronic decay channel, as discussed in Chapter 5. This analysis is extremely interesting, the event selection is orthogonal to the di-leptonic and semi-leptonic channels, leading to a complementary measurement of the top quark mass. At the same time the all-hadronic channel is a benchmark for the development of methods to control multi-jet events, which are a source of background for many of the searches for new physics, as in the case of Supersymmetric scenarios.

1.2.3 Top Quark Mass

The definition of the mass of a quark is not straightforward. Unlike leptons, quarks are confined inside hadrons and are not observed as free particles. For an observable particle, the position of the pole in the propagator is the definition of the particle mass. In QCD this definition is known as the pole mass m^{pole} and it is valid only in the perturbative regime. The pole mass cannot be used at arbitrary accuracy, because of non perturbative infrared effects in QCD (infrared renormalons). For this reason the accuracy of the pole mass is limited by the scale Λ_{QCD} . Nevertheless the pole mass can be related to any other renormalized Lagrangian mass $m(R, \mu)$ through a perturbative series $m^{pole} = m(R, \mu) + \delta m(R, \mu)$, where μ and R are scheme dependent scale parameters [39]. It is possible to chose schemes, known as short distance mass schemes, where the definition of the mass of a coloured particle is not limited by Λ_{QCD} . Such a choice allows, for example, to get to a precision of ~ 40 MeV on the measurement of the b -quark mass.

The top quark decays before forming hadrons. Therefore it is possible to measure directly the top quark mass instead of the hadron mass. For this purpose the invariant mass of the decay products of the top or anti-top quark can be reconstructed:

$$M_{i,\bar{i}}^2 = \left(\sum_{ica} p_i \right)^2, \quad (1.19)$$

where the set a depends on the specific reconstruction properties of the jets or of the leptons and missing transverse energy. The hadronic observable $M_{t,\bar{t}}^2$ corresponds to the pole mass m_t^{pole} , since it is designed to be sensitive to the on-shell region $p_t^2 \sim m_t^2$. This approach is applicable if the error on the measurement is larger than $O(\Lambda_{QCD}) \sim 1$ GeV.

In order to obtain a smaller error on the top quark mass measurement, it is possible to calibrate $M_{t,\bar{t}}^2$ back to the value of the top quark mass parameter of the Monte Carlo simulation that describes the data. This approach relies on a very good description of both physics effects and detector effects in the simulations. On the other hand, it is possible to show that the top quark mass parameter of the Monte Carlo is expressed in a short-mass renormalization scheme and thus allows for a precision smaller than Λ_{QCD} . It is difficult to identify the exact scheme in which the Monte Carlo top quark mass is quoted, for both the TEVATRON and the LHC. This is because the simulations used reach a leading order precision only. Nevertheless numerical results are already available and further studies are ongoing [39].

1.3 Monte Carlo Generators

In the real world accelerator machines produce collisions that are measured by detectors. All the information about a collision is recorded and form what is called an event. In particle physics, parallel to the real world, a virtual world exists. In the virtual world the hadron collision role is played by event generator programs and the detector role is played by detector simulation programs, like GEANT4 [40]. The real and virtual world can then share the same event reconstruction and subsequent physics analysis. The investigations performed in the real world have reached such a level of complexity that the full understanding of the results has to pass through the comparisons with the virtual world, on which full control is possible. For this reason, event generators are extremely important in particle physics and an increasing number of them, with higher level of precision and specifications, is appearing on the market. Event generators are generally called Monte Carlo event generators, because they use pseudo-random numbers to reproduce the quantum mechanical probabilities for the different outcomes of the process to be simulated.

The Monte Carlo generation of an event involves several stages [5, 41–43].

Hard scattering Configurations relative to the physics process of interest (e.g. $ug \rightarrow$

ug or $gg \rightarrow t\bar{t}$ or $gg \rightarrow h^0$) are generated, with probabilities proportional to the perturbative matrix element (ME). Depending on the process of interest, calculation of the matrix element at leading order (LO) or next-to-leading order (NLO) are taken into account.

Parton shower For the partons in the initial state as well as for the partons in the final state, bremsstrahlung emission can occur and is referred to as Initial State Radiation (ISR) or Final State Radiation (FSR), respectively. The radiation is described by higher order QCD terms that cannot be neglected. The enhancements occur when a soft gluon is emitted or when a gluon or a quark splits into two almost collinear partons. The leading contributions of the soft and collinear configurations can be identified and summed to all orders. In this way it is possible to calculate the probability for each parton, that it does not split into other partons between the scale Q_0 and some smaller scale Q_1 . The probability is represented by the Sudakov form factor and is used in Monte Carlo generators to determine the subsequent scales of the emissions, until $Q_0 \sim 1$ GeV. The result is a parton shower: from one parton at large Q many partons are produced whose Q lies in the non perturbative regime. ISR emissions can be modelled by space-like parton showers and FSR can be modelled by time-like parton showers. The existing parton shower programs reach a Leading Log (LL) precision, because they implement the higher order QCD corrections described by leading soft and collinear logarithms.

Hadronisation At the parton shower cut-off scale $Q \sim 1$ GeV confinement forces become important. The evolution of these forces cannot currently be described from first principles, so models have to be introduced. Two main approaches are used. The Lund string model involves the stretching of a colour string across quarks and gluons, and breaking it up into hadrons [44]. The cluster model breaks each gluon into a $q\bar{q}$ pair and then groups quark and anti-quark into colourless clusters, from which hadrons are created [45].

Underlying Event In the case of hadron colliders, it is important to take into account the interactions that can occur between the partons of the proton remnants, which don't contribute to the hard scattering. These interactions generate the so called underlying event and are described by $2 \rightarrow 2$ processes at a scale of few GeV (multiple parton interactions). The underlying event is not an independent

process, but it is interconnected to the parton shower and hadronisation processes in terms of their colour flow.

Different categories of event generators exist. In first instance, general purpose event generators cover all the aspects mentioned above and include LO matrix element calculations of the hard scattering for a wide range of processes. Examples are the PYTHIA [44] and HERWIG [45] programs. When the process of interest is not included into the general purpose generators or when a higher matrix element accuracy is desired, more specialised programs have to be considered. In the case of processes like multi-jet or W plus jet production, the LO matrix element calculation is provided by programs like ALPGEN [46]. Then the outcome of this simulation has to be interfaced to a general purpose event generator that provides the parton shower and hadronisation and underlying event description. In order to avoid double counting in the interface step, dedicated matching algorithms have been developed, like the CKKW [47] or MLM [48] algorithm. In cases like $t\bar{t}$ production, NLO matrix element calculations are available. These calculations have to be interfaced to general purpose event generators as well, in order to get the complete event simulation. This matching has become recently possible, with the use of algorithms like MC@NLO [49].

This list of possible examples of event generators doesn't pretend to be complete, but focuses on the Monte Carlo programs used for the studies presented in Chapters 4 and 5. A more detailed discussion of the topic can be found in [41] and [42].

Chapter 2

The ATLAS Experiment

At the European Organisation for Nuclear Research (CERN) fundamental physics has been investigated since 1954. In the 1980s the concept of a proton-proton collider at an extraordinary high luminosity and centre of mass energy, called the Large Hadron Collider (LHC), was conceived. The LHC project was approved for construction in 1994 by the CERN Council and already in 1998 the excavation works for the construction of the experiment caverns had begun. Then, at the end of the year 2000, the Large Electron-Positron Collider (LEP) was shut down to start the installation of the LHC machine. In September 2008, after eight years of construction and commissioning, the first proton beams were successfully circulated in the two directions, but on the 19th of September a faulty interconnect between two of the LHC magnets caused an incident. As a consequence several magnets were damaged and the collider operation had to stop for the necessary repair to take place. Finally, in November 2009, the LHC operations restarted and on the 23rd of November first collisions at 900 GeV centre of mass energy were recorded. Already on the 30th of November the world record centre of mass energy of 2.36 TeV was reached. After the winter shut down, on the 19th of March 2010, the new record of 7 TeV centre of mass energy was established. Since then the LHC has run at constantly increasing instantaneous luminosities until the 4th of November, when proton-proton collisions have been stopped. The LHC has taken only 4 days to successfully switch from proton-proton to ion-ion collisions: the beams have been accelerated to an energy of 287 TeV and ion-ion collisions have taken place at an centre of mass energy of 2.76 TeV per nucleon pair, which is the highest centre of mass energy ever achieved for nuclear collisions. The LHC has run with ions until the winter shutdown 2010.

In this Chapter the main features of the LHC collider and of the ATLAS experiment are outlined ¹. In particular, Section 2.1 focuses on the LHC accelerator machine, while Section 2.2 on the ATLAS detector. Finally Section 2.3 describes the worldwide distributed LHC computing system, known as Grid, that allows the storage and analysis of the LHC experimental data.

2.1 The Large Hadron Collider

The Large Hadron Collider is the largest particle accelerator in the world [53–55]. The LHC is built in a circular tunnel of 27 km in circumference, that was previously used by the LEP collider. The tunnel is buried around 50 to 175 m underground. The tunnel straddles the Swiss and French border, on the outskirts of Geneva.

The LHC is designed to collide two counter rotating beams of protons or heavy ions. Proton-proton collisions are foreseen at an energy of 14 TeV in the centre of mass and at a luminosity of $10^{34}\text{cm}^{-2}\text{s}^{-1}$. The ions are completely ionised lead atoms. The ion-ion collision are foreseen at a centre of mass energy of 5.52 TeV per nucleon pair (which corresponds to accelerating the beams to an energy of 574 TeV) and at a luminosity of $10^{27}\text{cm}^{-2}\text{s}^{-1}$. The particle beams circulate into two separate tubes, in ultrahigh vacuum (10^{-13} atm), in order to avoid collisions with gas molecules.

In particular, each proton beam consists of 3564 bunches, of which 2808 are filled: a bunch contains $1.15 \cdot 10^{11}$ protons, at the start of the nominal fill. Every bunch is 7.55 cm long and has transverse dimensions of the order a mm, that is reduced to $16 \mu\text{m}$ at the interaction point. The total proton-proton cross section at 14 TeV centre of mass energy is approximately 110 mb, and the inelastic cross section is 60 mb. So, at a full luminosity of $10^{34}\text{cm}^{-2}\text{s}^{-1}$, 20 collisions per bunch crossing are expected. In this way, the protons keep circulating for hours in the ring, before a new filling is needed. The protons are accelerated by the Linac, PS booster, PS and SPS accelerators, before being injected into the LHC ring with 450 GeV energy. A schematic view of the accelerator chain is shown in Figure 2.1. In the LHC ring the protons are further accelerated using 8 radio-frequency cavities, with maximum electric field of 5.5 MV/m. The protons are bent into a circular trajectory using dedicated magnets. The momentum of the proton p (GeV/c), the magnetic field B (Tesla) and the radius of the proton trajectory R (m)

¹The description of the ATLAS detector is taken from [50–52]

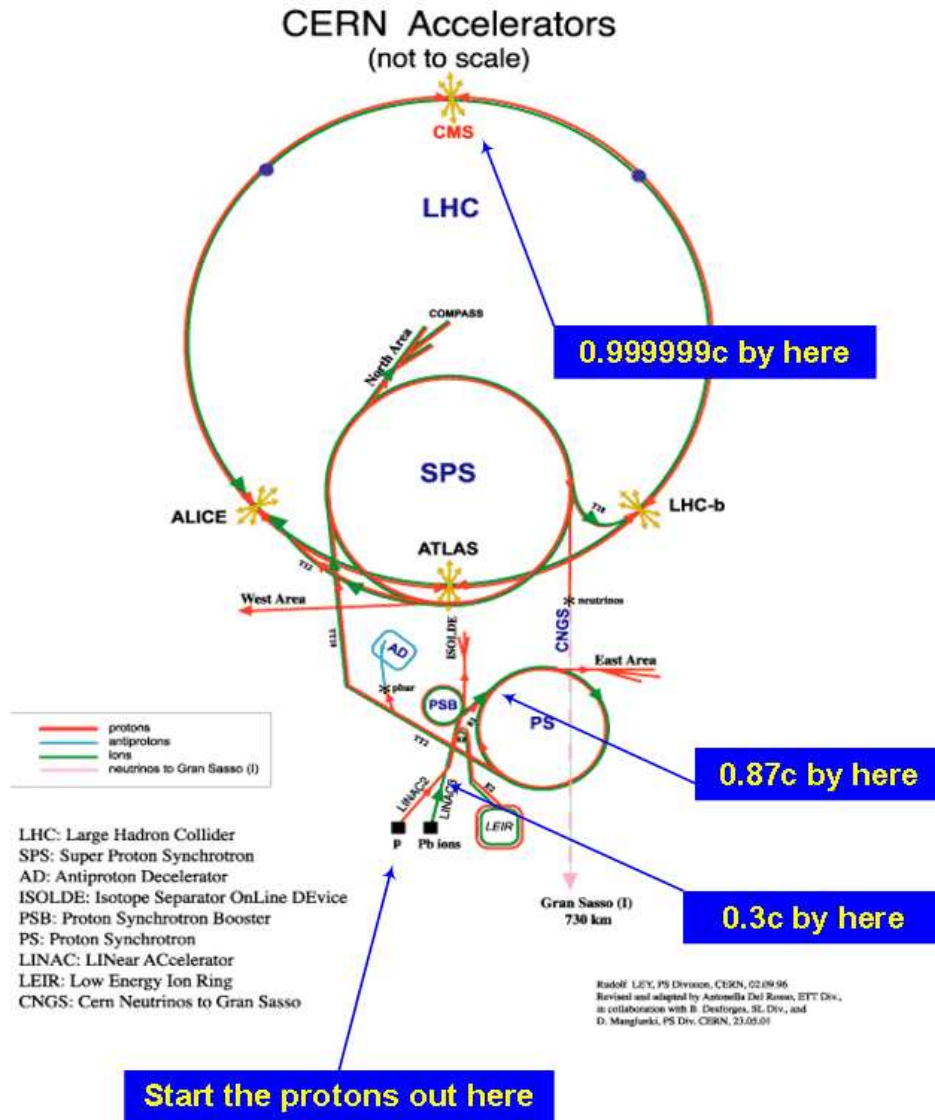


Figure 2.1: Diagram of the LHC accelerators and experiments. The proton speed is reported for the various acceleration steps.

are connected by the Lorentz formula:

$$p = 0.3 \cdot B \cdot R . \tag{2.1}$$

In order to achieve the 7 TeV energy per beam, keeping the radius $R = 4.3$ km constant, an average magnetic field of 5.5 T is needed. This strong magnetic field is realised using 1232 dipole magnets. Every magnet generates a magnetic field of 8.4 T at a current of around 11700 A. The magnets are superconducting and are kept cold (1.9 K), using a

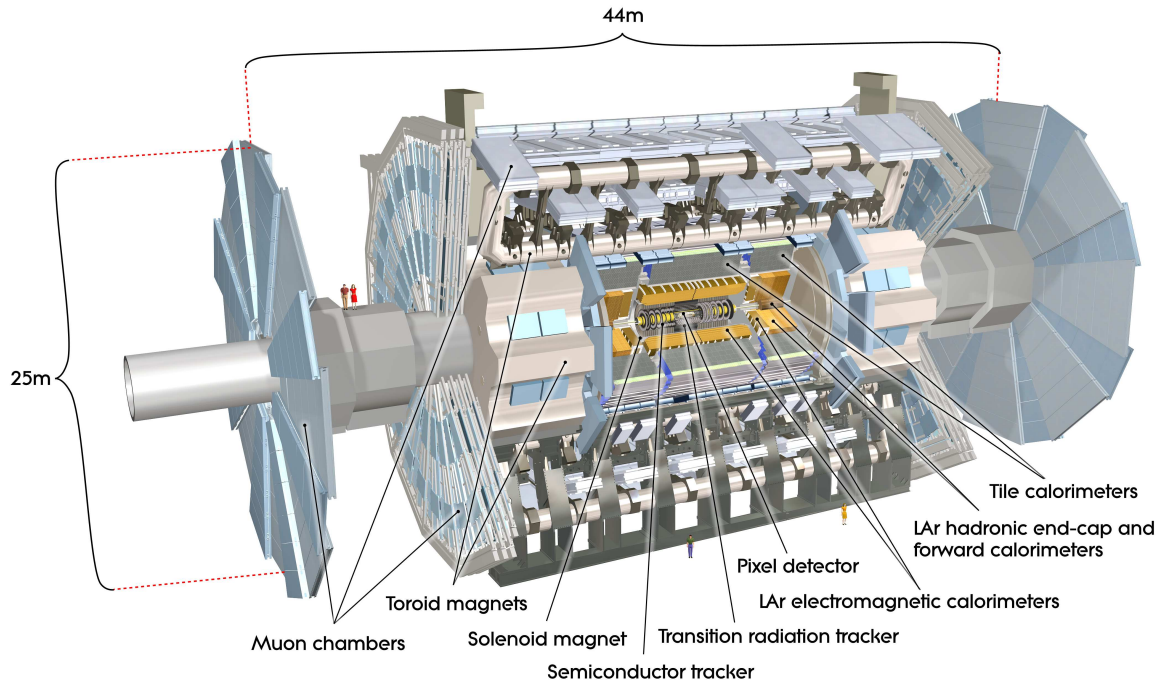


Figure 2.2: Computer generated image of the ATLAS detector.

superfluid helium technology.

The protons, guided by magnets, collide in 8 interaction points named IP1-IP8. Four experiments have been designed for the LHC: ATLAS (A Toroidal LHC Apparatus) [52] located in IP1, ALICE (A Large Ion Collider Experiment) [56] located in IP2, CMS (Compact Muon Solenoid) [57] located in IP5 and LHCb (LHC beauty) [58] located in IP8. The ATLAS and CMS detectors are multi-purpose, their principal aim is to investigate physics beyond the Standard Model. The ALICE detector is designed to reveal and study the quark-gluon plasma and LHCb is mainly focused on CP violation measurements in the b -quark sector.

2.2 The ATLAS Detector

The ATLAS collaboration has proposed to build a multi-purpose detector, able to fully exploit the physics opportunities given by the high energy and high luminosity of the LHC. The detector requirements have been defined with respect to the observation of a set of possible TeV scale phenomena. In first instance, the discovery of the Standard Model Higgs boson, over the allowed mass range, has been used as benchmark. This

implies very good photon reconstruction for the double photon decay or high b -tagging performance for the $H \rightarrow b\bar{b}$ decay in associated production to $t\bar{t}$ pairs or electroweak bosons. For higher Higgs boson masses, decays into a pair of W or Z bosons are possible and high precision lepton reconstruction is required. Searches for the Higgs boson in scenarios beyond the Standard Model have been considered, which add the requirement of good τ lepton reconstruction. Scenarios that predict the existence of heavy W' and Z' imply good performance in reconstructing high p_T leptons and their charge. Precise measurement of the jet cross-section is needed to address the issue of quark compositeness and implies accurate jet reconstruction and calibration. Supersymmetric theories that conserve R-parity predict decay cascades of particles as squarks and gluinos to the lightest stable supersymmetric particle (LSP). The LSP is predicted to be weakly interacting with the detector, creating a large missing transverse energy (MET) signal. Thus, for Supersymmetry discoveries, high resolution MET measurement is a key point. Models that propose the existence of extra dimensions could as well lead to large MET signatures related to gravitons escaping the detector or to the appearance of TeV scale Kaluza-Klein resonances. These are only few examples of the various experimental signatures that have driven the design of ATLAS. In addition to the physics potential, the experimental challenges due to the LHC environment had to be addressed. These include high interaction rates, high radiation doses as well as large pile up (20 events per bunch crossing) and large QCD cross-section. The combination of the various requirements can be turned into a set of general criteria:

- fast and radiation hard detector electronics, to handle radiation and high interaction rate;
- high detector granularity, to reduce the influence of overlapping events;
- large detector acceptance, for measurements like MET;
- high momentum resolution for charged particle reconstruction in the tracker, for efficient τ and b tagging;
- very good electromagnetic calorimetry for e and γ reconstruction together with full coverage hadronic calorimetry for jets and MET reconstruction;
- good muon identification over a large momentum spectrum together with charge identification;

- highly efficient trigger.

The overall detector layout is shown in Figure 2.2. The ATLAS detector is designed with cylindrical symmetry, around the beam direction, and it is centred at the interaction point. The nominal interaction point is the origin of the ATLAS coordinate system. The beam direction defines the z -axis and the $x - y$ plane is transverse to it. The positive x -axis is defined as pointing to the centre of the LHC ring and the positive y -axis as pointing upwards. The side A of the detector is the one with positive z and the side C the one with negative z . The azimuthal angle ϕ is measured around the beam axis and the polar angle θ is the angle from the beam axis. The pseudorapidity η is defined as $\eta = -\ln \tan \theta/2$ and distances in the $\eta - \phi$ space are usually given in terms of $\Delta R = \sqrt{\Delta\eta^2 + \Delta\phi^2}$. Transverse momentum p_T , transverse energy E_T and missing transverse energy MET are defined in the $x - y$ plane.

The ATLAS detector can be divided into four main parts: the inner detector, the calorimeters, the muon spectrometer and the magnetic system. The inner detector tracks the particle trajectories, then the particle energy is measured by the calorimeters, and finally the muon spectrometer detects the very penetrating muons. The magnetic system is designed to bend the charged particle trajectory in the inner detector and in the muon spectrometer, in order to measure the particle momentum. The performance goals for tracking, calorimetric energy measurement and muon momentum measurement are listed in Table 2.1. In the followings some details are given on the specifications of the ATLAS detector components.

2.2.1 Magnetic System

The ATLAS magnetic system is composed of three parts, the Central Solenoid, the Barrel Toroids and the End-Cap Toroids, as shown in Figure 2.2. The Central Solenoid provides the inner detector with a central magnetic field of 2 T. The Barrel Toroids and the End-Cap Toroids generate the magnetic field for the muon spectrometer. Their performance, in terms of bending power, is characterised by the integral of the magnetic azimuthal field component over a straight line trajectory, between the inner and outer radius of the toroids. In these terms the Barrel Toroids provides 2 to 6 Tm in the range $1.3 < |\eta|$ and the End-Cap Toroids provide 4 to 8 Tm in the range $1.6 < |\eta| < 2.7$. The bending power is lower in the range $1.3 < |\eta| < 1.6$, where the two magnets overlap. All the magnets are superconducting and are indirectly cooled by forced flow of helium at 4.5 K through tubes, which are welded on the casing of the windings. The overall

Detector component	Required resolution	η coverage measurement	η coverage trigger
Inner detector	$\sigma_{p_T}/p_T = 0.05\% p_T \oplus 1\%$	± 2.5	
EM calorimeter	$\sigma_E/E = 10\%/\sqrt{E} \oplus 0.7\%$	± 3.2	± 2.5
Hadronic calorimeter barrel and end-cap	$\sigma_E/E = 50\%/\sqrt{E} \oplus 3\%$	± 3.2	± 3.2
forward	$\sigma_E/E = 100\%/\sqrt{E} \oplus 10\%$	$3.1 < \eta < 4.9$	$3.1 < \eta < 4.9$
Muon system	$\sigma_{p_T}/p_T = 10\%$ at $p_T = 1$ TeV	± 2.7	± 2.4

Table 2.1: General performance goals for the ATLAS detector. Performance in the case of the inner detector is quoted for tracks, in the case of the electromagnetic calorimeter for e and γ , in the case of the hadronic calorimeter for jets and in the case of the muon system for muons. For high p_T muons the muon spectrometer performance are independent of the inner detector system. The units for energy E and transverse momentum p_T are GeV.

dimensions of the magnet system are 26 m in length and 20 m in diameter, this large size demands careful engineering.

2.2.2 Inner Detector

The inner detector consists of three parts, all contained in the Central Solenoid. The Pixel Detector is the closest to the interaction point and has a very high spatial resolution. The Silicon Microstrip Trackers (SCT) and a Transition Radiation Tracker (TRT) are at the outer radii and provide continuous tracking measurements. The inner detector structure is shown in Figure 2.3.

The Pixel Detector is designed to precisely measure the particle impact parameters and the decay vertices of short living particles, as b -hadrons and τ leptons. It reaches a spatial resolution of $\Delta R\phi = 10 \mu\text{m}$, $\Delta z = 115 \mu\text{m}$ both in the barrel and in the end-caps.

The Silicon Microstrip Trackers system is designed to provide eight precision measurements per track in the intermediate radial range, contributing to the measurement of the momentum, impact parameter and vertex position. For the barrel and end-caps SCT the spatial resolution is $\Delta R\phi = 17 \mu\text{m}$, $\Delta z = 580 \mu\text{m}$. Tracks can be distinguished if separated by more than $\sim 200 \mu\text{m}$.

The Transition Radiation Tracker design is based on the use of straw tubes. The straws can operate at the very high event rates expected at the LHC, thanks to their small diameter and to the isolation of the sense wires within individual gas volumes.

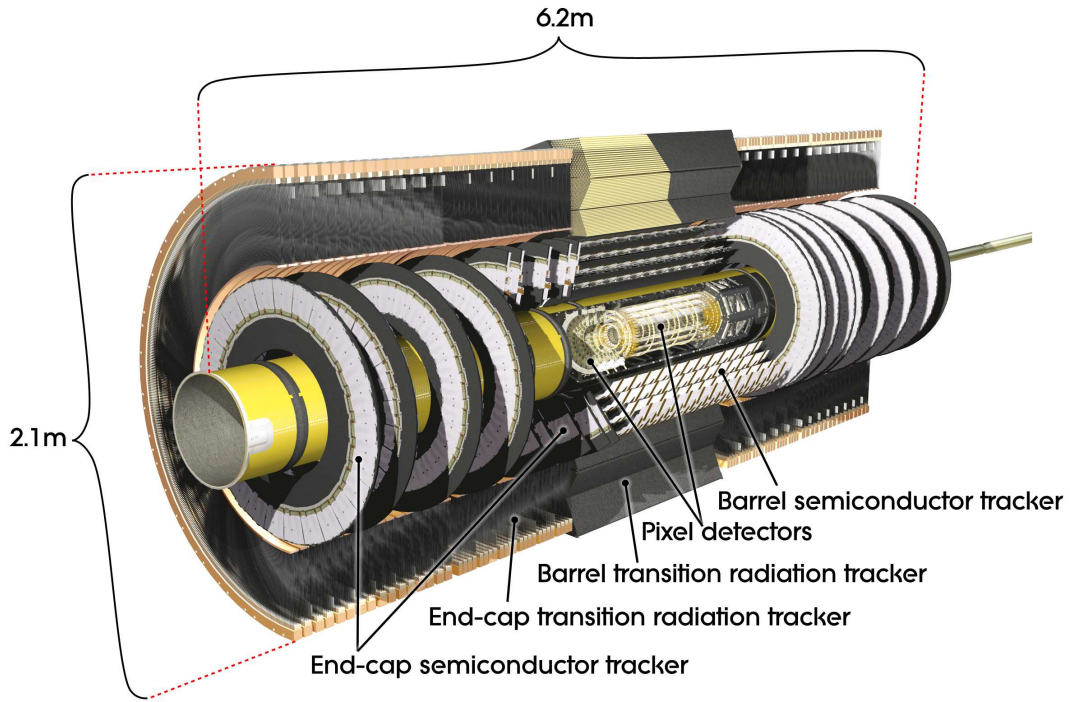


Figure 2.3: Cut-away view of the ATLAS inner detector.

The employed mixture of gases is 70% Xe, 20% CO₂ and 10% CF₄. The use of xenon gas allows for the identification of electrons detecting the transition radiation photons, created in a radiator positioned between the straws. The TRT detects on average 36 measurements on every track. It provides information only in $R-\phi$ with a spatial resolution in of 130 μm per straw.

2.2.3 Calorimeters

The ATLAS calorimeter system offers an hermetic coverage in ϕ and in pseudorapidity up to $|\eta| < 4.9$. It provides excellent performance in terms of energy and position resolution and ensures good containment of the electromagnetic and hadronic showers over the whole acceptance region. The electromagnetic calorimeter contains 22 radiation length X_0 in the barrel and 24 X_0 in the end-caps. The hadronic calorimeter and the electromagnetic calorimeter together have a thickness of 11 interaction lengths (λ) at $\eta = 0$, including about 1.5 λ from the outer support. This thickness has been measured to be sufficient to reduce punch-through into the muon system. At the same time 10 λ of active calorimeter are adequate to provide good resolution for high energetic jets.

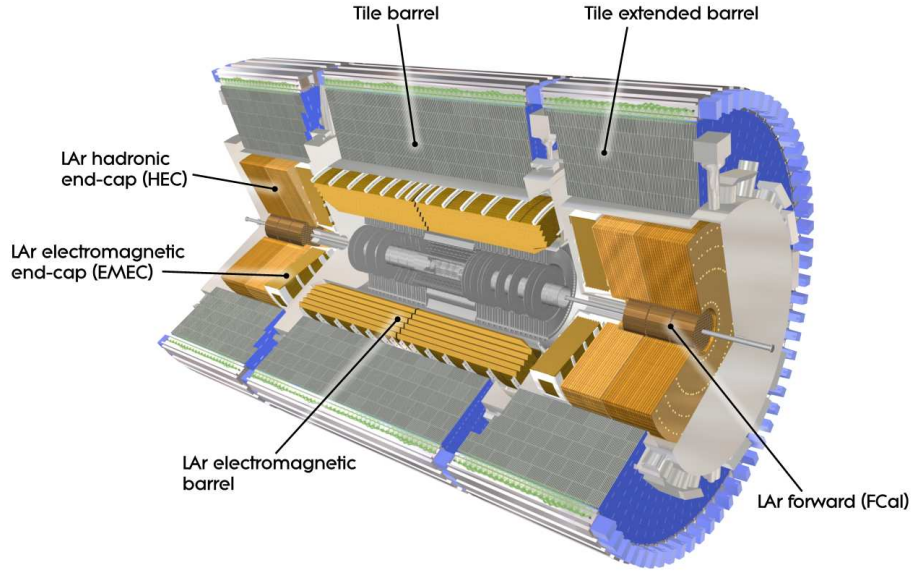


Figure 2.4: Cut-away view of the ATLAS calorimeter system.

The ATLAS calorimeter system consists of an electromagnetic (EM) calorimeter covering the pseudorapidity region $|\eta| < 3.2$, an hadronic barrel calorimeter HCAL covering the region $|\eta| < 1.7$, an hadronic end-cap calorimeter HEC covering the region $1.5 < |\eta| < 3.2$ and a forward calorimeter FCAL covering the region $3.1 < |\eta| < 4.9$. Over the pseudorapidity range $|\eta| < 1.8$ the EM calorimeter is preceded by a presampler detector, used to correct for the energy lost in the material upstream the calorimeter. A schematic view of the different calorimeters is shown in Figure 2.4. All calorimeters in ATLAS are sampling calorimeters and are based on two different technologies. The hadronic calorimeter in the barrel and extended barrel region, called Tile calorimeter, is built using iron as absorber and plastic scintillating tiles as active material. All the other calorimeters in ATLAS use liquid argon (LAr) as active material, but different absorbers and geometry configurations. The LAr technology offers good linearity over a wide energy range, longterm stability and radiation hardness. The LAr calorimeters are housed in two different cryostats, one in the barrel and the other in the end-cap region.

In order to achieve good performance for the energy measurement, the calorimeter signal has to be calibrated to recover for its non-compensating nature. In fact, processes that don't create an ionisation signal, like nuclear interactions, are not detected by the ATLAS calorimeter. Energy deposits in terms of these processes are possible for

hadrons but not for electrons and photons, leading to an average higher response of the calorimeter for electromagnetic particles than for hadronic ones. Various effects on top of non-compensation have to be taken care of in order to access the energy of the hadrons produced in the hard interaction. A description of the calorimeter signal reconstruction and calibration is given in Chapter 3, while the performance and validation studies on one of the ATLAS calibration approaches, the Local Hadron Calibration, are discussed in Chapter 4.

Some details about the design of the various ATLAS calorimeters are given in the following.

Electromagnetic calorimeter The electromagnetic calorimeter is divided into a barrel part for $|\eta| < 1.475$ and two end-cap parts for $1.375 < |\eta| < 3.2$. A forward component is included into the forward calorimeter as discussed below. The barrel calorimeter consists of two identical half-barrels separated by a 6 mm gap at $z = 0$. Each end-cap calorimeter is divided into two coaxial wheels, an inner wheel in the region $1.375 < |\eta| < 2.5$ and an outer wheel in the region $2.5 < |\eta| < 3.2$. In the electromagnetic calorimeter lead is used as absorber and LAr as active material. The two materials are arranged in an accordion geometry structure that provides complete ϕ symmetry without azimuthal cracks. In this way the signals in the different samplings are collected on one electrode and no additional integration is needed.

Tile calorimeter The Tile Calorimeter is composed of one barrel part in the region $|\eta| < 1.0$ and two extended barrel parts in the region $0.8 < |\eta| < 1.7$. The tiles are placed radially and staggered in depth. The structure is periodic along z . Two sides of the scintillating tile are read out by wavelength shifting fibres into two separate photomultipliers, providing a quick signal response. The iron used as a passive material serves as well as a flux return joke for the central solenoid magnetic field.

The hadronic end-cap calorimeter The hadronic end-cap (HEC) calorimeter consists of two independent wheels per end-cap, located directly behind the electromagnetic end-cap calorimeter. In the HEC calorimeter copper is used as absorber and LAr as active material. Each of the HEC wheels is built from 32 identical wedge-shaped modules. The front wheels, closer to the interaction point, are built out of 25 mm copper plate, while the back wheels use 50 mm copper plates. In order to reduce the drop in material density at the interface to the Tile calorimeter (at $|\eta| \sim 1.7$) and at

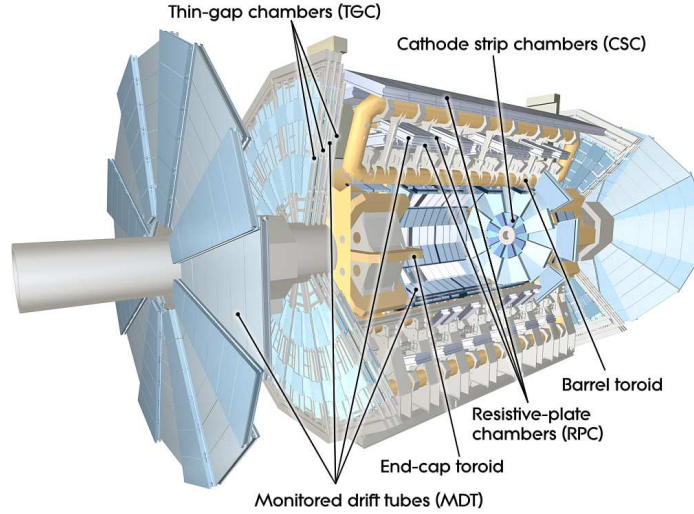


Figure 2.5: Cut-away view of the ATLAS muon system.

the interface to the forward calorimeter (at $|\eta| \sim 3.1$), the HEC calorimeter slightly overlaps with both, extending over the region $1.5 < |\eta| < 3.2$.

The forward calorimeter The forward calorimeter (FCAL) covers the region $3.1 < |\eta| < 4.9$. The FCAL calorimeter is integrated into the end-cap cryostat. This choice provides benefits in terms of uniformity of the calorimetric coverage, but exposes the FCAL to high radiation doses. In order to cope with radiation, the front face of the FCAL calorimeter is recessed of about 1.2 m with respect to the front face of the EM calorimeter and in order to still guarantee 10λ of depth a very high density design has been chosen. The FCAL is composed of three modules in each end-cap, for the first module, nearer to the interaction point, copper is used as absorber, while for the other two modules tungsten is used. The first module is optimised for electromagnetic shower measurements, while the other two modules are designed for hadronic shower measurements. Each module consists of an absorber metal matrix, with longitudinal channels filled with concentric rods and tubes. The rods are at positive voltage, the tubes and the matrix are grounded and the space in between is filled up with LAr sensitive medium. This geometry allows for an excellent control on the ion buildup in the gaps, which are as small as 0.25 mm in the first module.

2.2.4 Muon Spectrometer

The design of the muon spectrometer is based on the magnetic deflection of muon tracks in the large super conducting toroid magnets:

- over the region $|\eta| < 1.0$ magnetic bending is provided by the large barrel toroid;
- over the region $1.4 < |\eta| < 2.7$ muon tracks are bent by two small end-cap magnets, inserted into both ends of the barrel toroid;
- over the region $1.0 < |\eta| < 1.4$ magnetic deflection is provided by a combination of barrel and end-cap fields (transition region).

This magnet configuration provides a field that is mostly orthogonal to the muon trajectories, while minimising the degradation of resolution due to multiple scattering. The muon system is composed of two types of precision tracking chambers covering the region up to $|\eta| < 2.7$ and two types of trigger chambers covering the region up to $|\eta| < 2.4$. A cut-away view of the ATLAS muon system is shown in Figure 2.5.

In the barrel region the tracking chambers are arranged in three cylindrical layers around the beam axis, while in the end-cap region they are installed in three layers perpendicular to the beam axis. Over most of the η range, a precision measurement of the track coordinates is provided by Monitored Drift Tube (MDT) chambers. At large pseudorapidity range ($2 < |\eta| < 2.7$) Cathode Strip Chambers (CSCs) with higher granularity are used to withstand the demanding rate and background conditions. The measurement of the muon tracks is made in the $R-z$ projection, in the direction parallel to the bending direction of the magnetic field. The axial coordinate z is measured in the barrel, and the radial coordinate R in the transition and end-cap regions. In order to reach the desired momentum resolution of 10 % for $p_T = 1$ TeV, a relative alignment precision of $30 \mu\text{m}$ is needed. Over the large global dimensions of the spectrometer, it is not possible to stabilise the position of the chambers at the $30 \mu\text{m}$ level. Therefore an optical alignment system composed of 12000 sensors has been installed to monitor chamber deformations and positions. In this way, displacements up to ~ 1 cm can readily be corrected for the offline analysis.

The muon trigger system covers the pseudorapidity range $|\eta| < 2.4$. Resistive Plate Chambers (RPCs) are used in the barrel region and Thin Gap Chambers (TGCs) in the end-cap regions. The trigger chambers have to identify bunch crossing, with a time resolution better than the LHC bunch spacing of 25 ns. Moreover the trigger chambers

measure the second coordinate, in the direction orthogonal to the one measured by the precision chambers, with a typical resolution of 5–10 mm.

2.2.5 Forward Detectors

ATLAS is equipped with a variety of forward detectors.

The Beam Controlling Monitor (BCM) comprises two stations, with four diamond sensors of $1 \times 1 \text{ cm}^2$, at $\pm 1.8 \text{ m}$ from the interaction region. It covers a pseudorapidity range of $3.9 < |\eta| < 4.1$. The BCM detector is expected to provide monitoring information about anomalous beam conditions, as beam-gas and beam-collimator interactions. It is designed to work for the full luminosity range of the LHC, with a sufficient time resolution, to identify individual bunch crossings. Its capability to distinguish proton-proton interactions from backgrounds relies on time-of-flight information: only collision events give synchronous signals on the two sides.

The Minimum Bias Trigger Scintillator (MBTS) system has eight wedge-shape plastic scintillators installed on the front of the LAr end-cap cryostat, at $\pm 3.6 \text{ m}$ from the interaction region. The MBTS goal is to trigger minimum bias events, vetoing halo events for a luminosity $L < 5 \times 10^{32} \text{ cm}^{-2}\text{s}^{-1}$, and to contribute to the level 1 trigger. It will be used mostly during the commissioning phase. Although the lifetime of the detector will be limited by radiation damage, in the initial stage the MBTS measurement of the minimum bias trigger rate will provide luminosity monitoring information.

The Zero Degree Calorimeter (ZDC) is located at $\pm 140 \text{ m}$ from the interaction point and it consists of layers of alternating quartz rods and tungsten plates. The ZDC measures neutral particles in the pseudorapidity region $|\eta| < 8.2$ and plays a key role in determining the centrality of heavy ion collisions.

ALFA (Absolute Luminosity for ATLAS) is a system of ultra-small-angle detectors, located at $\pm 240 \text{ m}$ from the interaction region. The ALFA detector is designed to measure elastically scattered protons in the vicinity of the LHC beam, with angles in the μrad range. It consists of 4 stations of Roman Pots inserted in the beam pipe, equipped with position sensitive detectors.

LUCID (LUminosity measurement using Cherenkov Integrating Detector) is a relative luminosity monitor located at $\pm 17 \text{ m}$ from the interaction point. It is composed of Cherenkov tubes surrounding the beam pipe. It monitors the luminosity by counting the number of particles coming from the interaction point, for every bunch crossing.

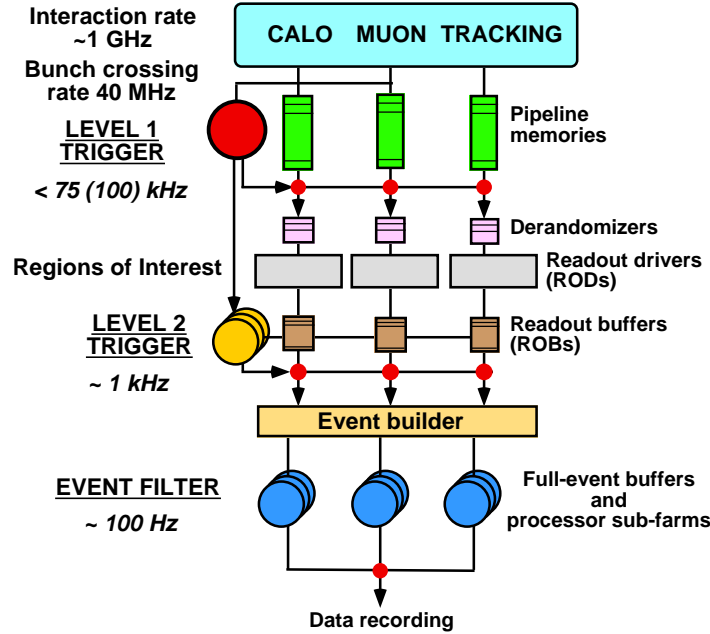


Figure 2.6: ATLAS trigger and data acquisition system.

2.2.6 Trigger System

The ATLAS trigger and data-acquisition (DAQ) system is based on three levels of online event selection. The initial bunch crossing rate of acquired events is 40 MHz at full luminosity and has to be reduced to 100 Hz, for permanent storage. This requirement implies a rejection factor of 10^7 for minimum bias events, but at the same time excellent efficiency must be retained for the rare physics processes of interest. A simplified diagram of the trigger/DAQ system is shown in Figure 2.6.

The level 1 (LVL1) trigger makes an initial selection, based on object information provided by a subset of detectors. High transverse momentum (p_T) muons are identified using only the trigger chambers (RPCs and TGCs). High p_T electrons and photons, jets, τ leptons decaying into hadrons, large missing energy and total transverse energy information are collected from all the calorimeters. The LVL1 trigger decision is based on combinations of objects required in coincidence or veto. Most of the physics requirements of ATLAS can be met, at the LVL1 level, using relatively simple selection criteria. The LVL1 trigger is as well in charge of identify the bunch crossing of interest. This is a challenging task, because, for example, the physical size of the muon spectrometer implies time-of-flight comparable to the bunch-crossing period. The LVL1 trigger reduces the event rate to 75 kHz using purpose built hardware

processors. During a time of latency, the information from all detector channels has to be conserved into pipeline memories. The latency time is required to be less than 2.5 μs for reasons of cost and reliability. The design latency for the LVL1 is thus 2.0 μs .

The level 2 (LVL2) trigger uses region of interest (RoI) information, provided by the LVL1 trigger. This information concerns position, p_T , and energy sums of the candidate objects. The RoI data are sent from the LVL1 to the LVL2 using a dedicated data path. From the RoI data, the LVL2 trigger decides which additional information have to be required and moved from the readout buffers (ROBs) to the LVL2 trigger. In general, only a few per cent of the full event data are required, thanks to the RoI mechanism. The LVL2 is expected to reduce the rate to ~ 1 kHz.

After the LVL2, the last stage of the online selection is performed by the Event Filter (EF). It employs offline algorithms, adapted to the online selection, and makes use of the calibration data, alignment information and magnetic field map. The EF reduces the event rate of an order of magnitude, to ~ 100 Hz, corresponding to an output rate of ~ 100 MB/s, that is the full event data to be recorded.

2.3 Worldwide LHC Computing Grid

The Worldwide LHC Computing Grid (WLCG) is a distributed computing infrastructure for the storage and the analysis of data from the four LHC experiments [59,60]. The LHC, running at design centre of mass energy and luminosity, produces roughly 15 Petabytes (15 million Gigabytes) of data per year. This impressive amount of data has to be accessed by more than 5000 scientists from the 500 worldwide research institutes and universities participating in the LHC. The analysis of the data is estimated to require of the order of 100000 CPUs at 2004 measures of processing power. Moreover the data collected have to be stored and kept available for at least the 15 years estimated lifetime of the LHC. The mission of WLCG project is to provide the appropriate data storage and analysis infrastructure for the entire LHC community. A traditional approach would have been to centralise all the computing resources at one location near to the experiments. Instead, in the case of the LHC, a novel approach - a computing Grid - was chosen. The Grid model is based on distributed data storage and analysis. The Grid approach presents several benefits. In first instance, concerning security, in a distributed system there are no single points of failure and the presence of multiple copies of the data in different locations ensures load balancing of the resources. On a world time scale, the availability of computing resources in all time zones facilitates

their monitoring and support. In addition, the costs for maintaining and upgrading the necessary resources can be handled locally by the participating organisations. A distributed system also presents significant challenges. An adequate level of network bandwidth between the contributing resources has to be ensured and the coherence of software versions installed in various locations has to be guaranteed despite of the heterogeneous hardware. Finally, a safe and fair accounting mechanism has to provide access to the different groups of scientists, depending on their needs.

The WLCG has addressed these several requirements with a four-tiered model.

- The raw data emerging from the data acquisition systems are recorded at the Tier-0 centre at CERN. The first event reconstruction takes place at the Tier-0, where a copy of the reconstructed data is stored. A second copy is distributed to one or more Tier-1 centres associated with the experiment.
- The role of the Tier-1 centres varies according to the experiment. In general they have the prime responsibility for managing permanent storage of raw, simulated and processed data. They provide as well computational capacity for reprocessing and for analysis of large amounts of data. At present 11 Tier-1 centres have been defined.
- The role of the Tier-2 centres is to provide computational capacity and appropriate storage for Monte Carlo simulation and for end-user analysis. The Tier-2 obtain data from the Tier-1, and the data generated at Tier-2 is sent to Tier-1 for permanent storage. More than 100 Tier-2 centres have been identified.
- Tier-3 centres are computing facilities in universities and laboratories. Tier-3 take part in the processing and analysis of LHC data and are provided with access rights as decided by the different experiments. However, the direct management of the Tier-3 lie outside the scope of the WLCG.

A huge work of coordination and interface is needed to enable the user to access the distributed resources. This key role is played by the middleware software, which interfaces the operating system software of the computers with the physics application software required by the user.

Despite of the challenges and of the absolute novelty of the project, the WLCG is a great success. ATLAS users can access the Grid resources through the dedicated GANGA (A User Grid interface for Atlas and LHCb) interface [61]. In fact, all the

results presented in Chapters 4 and 5 have been obtained with the use of the WLCG via GANGA.

Chapter 3

Jets and Calibration

It is common to think of QCD phenomena in terms of quarks and gluons. But they are never visible. Right after being produced, a quark or a gluon fragments and hadronises, leading to a collimated spray of energetic hadrons, a jet. Jets set a correspondence between the partonic and the hadronic level and thus need to be defined as infrared and collinear safe quantities.

The high energetic hadrons enter the detector and interact with it, depositing most of their energy in the form of particle showers in the calorimeters. Therefore, beside the correspondence between the parton and the hadron level, a correspondence between the hadron level and the energy measured in the experimental detector has to be established. This is set by jet calibration, which is a technique aimed at reconstructing the initial energy of the jet from the calorimeter deposits.

In this Chapter a description of the jet algorithms and the jet calibration methods adopted by the ATLAS collaboration is given, with special focus on the approaches used in Chapters 4 and 5. In particular, in Section 3.1 various jet algorithm definitions are discussed, in Section 3.2 the formation of hadronic and electromagnetic showers is described, in Section 3.3 the calorimeter signal reconstruction in terms of topological clusters is presented and in Section 3.4 various methods for calibrating the calorimeter signal back to the jet level are described.

3.1 Jet Algorithm

Jets do not exist a priori, they are defined through the use of jet algorithms. A jet algorithm should be applicable to experimental measurements, to the output of

parton shower Monte Carlos and to partonic calculations, in order to allow comparisons between predictions and measurements in terms of the same observable. A jet algorithm should be collinear and infrared safe: if an event is modified by collinear splitting or soft emission, the set of hard jets that are found should remain unchanged. In this way, the jet definition allows for finite predictions at any order of perturbative QCD. A jet algorithm should be as much as possible independent of non-perturbative effects like hadronisation models and underlying event, in order to be sensitive to the hard process of interest. From the experimental point of view only, a jet algorithm should perform fast in order to contribute to the online event selection and it should be stable against detector noise and pile-up noise (coming from events occurring in the same bunch crossing or from previous events).

Two classes of jet algorithms exist. The cone type algorithms are based on the idea that fragmentation and hadronisation leave unchanged the energy flow inside a cone. This can be seen as a top-down approach to the problem and it was the first one to be developed. On the other hand, the sequential recombination algorithms are based on the idea to recombine close pairs of particles until the energy flow is reconstructed. This can be seen as a bottom-up approach to the problem, it was first used in e^+e^- or ep colliders and it has now become available for hadron colliders in many possible variants. The ATLAS specific implementations of both types of algorithms are discussed in the following, a more general and accurate discussion can be found in [62].

Recombination scheme Jets are made out of constituents, which can be particles, calorimeter cells or other objects. The constituents are represented by 4-vectors and they are combined into the 4-vector of the final jet via a recombination scheme. The ATLAS default is the sum of the 4-momenta of all the constituents:

$$p^{jet} = \sum_i p^i. \quad (3.1)$$

This scheme provides massive jets and conserves energy and momentum. Dealing with massive objects implies the use of the rapidity y coordinate for kinematic reconstruction:

$$y = \frac{1}{2} \ln \frac{E + p_z}{E - p_z}, \quad (3.2)$$

instead of the pseudorapidity η . The two quantities coincide in case of massless objects. Other schemes are possible, like the Snowmass scheme, where only the transverse

momentum of the constituents is summed up and jets are defined to be massless.

Cone algorithm Many different definitions of the cone algorithm exist. The ATLAS cone algorithm depends on the cone radius R , defined in the $y - \phi$ plane. It is based on a list of seeds, which are constituents with transverse momentum above a defined threshold. Starting from the more energetic seed, all constituents inside a cone with radius R from the seed are summed with it in order to form a pseudo-jet. Iteratively, a new cone is drawn around the pseudo-jet and the procedure is repeated until the configuration is stable and the cone can be considered a jet. The same procedure is repeated for all seeds. The jets obtained at the end can possibly share constituents and in order to define them uniquely a split and merge procedure is applied: jets which share constituents are either split into two jets or merged into a single jet, depending on the amount of overlap.

The seeded cone algorithm is not infrared nor collinear safe and for this reason it is no longer the default jet algorithm in ATLAS. A possible substitute is the Seedless Infrared Safe Cone (SISCone) algorithm [63], which is implemented in the ATLAS software.

Sequential recombination algorithms These algorithms are based upon a set of definitions. For each constituent i , it is possible to calculate two distance measures: the distance d_{ij} from each other constituents j and the distance d_{iB} from the beam axis:

$$\begin{aligned} d_{ij} &= \min(k_{Ti}^{2p} k_{Tj}^{2p} \frac{(\Delta R_{ij})^2}{R^2}, \\ d_{iB} &= k_{Ti}^{2p}, \end{aligned} \quad (3.3)$$

where R is the algorithm radius parameter, ΔR_{ij} is the ij distance in the $y - \phi$ plane and k_T is chosen to be the transverse momentum p_T of the constituent. Starting from a list of all possible d values, if the smallest entry is a d_{ij} , constituents i and j are combined and the list is remade. If the smallest entry is a d_{iB} , the constituent i is considered a complete jet and is removed from the list. Historically, implementations of these algorithms have been prohibitively slow, but the issue has been recently solved [64] and the new implementation is coded in the package FastJet [65].

Depending on the value of the parameter p in Equation 3.3, it is possible to distinguish three different algorithms, which are infrared and collinear safe to all orders in perturbation theory.

K_T algorithm for $p = 1$ [66, 67] In this case, constituents with low p_T are merged

first and the final merge is the hardest. This ordering information is very powerful for studying the jet substructure. The K_T jets have irregular shape and thus can be more difficult to calibrate.

Cambridge/Aachen algorithm for $p = 0$ [68, 69] In this case, the p_T order of the constituents is irrelevant and objects near to each other in ΔR are merged first. This ordering information can as well be exploited for studying the jet substructure.

Anti- K_T algorithm for $p = -1$ [70] In this case, in the vicinity of an hard constituent ($\Delta R < R$), all softer constituents are merged with the hard one. If two hard constituents are near to each other ($R < \Delta R < 2R$), the energy in between is shared. If two hard constituents are beside each other ($\Delta R < R$) a single jet is formed. The ordering of the merging has no special meaning in this case and cannot be used for jet structure studies. The Anti- K_T jets have very regular cone-like jet boundaries, and thus can be easier to calibrate.

The Anti- K_T algorithm has been chosen to be the ATLAS default, because it performs particularly well in terms of jet reconstruction efficiency, speed, trigger efficiency and stability under pile-up conditions [71]. Nevertheless the K_T and Cambridge/Aachen algorithms are used in parallel because they provide jet sub-structure information.

3.2 Particle showers

When a high energetic particle hits the detector and interacts with the detector material new particles can be produced. These can again give rise to new particles by interacting with the detector material. In this way a particle shower is initiated and it stops when the energy of the produced particle is too low to give rise to new particles.

Electromagnetic showers (initiated by electrons and photons) are very different from hadronic showers (initiated by hadrons) because of different mechanisms of particle production and energy loss, which determine different shower shapes.

A high energetic electron or photon interacts electromagnetically with the detector material and loses energy via bremsstrahlung and e^+e^- pair production. These two processes can follow each other giving rise to an electromagnetic shower. The characteristic length for these processes is the radiation length X_0 , which for electrons is

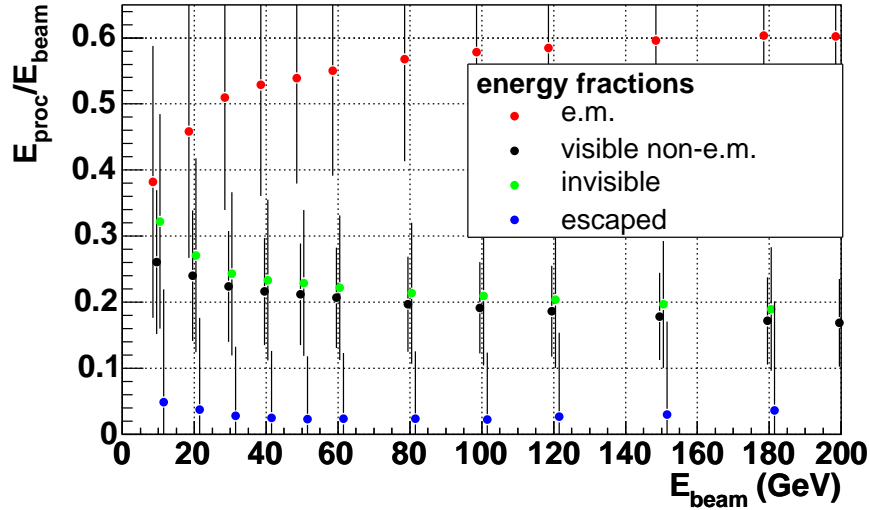


Figure 3.1: Fraction of the visible-em, visible-non-em, invisible and escaped energy for charged single pion showers in the end-cap region versus the initial pion energy, from GEANT4 simulation. Error bars indicate the RMS of the distribution. [72].

defined as the mean distance over which a high energy electron loses all but $1/e$ of its energy by bremsstrahlung and for photons as $7/9$ of the mean free path for pair production [5]. The shower mechanism interrupts when electrons reach the critical energy E_C at which the loss of energy via ionisation starts to dominate and when the photon energy is below the threshold for e^+e^- pair production. The electromagnetic processes are well understood theoretically and thus it is possible to describe and model electromagnetic showers with accuracy. The typical depth of an electromagnetic shower is defined as containing 98% of the energy of the incoming particle E_0 and is given by [5]:

$$L_{em} \approx 2.5X_0 \cdot (\ln(E_0/E_C) + C) , \quad (3.4)$$

where $C = +0.5$ for photons and $C = -0.5$ for electrons. The transverse size of an electromagnetic shower is given by the Molière radius [5]:

$$\rho_M = \frac{21\text{MeV}}{E_C} \cdot X_0 . \quad (3.5)$$

For an electromagnetic shower all the energy is finally deposited via ionisation processes and thus it is measured by the ATLAS calorimeter.

A high energetic hadron interacts with the detector material via the strong interaction through non-perturbative processes. Because these interactions are not easy to model theoretically, the description of hadronic showers is less accurate than for electromagnetic showers and relies on Monte Carlo simulation programs like GEANT4 [73]. In strong hadron-matter interactions the more likely process to occur is spallation, which consists of a fast intra-nuclear cascade (first step) followed by a slower evaporation (second step) [74]. During the first step the incoming hadron makes quasi free collisions with the nucleons of one of the material nuclei resulting in a cascade of fast nucleons from which hadrons (mainly pions, protons and neutrons) are produced. During the second step the highly excited nucleus radiates nucleons and photons. The characteristic length for these processes is the hadronic interaction length λ , which is defined via the probability that an hadron travels a distance x without interaction $p(x) = \exp(-x/\lambda)$. The typical depth of an hadronic shower is given by [75]:

$$L_{had} \approx (0.6 \ln(E_0) - 0.2 + 4 \cdot E_0^{0.15}) \cdot \lambda , \quad (3.6)$$

where the energy is given in GeV, while the typical shower transverse size is of the order of λ .

Depending on the nature of the secondary particles produced, the energy deposition of hadronic showers can be divided in four categories.

- Visible-em energy: this is due to π^0 or η^0 mesons, which decay into photons that generate electromagnetic sub-showers. These neutral mesons are $\sim 1/3$ of the secondaries because of isospin conservation and carry an increasing amount of energy with increasing initial particle energy.
- Visible-non-em energy: this is due to ionisation losses from secondary hadrons.
- Invisible energy: this is due to nuclear interactions of the hadrons with the detector material via processes as nuclei breakup or nuclear excitation. The energy lost in these processes is not measured in the calorimeters.
- Escaped energy: this is due to muons and neutrinos that leave a very small signal or no signal at all in the calorimeters.

The relevance of each energy category changes with respect to the initial hadron energy, as shown in Figure 3.1. In general, the visible energy accounts for about 80% of the initial particle energy while the invisible energy is about 20%. Anyhow these numbers

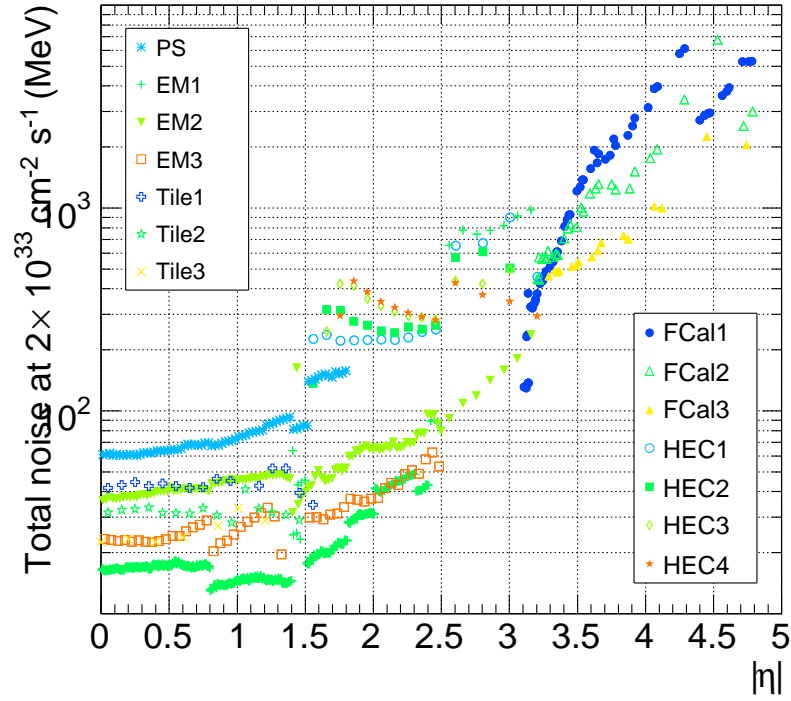


Figure 3.2: Expected noise from the electronic and pile-up for a luminosity of $2 \cdot 10^{33} \text{ cm}^{-2} \text{ s}^{-1}$ in individual cells of the various compartments of the calorimeters as a function of $|\eta|$ [52].

are affected by large shower-by-shower fluctuations, which make the hadronic shower energy measurement a rather challenging task.

The electromagnetic and hadronic shower shapes are different because of the different processes just described. Moreover in high Z materials, as the one used in the ATLAS calorimeters, electromagnetic showers are much more compact and dense than hadronic showers ($X_0 \ll \lambda$). These effects contribute to the different response of the calorimeter to electrons (or photons) and hadrons, which is one of the main effects that energy calibration has to take into account and correct for.

3.3 Cluster Algorithm

Jet constituents coming from detector measurements are complex objects. In ATLAS, the analog signal from each calorimeter cell is sampled and digitised. Then the energy deposited in each cell is computed from the sampled data using an optimal filtering

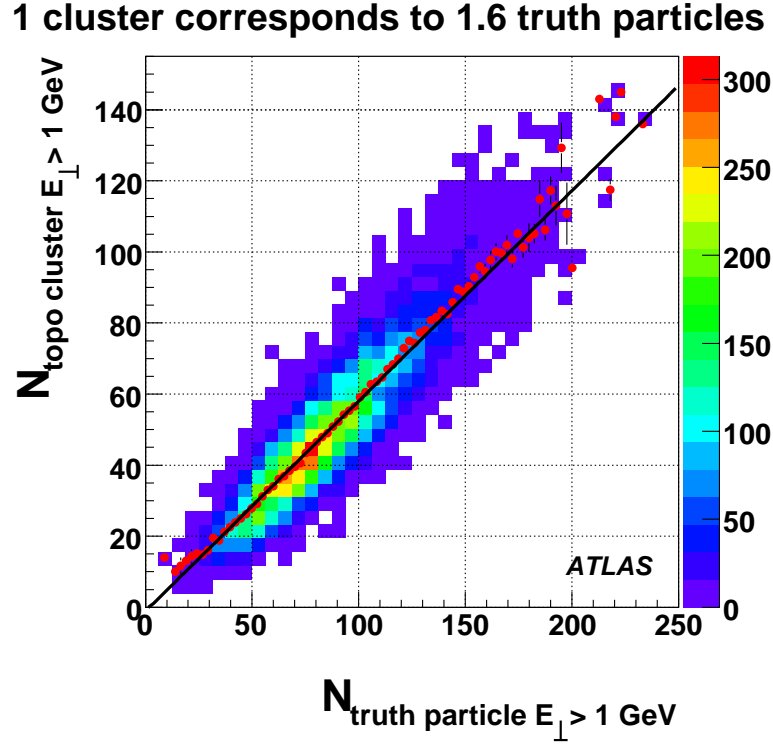


Figure 3.3: Number of topo-clusters with $E_T > 1$ GeV versus number of stable truth particles with $E_T > 1$ GeV, from a QCD di-jet simulation [76].

algorithm that minimises the effects of electronic and pile-up noise [77,78]. During this procedure, the signal is corrected for the energy lost in the absorber material using sampling fraction factors. These are obtained, separately for each sub-calorimeter system, in beam test experiments with electrons of known energy. Therefore, after the electronics calibration, the energy of the calorimeter cells is said to be the electromagnetic scale.

In order to be used as input to jet algorithms, cells need to be organised in 3 dimensional structures, which correspond to the energy deposited from the hadrons forming the initial jet. Cells contributing to these structures have to be selected carefully in order to suppress electronic and pile-up noise: as shown in Figure 3.2, cell noise in the ATLAS calorimeters spans 4 orders of magnitude, from few MeV in the central Barrel region to more than 10 GeV in the very forward region.

A standard approach at hadron colliders has been to group cells into calorimeter towers of fixed size. Calorimeter towers are implemented in ATLAS with size $\Delta\eta \times \Delta\phi =$

0.1×0.1 , but their usage is deprecated because they don't provide an adequate level of noise suppression. Moreover calorimeter towers don't show a correspondence to the particle showers and thus cannot be considered as natural inputs to jet algorithms. A more sophisticated approach has been developed in ATLAS: the cluster algorithm [79]. Two types of cluster algorithms are implemented.

Sliding window cluster algorithm This is based on combining cells inside a rectangular window of fixed size ΔR . The position of the window is adjusted until the transverse energy contained is a local maximum. This algorithm is optimal for reconstructing electrons and photons and the usage of a fixed size allows for a very precise cluster energy calibration.

Topological cluster algorithm This is based on combining cells around a seed, providing they satisfy specific noise thresholds cuts. This algorithm is very efficient at suppressing noise and is optimal for jet and missing transverse energy reconstruction. The clusters, called topo-clusters, contain a variable number of cells and don't have a fixed shape. The shape and energy properties of the topo-clusters can in fact be exploited to understand and calibrate the underlying hadronic shower, as described in Section 3.4. But, in case a fixed shape is preferred, the cells selected by the algorithm can be grouped into standard towers, called topo-towers.

The topological cluster algorithm is based on the signal to noise ratio ($|E|/\sigma_E$) of each cell. The absolute value of the energy is used in order to preserve the statistical noise cancellations between positive and negative cell energies. The cell noise is calculated as the expected RMS of the electronic and pile-up noise for the current gain and conditions. The cluster algorithm starts from identifying seeds: cells with a signal to noise ratio above a threshold t_s . Then, for each seed, all the neighbouring cells are considered and they are added to the seed if their signal to noise ratio is above a threshold t_n . Finally, all direct neighbours are summed up if their signal to noise ratio is above a threshold t_c . The default threshold schema (t_s, t_n, t_c) is $(4, 2, 0)$, which shows the best performance in terms of noise suppression and reconstruction efficiency. In the very dense jet environment, it happens that clusters grow to cover large areas, because energy is present between different showers. In order to improve the correspondence between single clusters and initial hadrons, topological clusters are split around local maxima. Finally, as shown in Figure 3.3, a cluster corresponds to ~ 1.6

truth particles. It is important to notice that, apart from minor contributions from other hadrons, a jet is composed of $\sim 1/3$ of π^0 and $2/3$ of π^\pm . Neutral pions decay into two photons in 99% of the cases. In the ATLAS simulation, the photons, and not the π^0 , are considered stable particles, but they are often reconstructed as a single cluster. This raises the expected number of particles per cluster to ~ 1.3 .

Topological clusters are an absolute novelty at hadron colliders and have been implemented taking advantage of the high granularity and excellent resolution of the ATLAS calorimeters. They show very good performance in terms of noise suppression and truth particle correspondence and are used as default input to jet algorithms and calibration [77, 78].

3.4 Jet Calibration

Precise jet energy measurement is fundamental for many different physics analyses, like the top quark mass measurement, the inclusive jet cross section measurement or the search for Supersymmetric particles. Precise jet energy measurement implies jet energy calibration, from the electromagnetic scale of the constituents to the initial jet energy.

The definition of the initial jet energy is not unique. It is possible to consider the energy of the parton that initiated the jet, but this concept is not always well defined because partons are not free objects. Instead, fragmentation and hadronisation effects are included in the particle jet energy definition, which is the energy of the jet obtained by running the chosen jet algorithm on the final state Monte Carlo particles. The particle jet energy sets the reference jet energy scale in ATLAS.

The correspondence between the particle jet (true jet) and the jet made from clusters (reconstructed jet) is set via a ΔR matching, which is the base of any Monte Carlo jet calibration. It is important to notice that this matching does not account for the bending effects of the magnetic field on charged particles. This causes energy losses outside the jet perimeter and foreign energy leak from other calorimeter deposits into the jet. In order to study in detail the correspondence between the true and the reconstructed jet, a Primary Particle ID tool has recently been implemented in ATLAS [80]. This tool keeps track of which particles have deposited how much energy into each calorimeter cell, leading to a quantification of the lost and foreign jet energy. The

Primary Particle ID tool is very powerful and can be the base for future improvements in the ATLAS jet calibration strategy, as discussed in Chapter 4.

In order to bring the jet energy to the particle level, any jet calibration procedure for ATLAS has to account for the following effects.

In first instance, the non-compensation of the ATLAS calorimeter system has to be recovered: when an electron or a charged pion energy is measured in the calorimeters, the response for the electron is higher. This is due to the nature of hadronic and electromagnetic showers, as discussed in Section 3.2. Correcting for non-compensation effects implies recovering the invisible and escaped energy not measured by the calorimeters. This is a challenging tasks, because the composition of hadronic showers is subject to large fluctuations.

Particles coming from jets can deposit energy outside the active calorimeter regions, in the so called dead material. This includes energy deposited in the region between the interaction point and the calorimeters (inner detector material, magnetic coil or cryostat walls), as well as in the transition regions between the various calorimeter modules, in the so called crack regions. Finally, even if the shower containment is very good, some energy can leak out of the calorimeters, inside the muon spectrometer. Energy lost in dead material and leakage is never detected by the calorimeters and needs to be recovered.

Some of the particles that form the initial jet are never reconstructed in the calorimeters. Very often they are low energetic and deposit all of their energy in the material upstream the calorimeter. In other cases they are bent by the magnetic field and reach the calorimeter far from the high energetic hadrons of the same jet. In both cases the final jet lacks of some energy that has to be recovered.

Finally both the cluster and the jet algorithm show inefficiencies that need to be taken into account.

Various calibration methods have been developed by the ATLAS collaboration. For all methods the reference object is the true particle jet, obtained from stable Monte Carlo particles (after parton shower and hadronisation) excluding muons and neutrinos. The methods can be distinguished in two categories, the global and the local calibrations.

3.4.1 Global Calibration

In the global calibration methods, jets are first found by the jet algorithm using as input topo-clusters (or topo-towers) with energy at the electromagnetic scale. Then the single jets are calibrated with respect to the true particle jet. Two main global approaches have been developed.

p_T and η dependent calibration (EM+JES) In this calibration scheme all the detector effects are corrected in one step. The jet energy scale is recovered applying a factor, that depends on the p_T and η of the reconstructed jet. The calibration factors can be calculated from Monte Carlo simulations, or from data using γ +jet and di-jet balance techniques. This method is simple to implement and has therefore been used for first data analysis [81]. After calibrating jets with the EM+JES method, it is possible to improve the resolution using other variables as the longitudinal and transverse jet structure. This second step is known as global sequential calibration [82].

Global cell energy-density calibration (GC) In this calibration scheme the jets are first corrected for non-compensation effects. This correction is obtained in terms of weights applied to the cells belonging to the jets. The weights are different for the various calorimeter layers and depend on the cell energy density, which reflects the tendency of electromagnetic deposits to be dense and compact and of hadronic deposits to be broader and less dense. The weights are obtained by minimising the jet energy fluctuations with respect to the true jet, so they correct partially for dead material losses and lost particles as well. Finally, a correction based on the p_T and η of the jet is applied in order to fully recover the jet energy scale [76, 82].

3.4.2 Local Hadron Calibration

In the Local Hadron Calibration (LC) method [72], topo-clusters are first calibrated to the hadronic scale. Then the calibrated topo-clusters are used as input to the jet algorithm. Finally, the jets are corrected for residual effects with respect to the true particle jet. The aim of the local hadron calibration method is to correct for the various detector effects in a modular way, in order to improve the control over the systematic uncertainty. In fact, corrections for non-compensation, cluster algorithm inefficiencies and dead material losses are performed at the cluster level, independently of the jet algorithm, while jet specific effects like lost particle and jet algorithm inefficiencies are

corrected at the jet level.

Cluster level corrections

The cluster level corrections are the first step performed by the local hadron calibration. They include a classification procedure which aims at separating the deposits deriving from the initial $\sim 1/3 \pi^0$ (and other particles creating electromagnetic showers) from the deposits deriving from the initial $\sim 2/3 \pi^\pm$ (and other particles creating hadronic showers) and at optimally calibrating each type of particle.

In order to derive the cluster level corrections, a true reference object has to be defined. The true reference is provided in terms of GEANT4 simulation information. In the virtual world of simulation, after the Monte Carlo has reproduced the hard scattering, the fragmentation and the hadronisation processes, the GEANT4 simulation describes in detail how the produced particles interact with the ATLAS detector. In particular, for each calorimeter cell, a virtual twin is created, the so called calibration hit. A calibration hit provides the information of how much energy was deposited in a calorimeter cell by any particle in the event. The energy deposited is available separately as visible-em, visible-non-em, invisible and escaped. The calibration hit energy is accessible for both active (liquid argon) and inactive (absorber) material for the Lar calorimeters, while the active (scintillator) and inactive material are treated together for the Tile calorimeter. In a similar way, all the dead material regions are artificially divided into pseudo-cells of size $\Delta\phi \times \Delta\eta = 0.1 \times 0.1$. For these pseudo-cells, dead material calibration hits are stored, which contain the energy lost by any particles in that dead material area.

In single pion simulations, which are events where a pion is shot from the interaction point with defined energy and pseudorapidity, all the calibration hits belong to the same particle (the single pion itself) and can be divided into three groups:

1. the calibration hits that are contained inside reconstructed clusters;
2. the calibration hits that are outside reconstructed clusters but inside the calorimeter;
3. the calibration hits that are in dead material areas.

Group 1 represents the energy that should be recovered after correcting for non-compensation effects (calibration hits include invisible and escaped energy). Group

2 represent the energy that should be recovered after correcting for the cluster algorithm inefficiency. Group 3 clearly represent the energy that should be recovered by dead material and leakage corrections. Even in single pion events it can happen that more than one cluster per event is reconstructed and in this case the true energy of the cluster does not coincide with the true energy of the initial pion. So, in general, the true energy of the cluster is defined for group 1 by the calibration hits contained inside the cluster and for groups 2 and 3 by using an assignment algorithm, which depends on the cluster energy and on the distance between the calibration hit and the cluster.

Each cluster is corrected in three different steps with respect to the true reference given by the calibration hits of groups 1,2 and 3. The corrections are derived from clusters and calibration hits in single pion simulations and then applied to clusters in collision events. The corrections consists of weights applied to the cluster energy and are derived in terms of cluster properties as energy, pseudorapidity and cluster moments, which are variables defined in terms of the properties of the cluster constituents. A cluster moment of degree n in an observable x is defined as:

$$\langle x^n \rangle = \frac{\sum_i E_i x_i^n}{\sum_i E_i}, \quad (3.7)$$

where i runs on all cells included in the cluster, E_i is the energy of the cell (only cells with positive energy are considered for the definition) and x_i is the moment observable calculated for the cell i . Interesting moment observables are the distance of the cell from the cluster axis r , the distance of the cell from the cluster centre along the shower axis λ and the cell energy density calculated as the ratio between the cell energy and the cell volume $\rho = E_i/V_i$.

Before any cluster correction is applied, clusters are classified as electromagnetic or hadronic. The classification depends on the cluster E and $|\eta|$, on the first moment in energy density $\langle \rho \rangle$ and on the distance of the cluster centre from the calorimeter front face along the cluster axis λ_{center} . In order to develop the classification procedure, a single pion simulation sample composed by $\sim 1/3$ of π^0 and $\sim 2/3$ of π^\pm is used and the three cluster level corrections are developed for π^0 (electromagnetic corrections) and π^\pm (hadronic corrections) separately. The outcome of the classification procedure is a probability for the cluster to have electromagnetic nature p_{em} , which relates to the probability of the cluster to have hadronic nature as $p_{em} = 1 - p_{had}$. The electromagnetic or hadronic corrections are finally applied to a cluster in proportion to its p_{em} and p_{had} respectively.

Corrections for non-compensation effects are applied in form of cluster cell weights (**W**) and depend on the cell $|\eta|$, the cell energy density ρ_{cell} and the cluster energy. It is important to notice that the cells composing the cluster are calibrated individually; in particular cells with a very high energy density (electromagnetic like) receive hadronic weights close to unity. This mechanism corrects for the fluctuations of the fraction of visible-em and invisible energy on an event-by-event basis.

Corrections for inefficiencies of the cluster algorithm due to noise threshold cuts are implemented in terms of the cluster E , $|\eta|$ and λ . These are called Out Of Cluster corrections (**OOC**) and are applied to clusters inside jets depending on the cluster isolation. In fact, clusters in single pion events tend to be isolated with respect to clusters inside jets and therefore need higher OOC corrections for energy that in a jet event could be included inside a neighbour cluster.

Corrections for dead material losses and leakage (**DM**) depend on the region of the detector where the cluster is reconstructed. In order to correct for deposits upstream the calorimeter, the energy measured in the presampler is used together with the cluster E and $|\eta|$. In order to correct for the energy lost in the cryostat wall between the barrel electromagnetic calorimeter and the tile calorimeter, the geometrical mean of the energies in the samplings just before and just after the wall is used together with the cluster E and $|\eta|$. Finally, corrections for the other regions are obtained with respect to the cluster E , $|\eta|$ and λ .

Performance of the local hadron calibration for single pions has been extensively studied in beam test experiments [83] and using simulations [76]. The classification procedure has shown to be able to classify 90% of the charged pions as hadronic ($p_{had} > 0.5$) and 90% of neutral pions with $E > 100$ GeV as electromagnetic ($p_{em} > 0.5$), while for neutral pions with energy of 10 GeV the efficiency drops to 50%. This result is very satisfactory, especially considering the fact that hadronic cell weights can be very small for cells with high energy density inside hadronic clusters. Concerning the energy calibration, all of the three cluster corrections perform very well, within residual non-linearities of few percent for low pion energies. The performance of the cluster level calibrations in the jet environment has been tested using Monte Carlo simulations and ATLAS data and is discussed in detail in Chapter 4.

Jet level corrections

Topological clusters that received the W, OOC and DM corrections are used as input to the jet algorithm. The jets formed from calibrated clusters don't contain corrections for particles lost or bent out of the jet area. These are provided by a dedicated constituent based (CB) calibration that uses as reference the Monte Carlo true jet. The corrections are applied as weight to the jet energy and are based on the jet E , $|\eta|$ and on a jet shape variable. Jets are more than four vector objects: as for clusters, their shape and properties can help to restore the jet energy scale. The variable used for the CB corrections is the fraction of jet transverse energy E_T^{jet} due to clusters with low transverse energy ($E_T^{clus} < 1 \text{ GeV}$), which has been shown to be sensitive to the energy of the lost particles.

Thanks to the CB corrections, the jet energy scale is restored within 1% and the resolution is improved with respect to the cluster level calibration only [82].

The development of the CB corrections is very recent [84] and took place partially as an outcome of the performance studies presented in Chapter 4. Local hadron calibrated jets with CB corrections are used in the all-hadronic $t\bar{t}$ analysis presented in Chapter 5, where they allow for a very good control over the event energy flow and over the jet energy scale systematic uncertainty.

Chapter 4

Local Hadron Calibration Studies

The performance of the Local Hadron Calibration method has been studied with data and with Monte Carlo simulations. Both jet level corrections and cluster level corrections, described in Section 3.4.2, have been investigated. This Chapter focuses mainly on the performance of the cluster level corrections, while a detailed description of the performance of the jet level corrections can be found in [84]. In Section 4.1 a discussion on the effects of nonlinear energy corrections on the jet energy resolution is provided. A general method to treat these effects has been developed and is used through the whole Chapter. In Section 4.2 Local Hadron Calibration performance studies for jet reconstruction are presented, including a study using calibration hits as true reference and a discussion on the main sources of systematic error. Then in Section 4.3 a preliminary study on the Local Hadron Calibration performance for MET reconstruction is presented. All performance results are obtained on Monte Carlo simulations. Finally, in Section 4.4, validation studies on ATLAS data collected for collisions at $\sqrt{s} = 900$ GeV are presented.

4.1 Resolution for nonlinear energy response

When the response of a calorimeter is nonlinear in energy, evaluating the performance of a calibration method requires some care. In fact, when a nonlinear energy correction is applied, the energy resolution changes due to an artefact that depends on the curvature of the correction function.

In order to demonstrate this effect a toy Monte Carlo simulation is used. True jet energies E^T are simulated with a probability distribution flat in $\log E^T$, with E^T

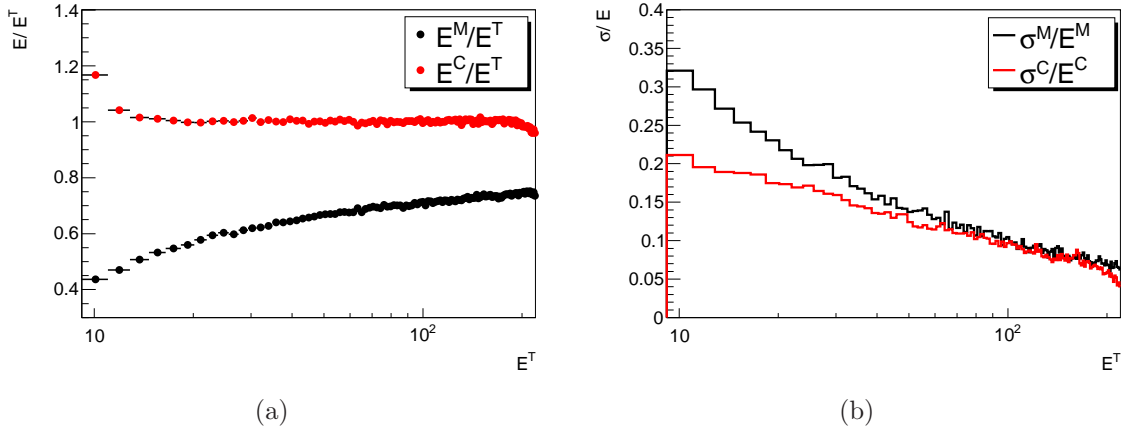


Figure 4.1: Linearity (a) and resolution (b) for non linear calorimeter response from a toy Monte Carlo simulation. The black histograms are for the energy as measured by the calorimeter and the red histograms are for the energy corrected for nonlinearity only.

between 2 GeV and 2 TeV. The energy measured in the calorimeter E^M is simulated by scaling the true energy with the function:

$$0.93 - \frac{0.87}{\log E^T} - \frac{0.63}{(\log E^T)^2}, \quad (4.1)$$

and with a random gaussian relative spread of $1/\sqrt{E^T}$, which combined produce an effect similar to the response of the ATLAS calorimeter in the barrel region. A linearity plot can be constructed as the mean of the distribution of the ratio of the measured energy E^M over the true energy E^T versus the true energy E^T . The resolution plot is constructed as the RMS of the distribution of the ratio E^M/E^T divided by the mean of the ratio E^M/E^T , versus the true energy E^T . Both numerator and denominator of the resolution definition are normalised to E^T by convention, but the ratio is in general indicated as σ/E . The linearity and the resolution plots are shown in black in Figure 4.1 (a) and (b), respectively. A calibration can be derived from the linearity distribution using the inversion method. This technique consists in inverting the linearity plot with the following procedure:

- for every bin the central value of the true energy E_c^T is considered;
- for every bin the mean measured energy E_m^M is calculated as the mean of the ratio E^M/E^T multiplied by E_c^T ;

- a new plot of E_c^T/E_m^M versus E_m^M is built.

A plot of the mean of the distribution of the ratio E^T/E^M versus E^M could be obtained directly, but would be biased by the intrinsic fluctuations of E^M . Moreover the inversion method is to be preferred in realistic Monte Carlo simulations, where the distribution of E^T/E^M for fixed E^M is not gaussian, because of the underlying falling p_T spectrum of jets. The inverted linearity plot can be used directly to read the weight w (or a function could be fitted to the histogram), which has to be applied to the measured energy in order to recover the initial true energy. In Figure 4.1 the linearity (a) and resolution (b) of the corrected energy E^C with respect to the true energy E^T are shown in red (an independent set of simulations has been used for deriving the corrections). It is evident that the corrections applied determine a change (an improvement in this case) of the energy resolution.

It is possible to build a model of this effect, which is independent of the specific response function and calibration method. The change in resolution can be explained as a consequence of error propagation. As shown in Appendix A, if the measured energy E^M is corrected with a calibration function $w(E^M)$ in order to obtain the corrected energy E^C , the error on the measured and corrected energies are related by the equation:

$$\frac{\sigma^C}{E^C} = \left(1 + \frac{E^M}{w(E^M)} \cdot \frac{dw(E^M)}{dE^M} \right) \cdot \frac{\sigma^M}{E^M} , \quad (4.2)$$

where σ^C and σ^M are the errors on the corrected and measured energy respectively. From Equation 4.2 it is possible to see that the resolution of the measured energy and the resolution of the corrected energy are related by a factor that depends on the derivative of the correction function w . Therefore, if the correction function is linear in energy, which implies $w(E^M) \equiv \text{constant}$, then the derivative $dw(E^M)/dE^M$ is zero and the resolution is not affected by the correction function.

Equation 4.2 contains the full relation between the resolution before and after non-linear energy corrections are applied. Nevertheless it is not useful in performance studies, because it is not expressed in terms of the true energy E^T . As shown in Appendix A, if the measured energy E^M is given by the response function $s(E^T)$ applied to the true energy E^T , it is possible to write:

$$\frac{\sigma^C}{E^C} = \frac{s(E^T)}{s(E^T) + \frac{ds(E^T)}{dE^T} \cdot E^T} \cdot \frac{\sigma^M}{E^M} . \quad (4.3)$$

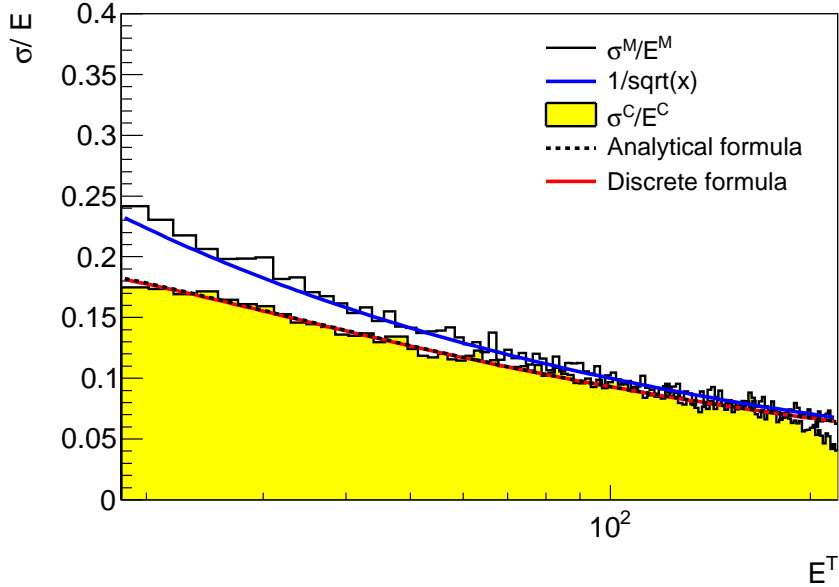


Figure 4.2: Resolution for non linear response (black histogram) and analytical description as known from the toy Monte Carlo (blue line). Resolution corrected for non-linearities (yellow histogram) with analytical (black dotted line) and discrete (red line) description.

Equation 4.3 sets an analytical correspondence between the measured and corrected energy resolution, in terms of the true energy E^T . If the response function $s(E^T)$ is not known analytically, it can be useful to write a discrete version of Equation 4.3:

$$\frac{\sigma^C}{E^C} = \frac{s(E^T) \cdot \Delta E^T}{s(E^T + \Delta E^T) \cdot (E^T + \Delta E^T) - s(E^T) \cdot E^T} \cdot \frac{\sigma^M}{E^M}, \quad (4.4)$$

which can easily be implemented by approximating $\Delta E^T \sim \frac{\sigma^M}{E^M} \cdot E^T$.

Equations 4.3 and 4.4 can be tested using the toy Monte Carlo simulation. In Figure 4.2 the resolution histograms of Figure 4.1(b) are shown together with the functions that describe them. The resolution of the measured energy is shown (in black) together with the resolution function introduced in the toy Monte Carlo (in blue). The resolution of the corrected energy is shown (in yellow) together with the analytical formula of Equation 4.3 (in dotted black), calculated from the response function of Equation 4.1, and together with the discrete approximation of Equation 4.4 (in red), calculated from the histogram shown in Figure 4.1(a). Equations 4.3 and 4.4 describe the resolution of the corrected energy very well and can be considered a general method to predict the change in resolution introduced when correcting for the

calorimeter nonlinear response.

It is important to notice that the change in resolution due to the curvature of the correction function is a geometrical artefact, which can lead either to the improvement or to the deterioration of the energy resolution, without physical meaning. The change in resolution due to nonlinear effects is different from the change in resolution expected when additional information (like the knowledge of the hadronic shower shape or of the momentum measured in the tracker) is used to calibrate. In order to be able to measure this physical change in resolution, the geometrical artefact has to be removed.

In particular, when a sophisticated energy calibration is applied to the calorimeter signal, residual nonlinearities can appear. These can be caused by effects like dead material losses, lost particles or jet flavour dependence, which are not completely recovered by the calibration. The effects of these residual nonlinearities have to be removed before comparing the resolution achieved by various calibration methods. Equations 4.3 and 4.4 are a very powerful tool in this respect and have been implemented in the official ATLAS software.

4.2 Monte Carlo performance studies for jets

The performance of a calibration technique for jet reconstruction can be evaluated with the use of Monte Carlo simulations by comparing the reconstructed and true energy of a jet. In this respect it is necessary to assign a true jet to each reconstructed jet. The strategy adopted in these studies is to perform a matching by looking for the closest true jet in ΔR , with maximum $\Delta R = 0.1$. The reconstructed jet is then considered only if a true match is found. In ATLAS a default cut on the transverse energy of the reconstructed jet is set to be $E_T^{reco} > 7$ GeV, in order to avoid threshold effects a corresponding cut on the transverse energy of the true jet is necessary. This has to be higher than the cut on E_T^{reco} , because jets tend to be reconstructed with a smaller energy than their true energy, so a cut on the true transverse energy has been set to $E_T^{true} > 14$ GeV. Jets have been reconstructed using the Anti- K_T algorithm with radius parameter $R = 0.4$ [70].

The performance for jet reconstruction is evaluated in terms of energy linearity and energy resolution. The linearity plot is constructed as the mean of the distribution of the ratio of the energy of the reconstructed jet E^{reco} over the energy of the true jet E^{true} versus the energy of the true jet E^{true} . The resolution plot is constructed as the RMS of the distribution of the ratio E^{reco}/E^{true} divided by the mean of the

ratio E^{reco}/E^{true} , versus the true energy E^{true} . These plots are usually built in bins of the true jet pseudorapidity η^{true} , in order to separate regions with different detector geometry and different relevant physics processes. The η^{true} bins chosen for the studies presented in this Section are:

- barrel region for $|\eta^{true}| = 0.3 \pm 0.2$, this is a region with small amount of dead material and is usually considered a benchmark for performance studies;
- crack region for $|\eta^{true}| = 1.4 \pm 0.2$, this is a difficult region because it includes dead material due to the crack between the barrel and the end-cap calorimeter;
- end-cap region for $|\eta^{true}| = 2.1 \pm 0.2$, this is a region with small amount of dead material, including part of the end-cap calorimeter;
- forward region for $|\eta^{true}| = 3.7 \pm 0.2$, this is a region with small amount of dead material, including part of the forward calorimeter.

Another type of study consists in building a plot of the mean of the ratio E^{reco}/E^{true} versus the true jet pseudorapidity η^{true} , in bins of true jet transverse energy E_T^{true} . In this way it is possible to see which detector effects are more relevant in which range of energies. In this case four E_T^{true} bins have been chosen:

- $E_T^{true} = 15 \text{ GeV} \pm 20\%$;
- $E_T^{true} = 30 \text{ GeV} \pm 20\%$;
- $E_T^{true} = 50 \text{ GeV} \pm 20\%$;
- $E_T^{true} = 100 \text{ GeV} \pm 20\%$.

In Section 4.2.1 linearity and resolution studies in bins of η are presented. In this case the particle jet is used as true reference. In Section 4.2.2 linearity studies in bins of η and in bins of E_T are presented. In this case a definition of the true jet energy based on calibration hit information is used as true reference.

The Monte Carlo samples used for the studies presented in this Section are di-jet events simulated for $\sqrt{s} = 10 \text{ TeV}$ pp collisions. This centre of mass energy was foreseen for the LHC start up in September 2008, before the accident due to the faulty magnet interconnect occurred. Di-jet events are non-diffractive $2 \rightarrow 2$ QCD processes. The total cross section for di-jet events is huge and the simulation sample cannot be produced inclusively. Instead in ATLAS a p_T slicing strategy is adopted.

Dataset Name	p_T min (GeV)	p_T max (GeV)	σ (pb)
J0	8	17	1.76E+010
J1	17	35	1.38E+009
J2	35	70	9.33E+007
J3	70	140	5.88E+006
J4	140	280	3.08E+005
J5	280	560	1.25E+004
J6	560	1120	360
J7	1120	2240	5.71
J8	2240	-	0.02

Table 4.1: Definition of PYTHIA QCD slices in p_T . For each dataset ~ 100000 events have been simulated.

This consists of dividing the event generation in 9 samples depending on the sum of the p_T of the two generated partons. Details on the sample naming convention, slicing boundaries and cross sections are given in Table 4.1. For all the results presented in this Section ~ 100000 events of each JX sample are processed and then combined together. Event generation, parton showering, hadronisation and underlying event are simulated with PYTHIA (version 6.421) [44]. The description of the interaction of the particles with the ATLAS detector is performed using the GEANT4 software toolkit [40]. The GEANT4 model used as default is called QGSP-BERT. Its main features are the use of the Quark Gluon String model [85] for the fragmentation of the nucleus, and the Bertini cascade model [86] for the description of the interactions of the hadrons in the medium of the nucleus. Among the available simulations of hadronic processes, the QGSP-BERT model has shown to best reproduce the results of test beam experiments with single pions as described in [87–89] for the calorimeter barrel and in [90, 91] for the calorimeter end-caps.

All samples have been simulated with the ATLAS software Athena version 15.1.0 and have been reconstructed using the Worldwide LHC Computing Grid in order to apply the more recent Local Hadron Calibration correction weights, obtained on single pion samples simulated with the same software release.

4.2.1 Performance studies with the true particle jet

The true particle jet sets the final jet energy scale to be recovered by the Local Hadron Calibration. With the combined use of the cluster level corrections and of the con-

stituent based jet level corrections this goal is achieved within a linearity of 1% [82]. In this Section a comparison of the energy of the reconstructed jet, after each cluster level correction is applied, with the energy of the particle jet is shown. In this way it is possible to appreciate the effect of each correction in different detector regions and energy regimes. The cluster level corrections are independent of the jet algorithm, therefore it is possible to calculate the energy of a jet after a specific cluster correction as the sum of the energies of its calibrated cluster constituents. The energy of the jet can be:

- at the electromagnetic scale, indicated in magenta (**EM**);
- after hadronic weights are applied, indicated in blue (**EM+W**);
- after out of cluster corrections are applied, indicated in green (**EM+W+OOC**);
- after dead material corrections are applied, indicated in red (**EM+W+OOC+DM**).

The cluster corrections are applied in this order on top of each other, so the latter case represents the final cluster energy scale. However the correction weights are obtained with respect to the cluster at the electromagnetic scale, in order to preserve an higher degree of independence. In this way it is possible to change the order in which the corrections are applied and to remove or add or change any set of weights.

In Figure 4.3 the linearity of the energy at the different scales described above is shown for the barrel, crack, end-cap and forward regions. In general it is possible to notice that the hadronic weight corrections and the dead material corrections are the two more important in terms of magnitude. The fact that the out of cluster corrections are smaller is positive, because it indicates that the cluster algorithm is working correctly. In all regions the linearity improves with increasing energy. This effect can be explained by considering that the lack of linearity is caused by lost particles, which are more likely bent outside the jet or absorbed completely by dead material if they are low energetic. The linearity behaviour in the crack region shows some anomalies at low energies, due to the fact that the cut on the true transverse energy is too loose in this region, considering the very low energy response at the electromagnetic scale. Again in the crack region, for energies larger than 100 GeV, the linearity at the electromagnetic, hadronic and out of cluster scale shows oscillations. These are very likely due to modulations in the hadronic shower caused by the dead material: the starting point of the hadronic shower can move into the dead material changing

the calorimeter energy response substantially. The linearity behaviour is restored after dead material corrections. Considering as a benchmark the performance for a jet of 100 GeV of energy, the final linearity achieved in the barrel and end-cap regions is better than 10%. The performance in the forward region is poorer (inside 20%) because of the very dense environment that makes a local calibration very challenging. The final performance in the crack region is very good (inside 20%) considering that the response at the electromagnetic scale is quite low.

The Local Hadron calibration method has been initially developed and tested in single pion beam tests. For single particles the three cluster corrections are sufficient to recover the linearity inside a few percent [76]. Instead, from plots like the one shown in Figure 4.3, the need of jet level corrections emerges.

In Figure 4.4 the resolution plots corresponding to the linearity plots of Figure 4.3 are shown. For each histogram the formula of Equation 4.4 has been used in order to remove the residual nonlinearities with respect to the true particle jet level. This step is particularly important when comparing the resolution achieved after each Local Hadron Calibration correction. In this way the resolution shown for the electromagnetic scale is the one which would be achieved by correcting the calorimeter response with the inversion method only. The resolution shown for the hadronic weights is the one which would be achieved by correcting the calorimeter response with the inversion method and with the hadronic weights. By comparing the two resolution histograms, it is possible to evaluate the improvement of the resolution due only to the hadronic weight corrections. The same is valid when adding out of cluster and dead material corrections. The plots shown in Figure 4.4 show a general improvement of the resolution after each correction is applied. This trend is particularly evident in the crack region, in which the dead material corrections improve the resolution substantially with respect to the previous energy scales. In this region, the oscillations of the resolution at the electromagnetic, hadronic and out of cluster scale for energies larger than 100 GeV derive from the nonlinear corrections of Equation 4.4, which propagate to the resolution the linearity oscillations shown in Figure 4.3. As a benchmark figure, for a jet of 100 GeV of energy in the barrel region, the resolution is about $\sigma/E = 10\%$ after dead material corrections. This figure is an upper limit, because the RMS has been used as an estimator.

In order to be able to read the final improvement in resolution obtained by the cluster level corrections with respect to the electromagnetic scale, the ratio of the resolution after all corrections over the resolution at the electromagnetic scale is shown in Figure 4.5. These plots show by bin-by-bin oscillations that are due to the use of

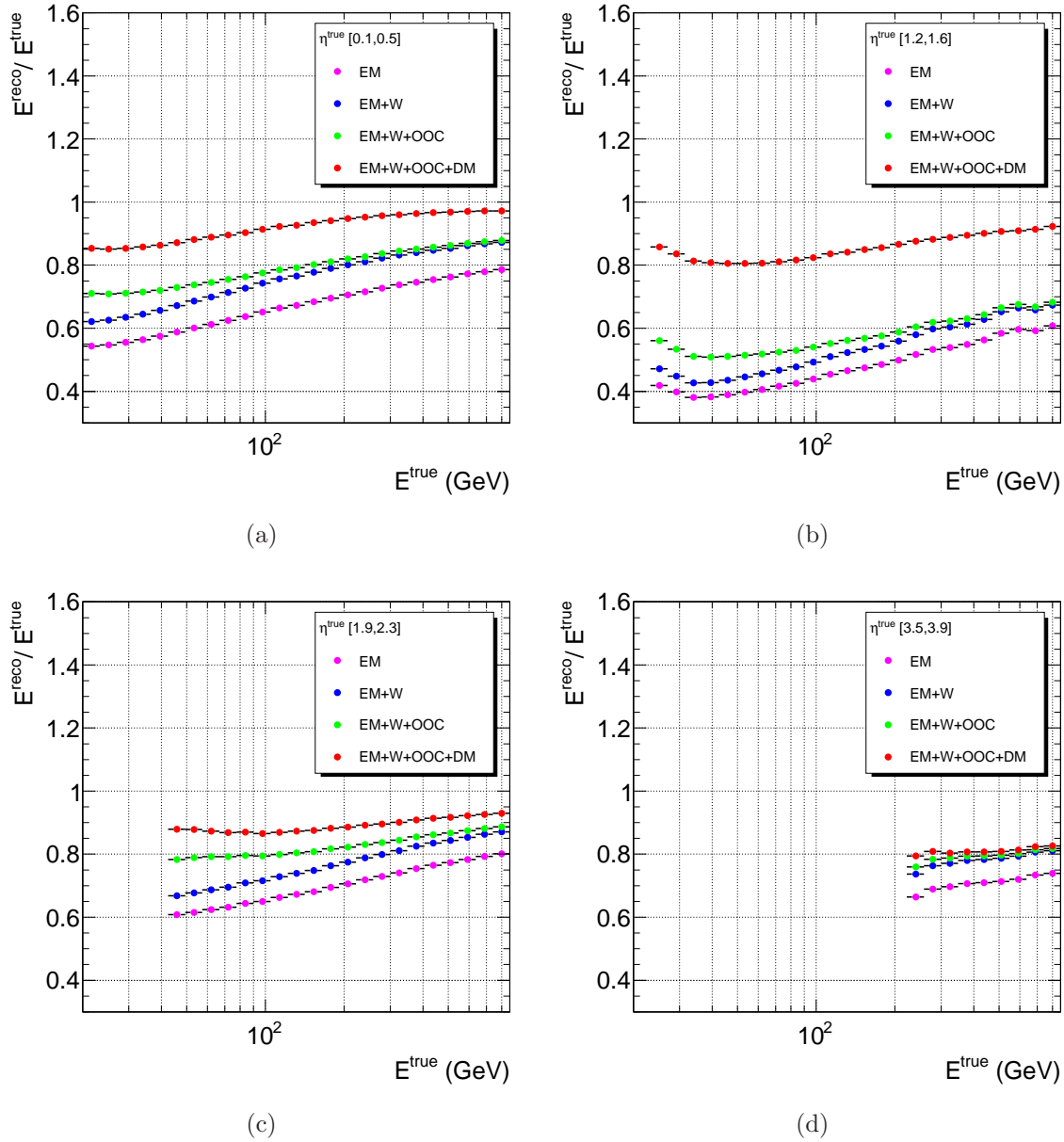


Figure 4.3: Energy linearity for the barrel (a), crack (b), end-cap (c) and forward (d) regions. The reconstructed jet energy is considered at the electromagnetic scale (in magenta), after hadronic weights are applied (in blue), after hadronic weight and out of cluster corrections are applied (in green) and after hadronic weight, out of cluster corrections and dead material corrections are applied (in red).

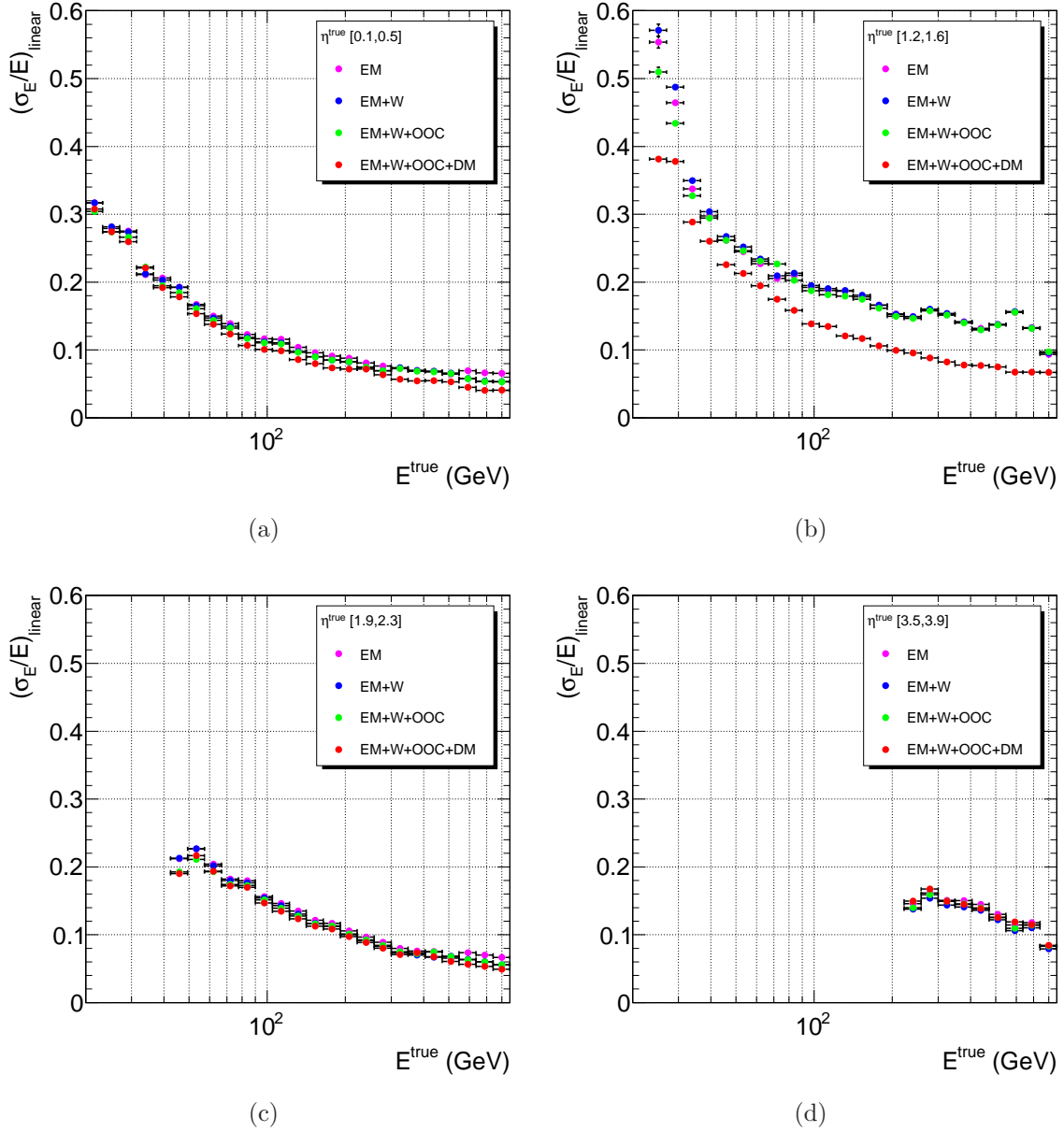


Figure 4.4: Energy resolution for the barrel (a), crack (b), end-cap (c) and forward (d) regions. The resolution is corrected for nonlinear effects. The reconstructed jet energy is considered at the electromagnetic scale (in magenta), after hadronic weights are applied (in blue), after hadronic weight and out of cluster corrections are applied (in green) and after hadronic weight, out of cluster corrections and dead material corrections are applied (in red).

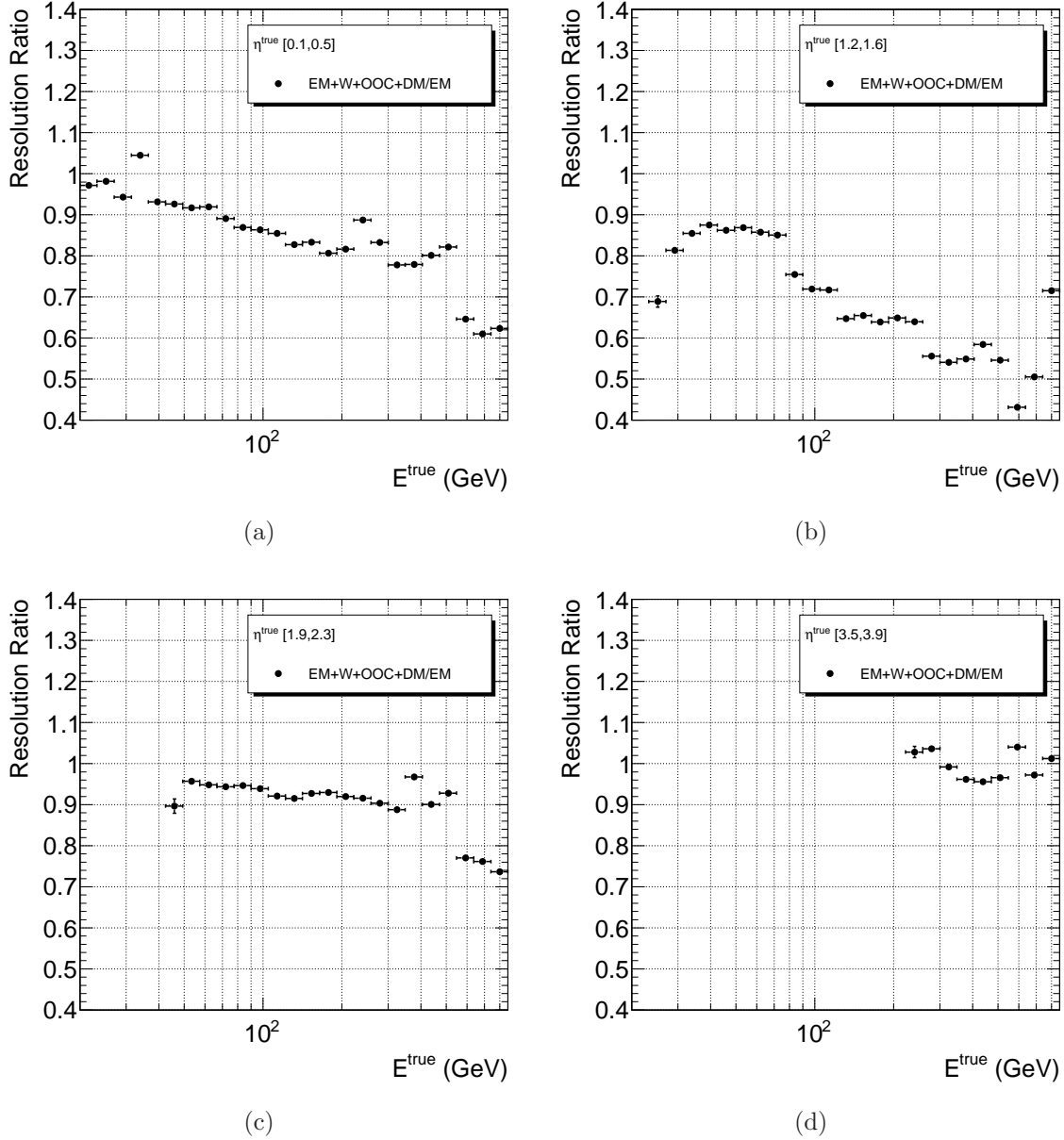


Figure 4.5: Ratio of the resolution after all the cluster corrections are applied to the resolution at the electromagnetic scale for the barrel (a), crack (b), end-cap (c) and forward (d) regions. The resolution is corrected for nonlinear effects.

the RMS to evaluate the resolution. In fact, the RMS is more sensitive to fluctuations than other estimators like the spread of a Gaussian fit. In general, it is possible to notice that the improvement in resolution with respect to the electromagnetic scale increases with energy. This is because for higher energies the correlation between the lost energy and the deposited energy is more pronounced and therefore easier to use for calibrating. The cluster level corrections improve the jet energy resolution in the barrel and in the end-caps, while for the forward region the performance is not as satisfactory. For the crack region the improvement is very large, especially thanks to the dead material corrections. As a benchmark figure, for a jet of 100 GeV in the barrel, the cluster corrections improve the resolution by about 12% with respect to the electromagnetic scale.

Systematics

The jet energy scale systematic error is a very important aspect of jet calibration. A way to assess this error is by comparing the change in linearity due to a specific effect with respect to the linearity obtained with a default sample. Two possible sources of systematic error are considered in this Section, the variation due to a change in the hadronic shower model and the variation due to a change in detector geometry used in the Monte Carlo simulations. The default sample is the one used in the previous Section for the performance studies.

The sample used to assess the systematic error due to the shower model variation is simulated using the FTFP-BERT shower model from the GEANT4 toolkit. In this case the Quark Gluon String fragmentation model used for the QGSP-BERT shower simulation is substituted with the Fritiof model [92]. The sample is then reconstructed using exactly the same set-up as for the default sample. This implies that Local Hadron Calibration corrections derived on a QGSP-BERT simulated sample are applied to a FTFP-BERT simulated sample. In Figure 4.6 linearity histograms obtained with the default sample (plotted as lines) are compared with linearity histograms obtained with the variation sample (plotted as dots). The FTFP-BERT sample shows a higher response than the QGSP-BERT sample already at the electromagnetic scale. This effect propagates also to the calibrated cluster level. In order to appreciate the difference between the two cases, in Figure 4.7 the ratio between the linearity of the reference sample and the linearity of the variation sample is shown both at the electromagnetic scale (in black) and after all cluster corrections are applied (in red). It is possible

to appreciate that the cluster corrections reduce the jet energy scale systematics with respect to the electromagnetic scale, especially in the barrel and the crack regions. This result is achieved thanks to the usage of cluster shape variables on an event by event basis during the cluster calibration. In general, the maximum variation of the jet energy scale after cluster level calibration is about 3.5% for all η region. It is interesting to notice that the linearity in the crack region is less affected by the shower model variation: in fact, as shown in the previous Section, the performance in this region is dominated by dead material effects.

The sample used to assess the systematic error due to the variation of the dead material distribution is simulated with a different detector geometry than the standard description used for the default sample. The distorted detector geometry has been simulated as follows [93]:

- an extra $0.05 X_0$ of material has been placed radially between the barrel pre-sampler and the calorimeter itself ($|\eta| < 1.45$);
- an extra $0.8\text{-}0.11 X_0$ of dead material has been placed radially in the cryostat before the electromagnetic calorimeter ($|\eta| < 1.5$);
- an extra $0.7\text{-}0.11 X_0$ has been placed radially in the cryostat between the barrel of the electromagnetic calorimeter and the hadronic calorimeter;
- the density of the material of the barrel end-cap cryostat gap (covering the space between electromagnetic barrel and electromagnetic/hadronic end-cap for $1 > |\eta| > 1.4$ and in front of the electromagnetic end-cap up to $|\eta| < 1.8$) has been increased by a factor 1.7.

In the forward region, a proper assessment of the detector material in front of the calorimeters is difficult. In order to evaluate the uncertainty in this region, studies on the dead material distribution with data are necessary. The variation sample is reconstructed using exactly the same set-up as for the default sample. In Figure 4.8 linearity histograms obtained with the default sample (plotted as lines) are compared with linearity histograms obtained with the variation sample (plotted as dots). With more dead material the response at the electromagnetic scale lowers, in particular for low energy jets. Dead material corrections are of course affected as well, because the calibration weights are calculated with respect to a different detector description. In Figure 4.9 the ratio between the linearity of the reference sample and the linearity

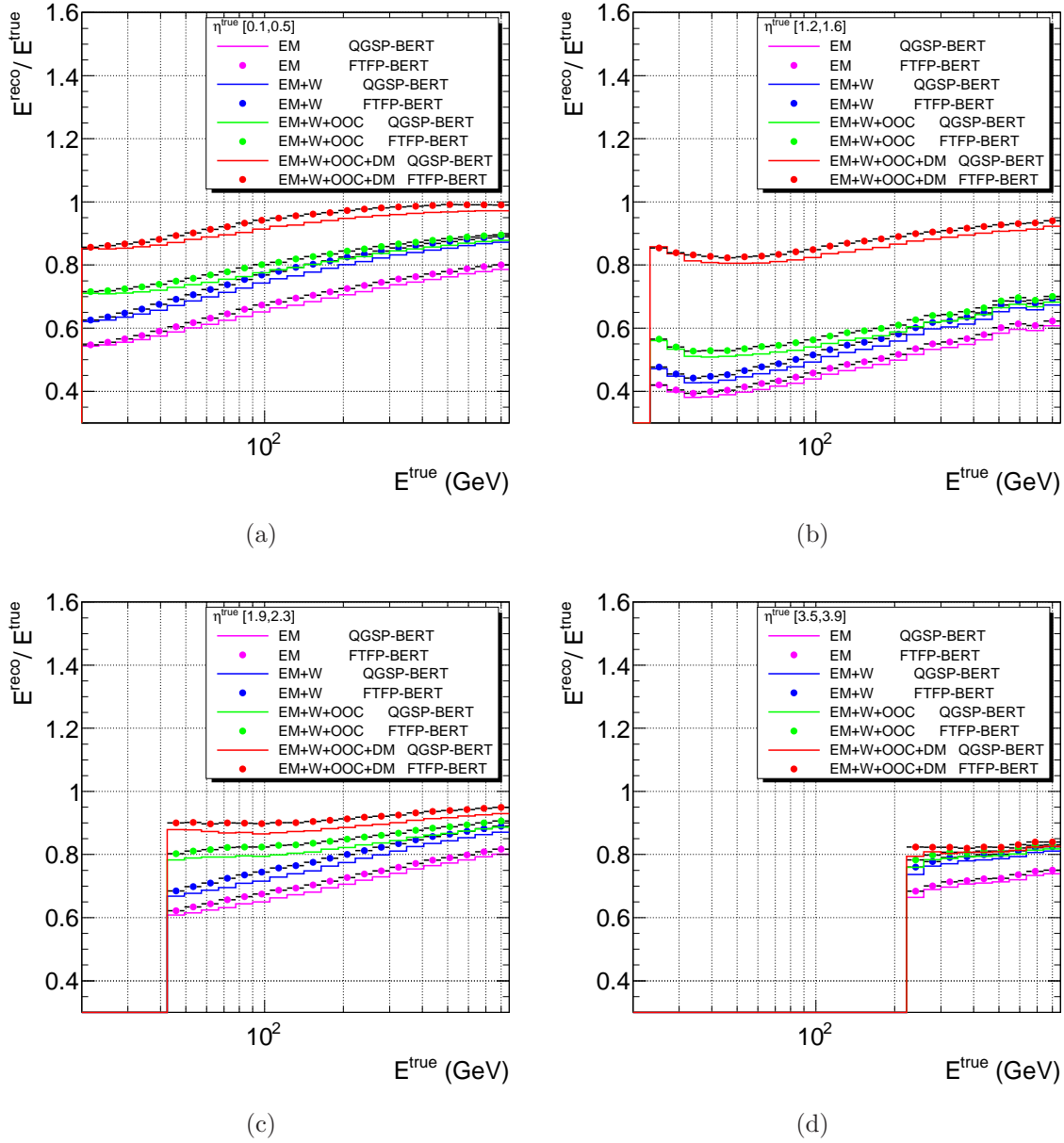


Figure 4.6: Energy linearity for the barrel (a), crack (b), end-cap (c) and forward (d) regions. The reconstructed jet energy is considered at the electromagnetic scale (in magenta), after hadronic weights are applied (in blue), after hadronic weight and out of cluster corrections are applied (in green) and after hadronic weight, out of cluster corrections and dead material corrections are applied (in red). Histograms obtained using the reference QGSP-BERT sample (lines) are compared to histograms obtained using the FTFP-BERT sample (in dots).

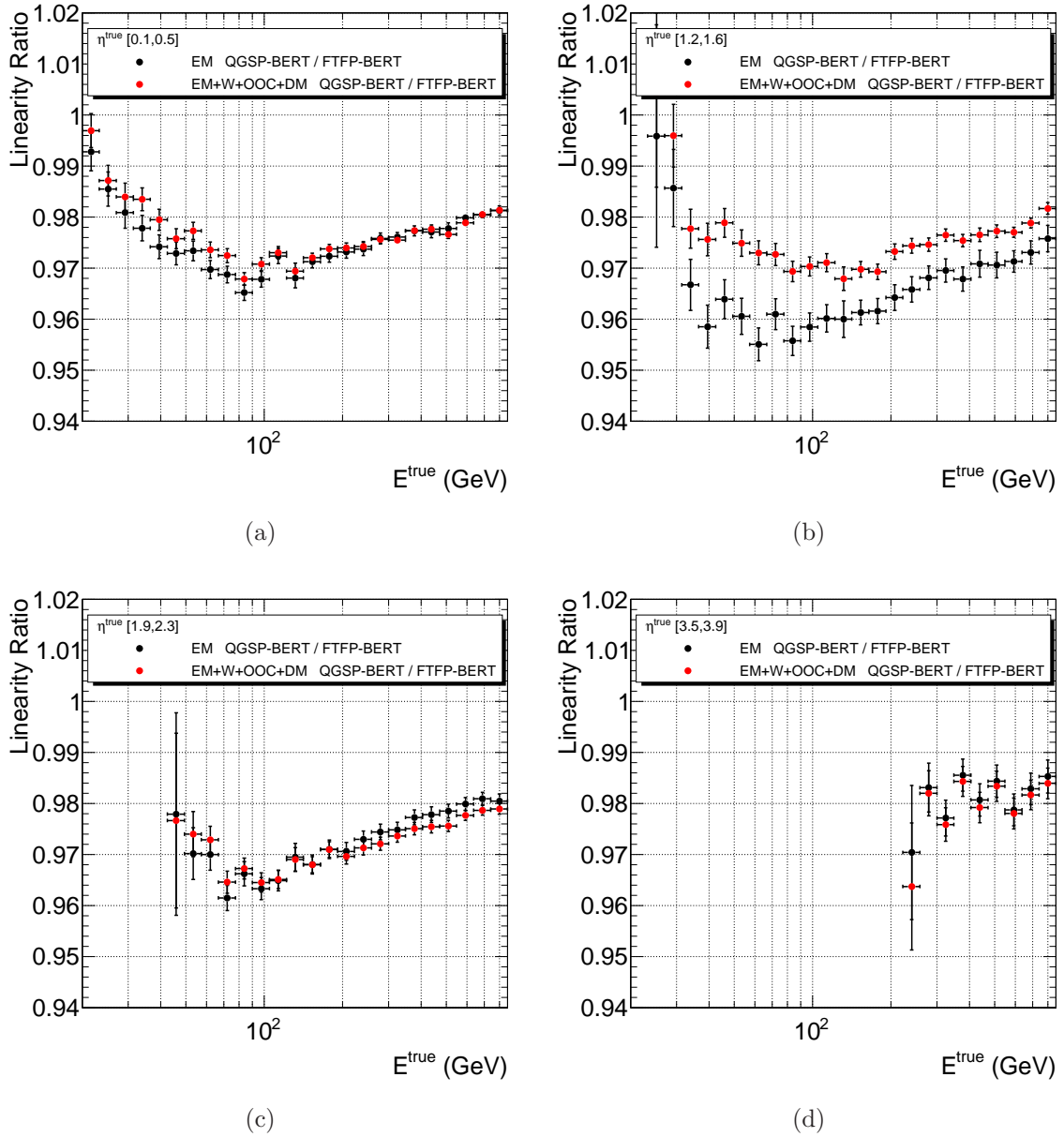


Figure 4.7: Ratio of the linearity obtained with the reference sample (QGSP-BERT) to the linearity obtained with the variation sample (FTFP-BERT), after all the cluster corrections are applied (in red) and at the electromagnetic scale (in black). The ratio is shown for the barrel (a), crack (b), end-cap (c) and forward (d) regions.

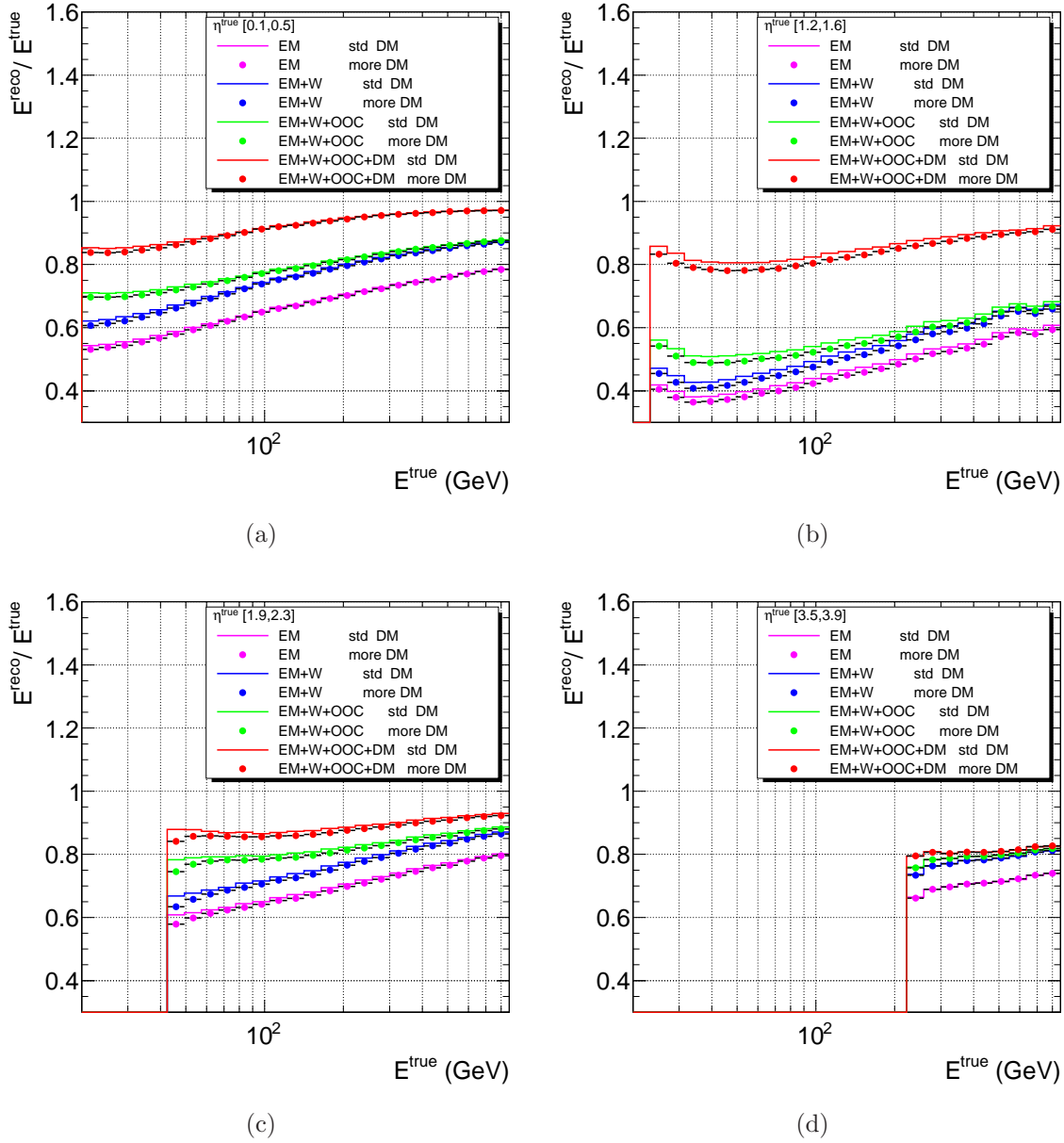


Figure 4.8: Energy linearity for the barrel (a), crack (b), end-cap (c) and forward (d) regions. The reconstructed jet energy is considered at the electromagnetic scale (in magenta), after hadronic weights are applied (in blue), after hadronic weight and out of cluster corrections are applied (in green) and after hadronic weight, out of cluster corrections and dead material corrections are applied (in red). Histograms obtained using the reference sample simulated with standard detector geometry (lines) are compared to histograms obtained using the variation sample simulated adding dead material to the standard detector geometry (in dots).

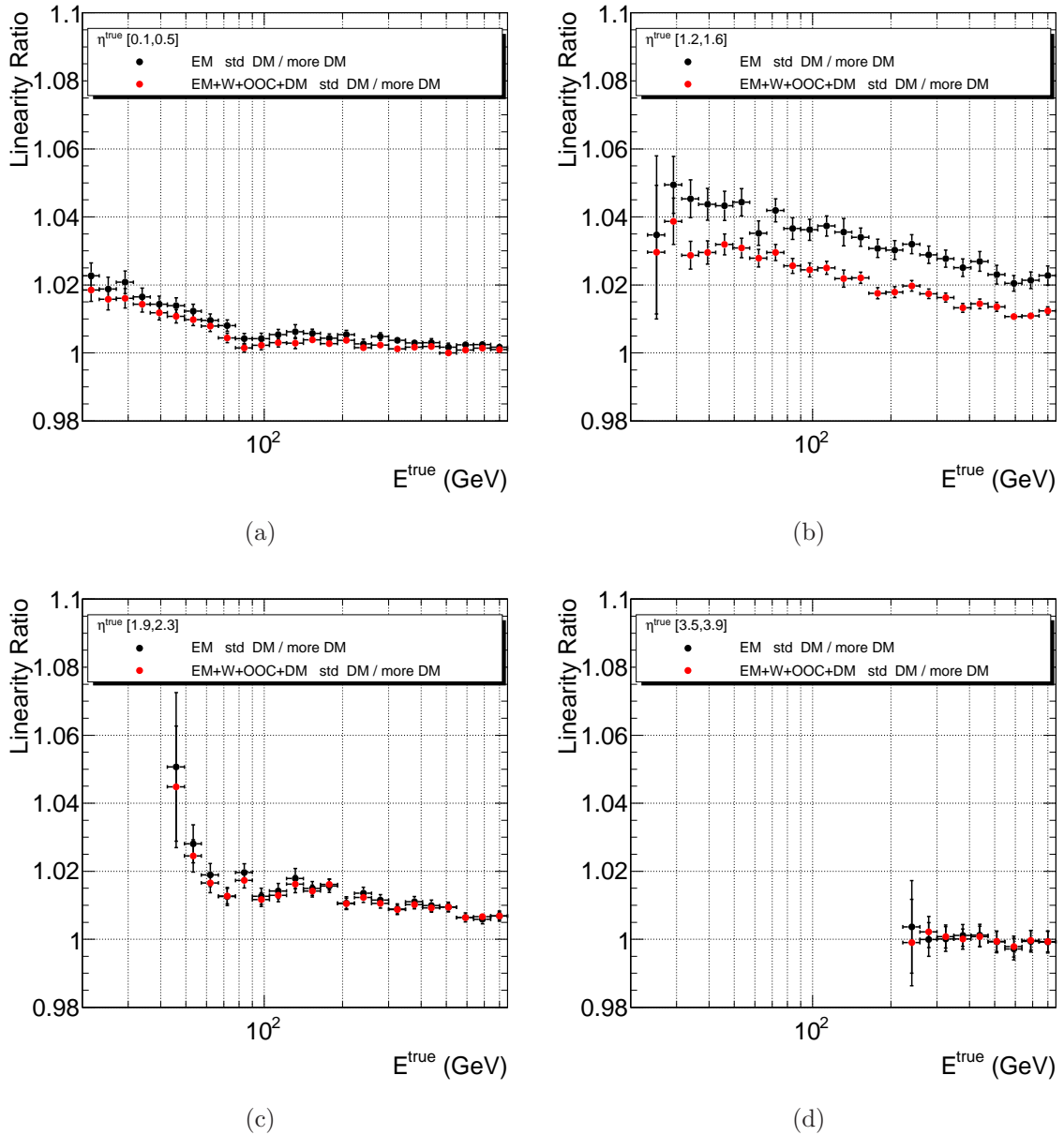


Figure 4.9: Ratio of the linearity obtained with the reference sample (standard geometry) to the linearity obtained with the variation sample (geometry with more dead material), after all the cluster corrections are applied (in red) and at the electromagnetic scale (in black). The ratio is shown for the barrel (a), crack (b), end-cap (c) and forward (d) regions.

of the variation sample is shown both at the electromagnetic scale (in black) and after all cluster corrections are applied (in red). As in the previous study with the hadronic shower model, it is possible to appreciate that the cluster corrections reduce the jet energy scale systematics with respect to the electromagnetic scale, especially in the barrel and the crack regions. This result is achieved thanks to the usage of cluster shape variables on an event by event basis during the cluster calibration. The maximum variation of the jet energy scale at the calibrated cluster level, due to the variation of the dead material distribution, is about 2% in the barrel and end-cap regions. The effect is larger for the crack region where it's about 3%. Jets in the forward region are not very affected because no change has been introduced in the dead material description in this region.

The uncertainties in the Monte Carlo simulation due to the hadronic shower model and to the dead material description are the main source of jet energy scale systematic error. Jets calibrated at the cluster level with Local Hadron Calibration show a good level of stability against both variations. It is possible to combine the uncertainties coming from the two effects in quadrature, because they can be considered statistically independent. In order to give a very conservative estimation of the combined systematic error, the maximum variation over the whole spectrum of energies and η regions can be considered, leading to a 4% combined result. In order to achieve a final systematic uncertainty for the Local Hadron Calibrated jets, jet level corrections have to be tested as well and effects like variation of the fragmentation model or of the cluster noise threshold cannot be neglected. These effects are being studied at the time of writing in order to provide an estimation of the systematic error for the 2011 data.

In order to reduce the systematic error on the jet energy scale, the key factor for Local Hadron Calibration is Monte Carlo tuning. This process requires a detailed comparison of data and Monte Carlo simulations, in order to adjust the description of all relevant parameters as the response at the electromagnetic scale or the dead material distribution or the calorimeter noise model. Studies in this direction have been possible since the very beginning of data taking and are described in Section 4.4.

4.2.2 Performance studies with calibration hits

The Local Hadron Calibration approach aims at correcting for the various detector inefficiencies with a modular approach. In order to study the performance of each correction the comparison with the true particle jet is not sufficient. In fact, from the

studies shown in Section 4.2.1, it is not possible to say how well the hadronic weights correct for the calorimeter non-compensation or the out of cluster corrections for the cluster algorithm inefficiencies or the dead material corrections for the energy lost in dead material. From the moment that all the detector effects are corrected at a cluster level, the answer can be obtained by comparing the energy of the reconstructed cluster with the energy of the true cluster, defined for each of the cluster energy scales.

This definition is possible using calibration hits. As described in Section 3.4.2, a calibration hit represents the true Monte Carlo equivalent of a calorimeter cell. In fact, during the GEANT4 simulation, it is possible to store the information of the energy deposited in a calorimeter cell, for the active and inactive calorimeter material. The same is done for the dead material regions divided into pseudo-cells. In terms of calibration hits, for each reconstructed cluster, the true cluster energy can be defined:

- at the hadronic scale (T_W) as the sum of the energy of the calibration hits inside the cluster ;
- at the out of cluster scale (T_{OOC}) as the sum of the energy of the calibration hits near to the cluster, not included into any other cluster and deposited inside the active calorimeter regions;
- at the dead material scale (T_{DM}) as the sum of the energy of calibration hits near to the cluster, deposited in dead material regions ;

The assignment of calibration hits to the out of cluster and dead material scale is performed via an algorithm that takes into account the proximity of the calibration hit to the cluster in $\eta - \phi$ space and the energy of the cluster.

The quantities to be compared with the T_x terms can be calculated from the energy of the reconstructed cluster after calibration. As described in the previous Section, the three cluster corrections are applied on top of each other, first hadronic weights, then out of cluster corrections and finally dead material corrections. Therefore, the amount of reconstructed energy coming from correction X , R_X , can be calculated as:

- at the hadronic scale (R_W) as the cluster energy after hadronic weights E^W ;
- at the out of cluster scale (R_{OOC}) as the difference between the energy of the cluster after out of cluster corrections and the energy of the cluster after hadronic weights $E^{OOC} - E^W$;

- at the dead material scale (R_{DM}) as the difference between the energy of the cluster after dead material corrections and the energy of the cluster after out of cluster corrections $E^{DM} - E^{OOC}$;

Then, for jets, the T_X and R_X terms are calculated as the sum of the T_X and R_X terms of their cluster constituents. It is important to notice that the definitions of R_W and T_W terms contain both the energy measured by the calorimeter and the energy added because of non-compensation effects. The reason for this relies in the lack of correspondence between the energy at the electromagnetic scale in the calibration hit and in the reconstruction. The reconstructed energy at the electromagnetic scale contains small corrections for dead material losses optimised for electrons and photons, which are not included in the calibration hits. From the moment that the local hadron calibration takes these factors into account, the correct quantities to compare are the inclusive (electromagnetic scale plus hadronic weight) definitions of T_X and R_X .

The linearity L of the cluster corrections can be studied in terms of the quantities:

$$L_W = \frac{R_W}{T_W} \quad L_{OOC} = \frac{R_{OOC} + T_W}{T_{OOC} + T_W} \quad L_{DM} = \frac{R_{DM} + T_{OOC} + T_W}{T_{DM} + T_{OOC} + T_W} \quad . \quad (4.5)$$

In case of perfect calibration ($R_X = T_X$), the linearity terms in Equation 4.5 should be equal to unity. Deviation from this value are dependent on the reconstructed energy contribution R_X under investigation.

In order to study the performance of the L_X terms, a dedicated set of QCD $2 \rightarrow 2$ Monte Carlo simulations containing calibration hit information is used. These samples are generated, simulated and reconstructed using the same physics list (QGSP-BERT) and Local Hadron Calibration correction weights as the reference sample used for the particle jet performance studies.

In Figure 4.10 the mean of the distribution of the linearity quantities defined in Equation 4.5 is shown versus the true particle jet energy for the barrel, crack, end-cap and forward regions. The histogram for L_W is shown in blue, the histogram for L_{OOC} is shown in green and the histogram for L_{DM} is shown in red. The hadronic weights perform very well (inside 2%) in all pseudorapidity regions. The performance for the out of cluster and dead material region changes with energy and it is respectively inside 5% and 10%.

In Figure 4.11 the mean of the distribution of the linearity quantities defined in Equation 4.5 is shown versus the true jet η^{true} for four different E_T^{true} regions. The histogram for L_W is shown in blue, the histogram for L_{OOC} is shown in green and

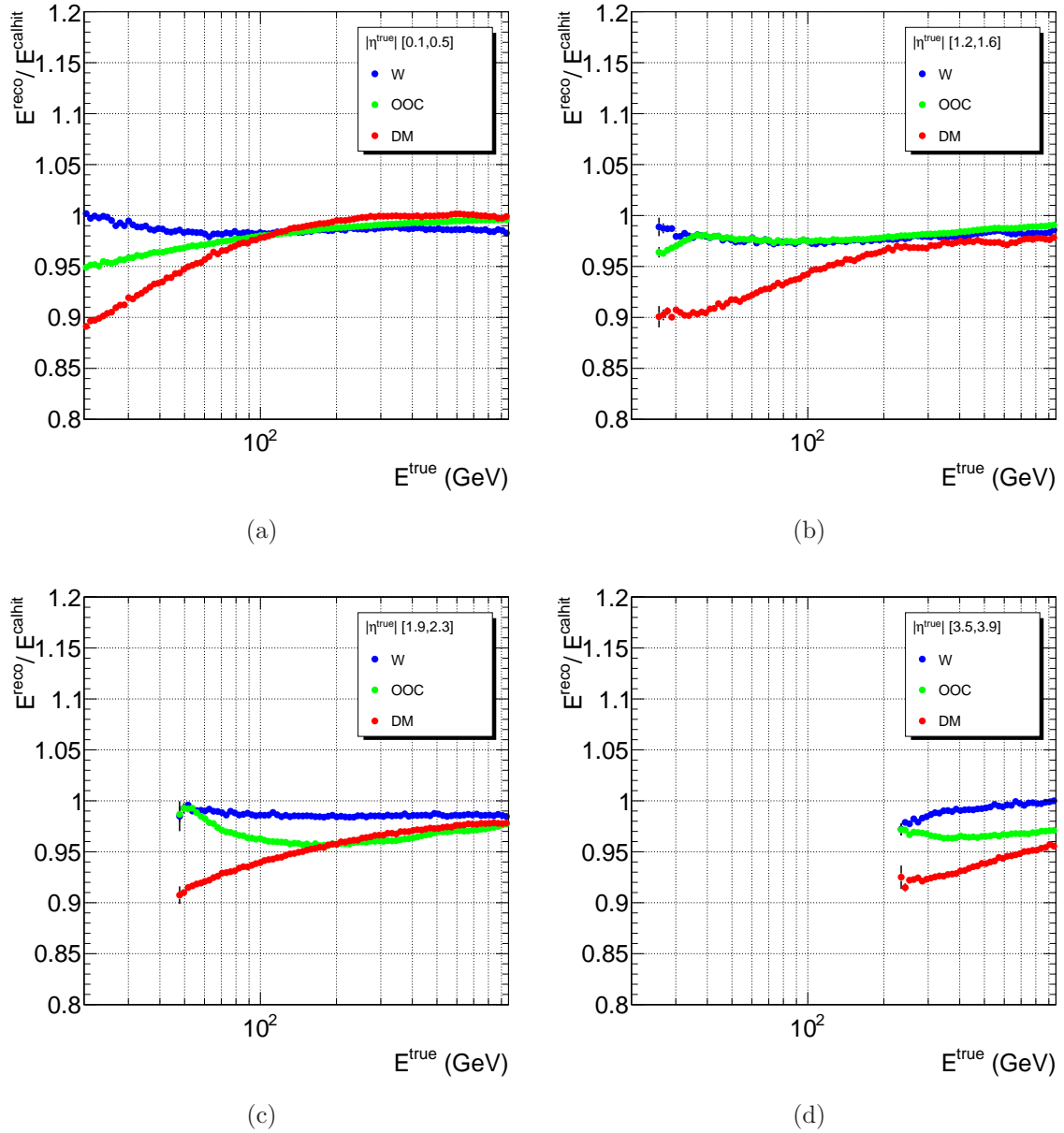


Figure 4.10: Energy linearity with respect to the calibration hit true energy as defined in Equation 4.5 versus the true jet particle energy. L_W for the hadronic weights is shown in blue, L_{OOC} for the out of cluster corrections is shown in green and L_{DM} for the dead material corrections is shown in red. The linearity is shown for the barrel (a), crack (b), end-cap (c) and forward (d) regions.

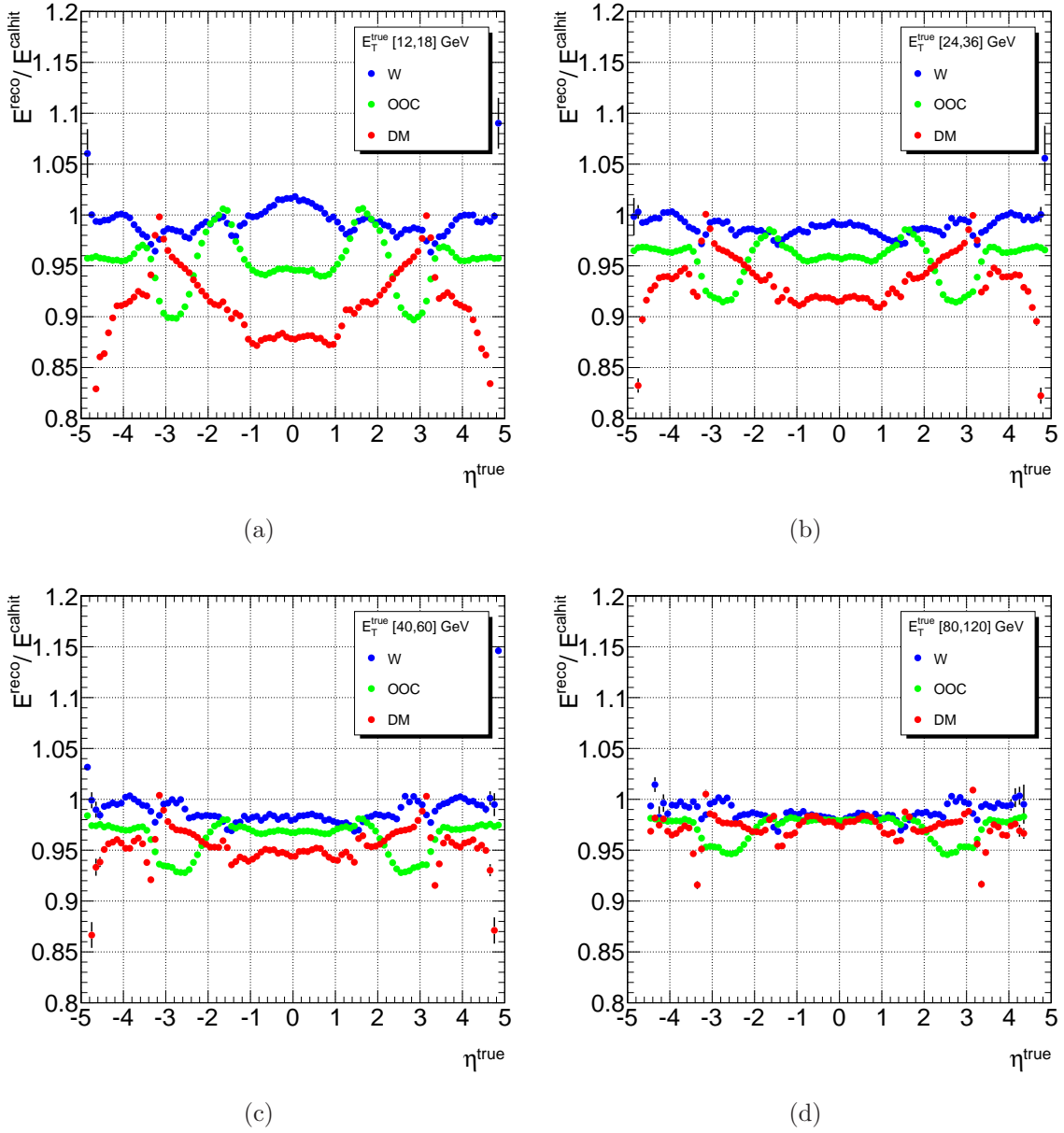
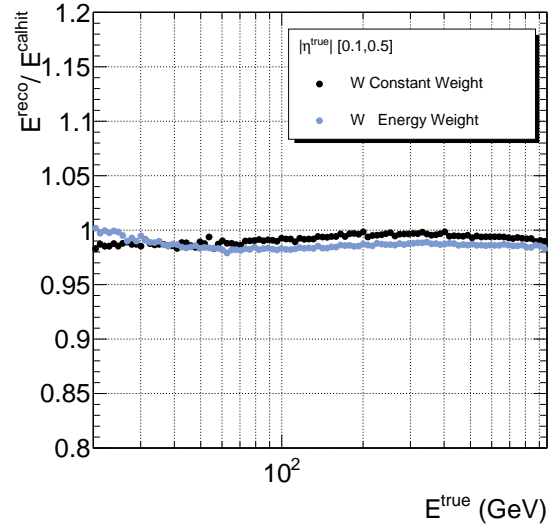
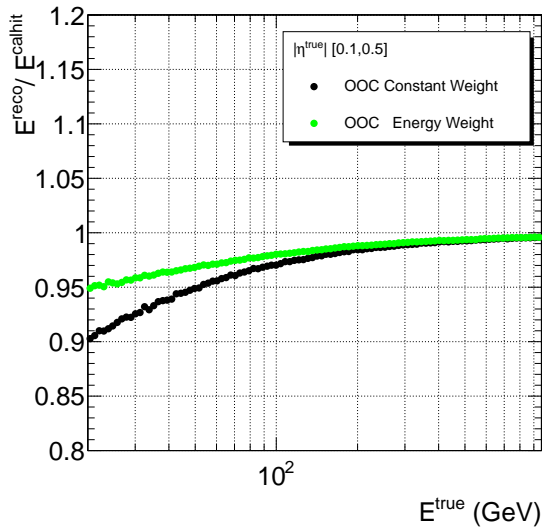


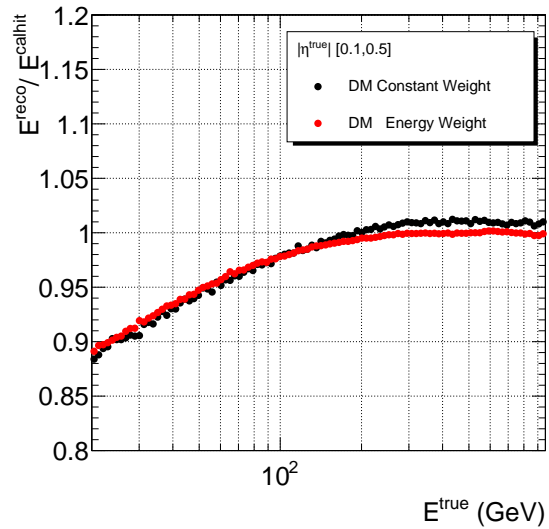
Figure 4.11: Energy linearity with respect to the calibration hit true energy as defined in Equation 4.5 versus the true jet pseudorapidity. L_W for the hadronic weights is shown in blue, L_{OOC} for the out of cluster corrections is shown in green and L_{DM} for the dead material corrections is shown in red. The linearity is shown for the transverse energy ranges $E_T = 15 \text{ GeV} \pm 20\%$ (a), $E_T = 30 \text{ GeV} \pm 20\%$ (b), $E_T = 50 \text{ GeV} \pm 20\%$ (c) and $E_T = 100 \text{ GeV} \pm 20\%$ (d).



(a)

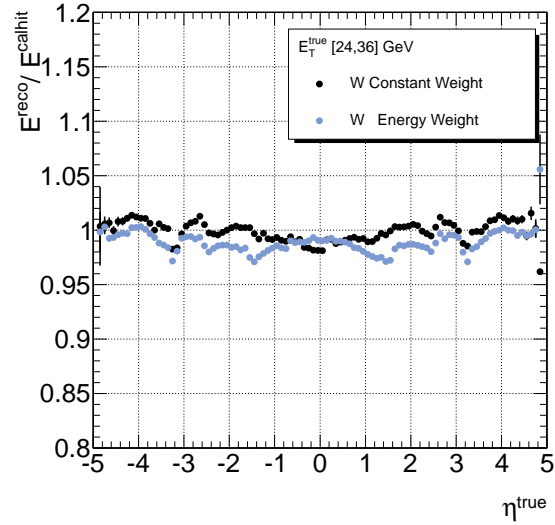


(b)

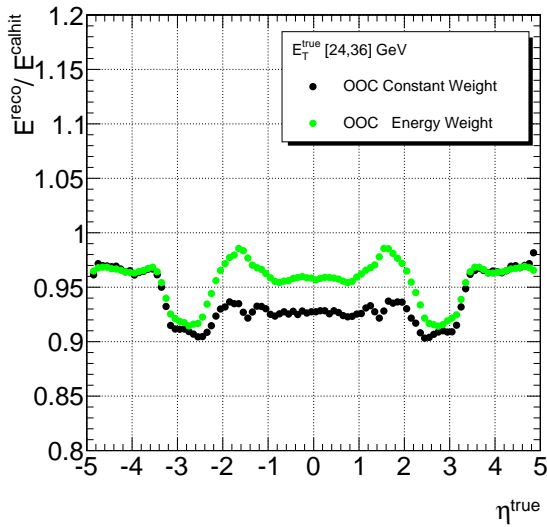


(c)

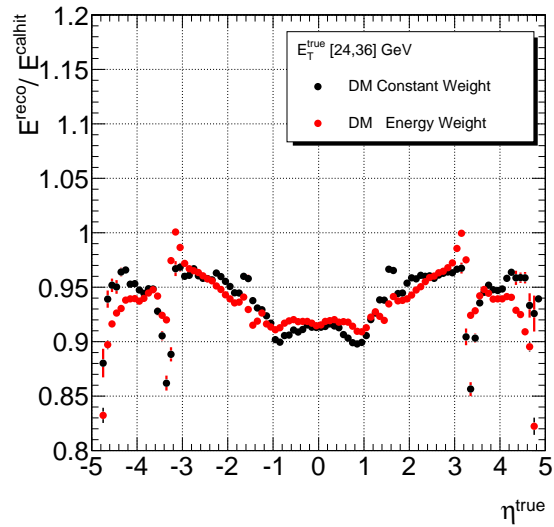
Figure 4.12: Energy linearity with respect to the calibration hit true energy as defined in Equation 4.5 versus the true particle jet energy. The linearity is shown for the barrel region for the constant weight schema (in black) and for the event probability schema (in colour): L_W for the hadronic weights is shown in grey (a), L_{OOC} for the out of cluster corrections is shown in green (b) and L_{DM} for the dead material corrections is shown in red (d).



(a)



(b)



(c)

Figure 4.13: Energy linearity with respect to the calibration hit true energy as defined in Equation 4.5 versus the true pseudorapidity. The linearity is shown for the barrel region for the constant weight schema (in black) and for the energy weight schema (in colour): L_W for the hadronic weights is shown in grey (a), L_{OOC} for the out of cluster corrections is shown in green (b) and L_{DM} for the dead material corrections is shown in red (d).

the histogram for L_{DM} is shown in red. In this case as well the hadronic weights perform the best, achieving a linearity of 2% in the whole η spectrum and for all E_T regions. The out of cluster and dead material corrections show a linearity which strongly depends on η and on the E_T^{true} regime. For both cases the linearity improves for more energetic jets, which deposit most of their energy in calorimeter clusters and thus are easier to calibrate. The pattern of the out of cluster correction linearity with respect to η is determined by the calorimeter cell geometry. The pattern of the dead material correction linearity with respect to η is determined by the distribution of dead material in the ATLAS detector.

Anyhow, in general, it is not possible to draw final numbers out of these performance studies. In fact, the definition of the true out of cluster and dead material energy can be ambiguous. The algorithm is only based on the proximity of the calibration hits to the cluster. This argument is sufficient in the case of single pion simulations, where all hits belong to the same particle and can be assigned to the clusters in the event. In the case of a jet event, a cluster can be surrounded by hits belonging to a particle which is not part of the same jet or by a particle which has deposited no energy in the cluster itself. In order to remove these ambiguities, a new definition of the true cluster energy based on the particle ID tool is under study. The particle ID tool, as described in Chapter 3, stores the information of which particles have contributed to the energy released in a calibration hit. In this way it is possible to uniquely assign to a cluster the energy lost as out of cluster and dead material by the particles which mostly contribute to its energy content.

Nevertheless, the calibration hit studies have shown a strong diagnostic power for internal tests during the development of the Local Hadron Calibration. When a new set of correction weights is released, in order to understand which correction is more affected by the changes introduced and in which respect, the calibration hit comparison is the only way. In fact, in these performance studies the energy recovered by each correction is studied separately and with respect to the same true reference. New sets of constants can be released either because some important aspect of the detector simulation has changed or because a new approach to the calculation of the correction weights is put in place.

For example, in an older version of the Local Hadron Calibration schema, every cluster was entering the cluster correction calculation with weight equal to one (constant weight). This approach would be completely correct if one particle would always correspond to one cluster. In the recent implementation, every cluster enters the cluster

correction calculation with a weight that is proportional to its calibration hit energy content (energy weight). This second approach ensures that the probability is correctly normalised as well in the case that one particle creates more than one cluster. In Figure 4.12 the L_W , L_{OOC} and L_{DM} histograms versus E^{true} are shown for the barrel region, both for the constant weight corrections (plotted in black) and for the energy weight corrections (plotted in colours). In Figure 4.13 the same quantities are shown as a function of η^{true} for the $E_T^{true} = 30$ GeV bin. From these studies it is possible to see that the energy weight approach degrades the linearity of the hadronic weight corrections, especially at higher energies. The corrections which are more affected by the difference between the two approaches are the out of cluster corrections, for which the linearity obtained with the energy weight approach improves by up to 5% for low energies. In the case of the dead material corrections, the small overshoot at large energies for the linearity with the constant weight approach is corrected in the case of energy weight approach. In the current version of the Local Hadron Calibration the energy weight approach is the one being used, because it is preferable in terms of probability normalisation and because it shows good linearity performance. Nevertheless a mixed approach is under study in order to restore the hadronic weight linearity.

Without the calibration hit studies it would be difficult to understand that the final improvement in linearity for low energies in the barrel with the event probability approach is due to the out of cluster corrections or that the degradation in linearity at high energies is due to the hadronic weights.

In conclusion, calibration hit performance studies are a precious tool for a modular calibration approach, like the Local Hadron Calibration. In fact, they are the only way to assess the performance of a specific correction in compensating for the inefficiency for which it has been designed. The power of these studies is limited at the moment by the definition of the true cluster energy, but it will be soon possible to overcome this limit with the use of the particle ID tool.

4.3 Monte Carlo performance studies for MET

The measurement of the missing transverse energy (MET) is based on the law of momentum conservation applied to the transverse plane. The momentum conservation along the z axis is not considered because of the difficulty to measure the z component of all the objects emerging from a hadron collision event, including beam remnants. The initial momentum in the transverse plane is zero, so the sum of transverse momentum

of all the particles produced in the event is zero as well. The opposite vector to this sum is called missing transverse energy, because it is mainly calculated from fundamental calorimeter objects, like cells, for which the mass is zero.

If the missing transverse energy is different from zero, some particles that don't interact with the detector must have been produced and the opposite of the MET vector is the sum of their transverse momenta. Therefore a correct measurement of MET is essential for many physics studies in ATLAS. Events with large MET are expected to be the key signature for new physics such as supersymmetry and extra dimensions.

ATLAS has a sophisticated programme for MET reconstruction and calibration. The default MET variable used for most of the Monte Carlo ATLAS studies is called METRefFinal and makes use of the Global cell energy-density calibration (GC) [76]. Instead, in this Section, a simple approach to MET calibration based on the use of the Local Hadron Calibration is discussed and preliminary results on the performance are presented. For the 2011 data the ATLAS default MET calculation is based on Local Hadron Calibration and consists of a development of the method presented here.

The MET vector consists of two components, $E_{Tmiss,x}$ and $E_{Tmiss,y}$. What is usually called MET is the norm of this vector. Two main contributions to the calculation of MET are considered here, the calorimeter term and the muon term:

$$\mathbf{E}_{Tmiss} = \mathbf{E}_{Tmiss}^{calo} + \mathbf{E}_{Tmiss}^{muon} , \quad (4.6)$$

where the sum is intended as a vector sum. The calorimeter term can be calculated with the use of Local Hadron Calibration from the calorimeter clusters after all the cluster corrections are applied. The way Local Hadron Calibration is conceived suits the MET calculation very well. In fact, all energy deposits included into clusters are calibrated, independently of the fact that they are included into jets. No additional corrections for dead material losses are necessary and the MET calculation can be performed directly from the cluster transverse energy, without considering the calorimeter cells:

$$E_{Tmiss,x,y}^{calo} = - \sum_{i=0}^{Nclus} E_{x,y}^{clus} , \quad (4.7)$$

where $E_{x,y}^{clus}$ indicates the x and y term of the cluster transverse energy. Clusters for $|\eta| < 4.5$ are considered. The MET muon term is calculated from the momenta of

muons measured in a range of pseudorapidity $|\eta| < 2.7$:

$$E_{T_{miss,x,y}}^{muon} = - \sum_{i=0}^{N_{muon}} E_{x,y}^{muon} . \quad (4.8)$$

In the region $|\eta| < 2.5$ only good quality muons in the muon spectrometer with a matched track in the inner detector are considered. The matching requirement considerably reduces contributions from fake muons. The calorimeter term and muon term can be added directly as first approximation. In fact, muons release a very small amount of energy in the calorimeter with respect to their momentum, so the double counting of this energy can be neglected.

In order to study the performance for MET reconstruction it is necessary to define a MET true reference. This is obtained from Monte Carlo simulation by summing the transverse energy of all the non-interacting particles in the event. This true MET is the final object that has to be reconstructed for physics analysis. The comparison between the reconstructed MET and the true MET is studied with respect to the linearity defined as:

$$\frac{\text{MET}^{\text{true}} - \text{MET}^{\text{reco}}}{\text{MET}^{\text{true}}} , \quad (4.9)$$

with a cut on $\text{MET}^{\text{true}} > 20$ GeV. This is justified because the reconstruction of a small amount of MET is particularly complicated. In fact, MET reconstruction can be strongly affected by detector noise or by any inefficiency in the reconstruction of all the objects that are considered for the calculation.

In order to study the performance for MET reconstruction, di-jet events cannot be used because no significant MET is expected. Instead a sample of $t\bar{t}$ events with dileptonic and semi-leptonic decay is used. In these processes the neutrinos from the W decays can have very large transverse momenta. This sample is the same used for the $t\bar{t}$ all-hadronic analysis discussed in Chapter 5 where all the details on the simulation are given.

In Figure 4.14 the MET linearity is shown versus true MET. The linearity of the METRefFinal is shown in black, the linearity of the MET calculated from Local Hadron Calibration as described above is shown in red and the linearity of MET from Local Hadron Calibration with constituent based jet level corrections is shown in blue. In general all the three curves are flat for true MET > 50 GeV. For smaller values of the true MET the performance drops because of fake reconstructed MET due to detector noise and containment. The best performance is given by the METRefFinal calculation,

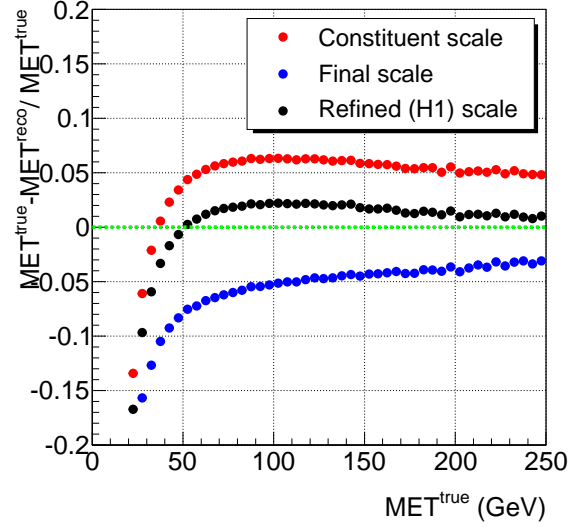


Figure 4.14: MET linearity versus true MET. The linearity for the METRefFinal calculation is shown in black, the linearity for the MET calculation with Local Hadron Calibration cluster level corrections is shown in red and the linearity for the MET calculation with Local Hadron Calibration jet level and cluster level corrections is shown in blue. Monte Carlo simulations of $t\bar{t}$ semi-leptonic events are used.

which includes proper calibration for e , γ and τ objects, additional calibration for b -jets and considers of the muon energy released in the calorimeter. The performance of the MET with Local Hadron Calibration at the cluster level is better than 8% for true MET > 50 GeV, which is a comparable result to the jet performance linearity after cluster corrections with respect to the true jet, as discussed in Section 4.2.1. In order to improve the linearity of the MET calculated with Local Hadron Calibration all the effects considered for the METRefFinal calculation should be included. Most of them have been already accounted for in the MET calculation for data. The effect of the final jet corrections should be included as well. A very direct way to account for jet level corrections is to calculate the amount of transverse energy added by them to the jet calibrated only with the cluster corrections:

$$E_{T,x,y}^{CB} = \sum^{N_{jets}} E_{T,x,y}^{CB+DM+OOC+W} - E_{T,x,y}^{DM+OOC+W}, \quad (4.10)$$

where $E_{T,x,y}^{CB+DM+OOC+W}$ is the jet energy component after cluster corrections and jet level corrections are applied, $E_{T,x,y}^{DM+OOC+W}$ is the jet energy component after cluster corrections are applied. The sum is intended over all jets in the event. Then $E_{T_{miss},x,y}^{CB} =$

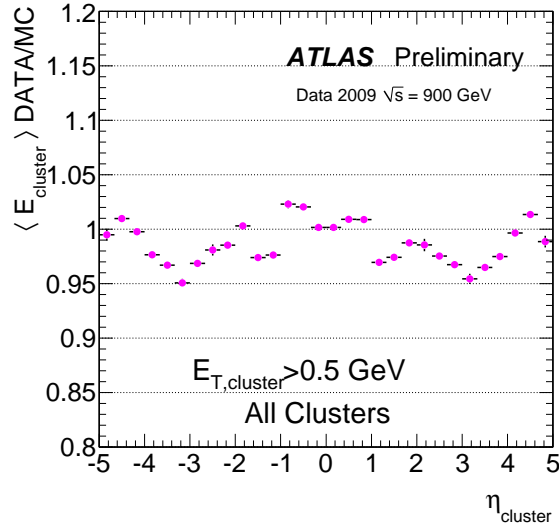


Figure 4.15: Ratio of the mean cluster energy at the electromagnetic scale in data and in Monte Carlo simulations versus η . Only clusters with transverse energy larger than 500 MeV are considered.

$-E_{T,x,y}^{CB}$ can be considered as a third term to be added to Equation 4.6. The linearity of the MET calculated with this approach is shown in blue in Figure 4.14. The linearity is inside 8% for true MET > 50 GeV, but the reconstructed MET is overestimated. This is due to a double counting of the energy recovered by the constituent based jet level corrections. In fact, these corrections recover for jet energy which is not reconstructed inside the jet, but that can be deposited outside the jet inside other calorimeter clusters. This is not an issue for jet calibration performance, because only one jet is considered at the time. Instead MET is like the film negative of hadronic calibration: it is correct if and only if all the deposits in the calorimeter are perfectly calibrated. A method to remove the jet level correction ambiguity for MET calculation is under study. A possible solution could be to exclude from the MET calculation all the clusters outside a jet, but near to its perimeter, because their energy is already accounted for by the jet level corrections.

4.4 Validation on ATLAS data

The first step towards the validation of the Local Hadron Calibration on data is to compare the effect of the cluster corrections in data and Monte Carlo. For this purpose ATLAS data collected in December 2009 for collisions at a centre of mass energy

of $\sqrt{s} = 900$ GeV have been considered. Events are selected using the minimum bias trigger scintillators (MBTS), installed on both sides of the ATLAS detector and covering the pseudo-rapidity region $2.09 < |\eta| < 3.84$. Offline cuts on the MBTS hits and calorimeter timing are used to remove contamination from events produced by the beam halo, by the interaction of beam protons with the gas in the beam pipe or by cosmic muons. Only runs in which the calorimeter and the inner detector were fully operational and the solenoid was on are considered. These criteria select 330810 events.

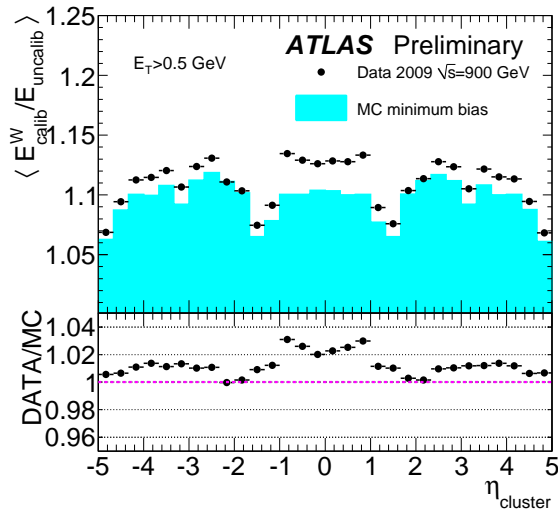
Data are compared to Monte Carlo (MC) simulations of non-diffractive, single and double diffractive processes in proton-proton collisions at a centre of mass energy of $\sqrt{s} = 900$ GeV. Pythia with ATLAS MC09 tune [94] is used as generator, while the detector response is simulated with GEANT4 using the QGSP-BERT hadronic shower model. The same trigger and event selection is used on the Monte Carlo simulations and on data.

As first step the energy of clusters at the electromagnetic scale has been compared between data and Monte Carlo. The ratio between the mean cluster energy in data and in Monte Carlo versus the cluster pseudorapidity is shown in Figure 4.15. Only clusters with transverse energy larger than 500 MeV are considered. The overall agreement is very good: $\approx 2\%$ in the central region and $\approx 5\%$ in the end-cap and forward region. Further studies are on going in order to understand the residual differences.

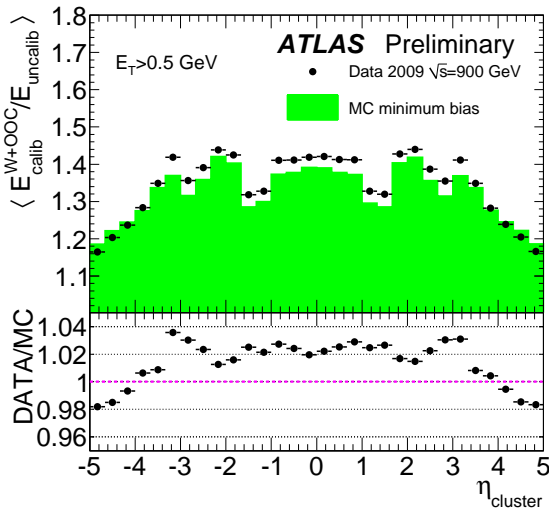
In order to validate the various calibration steps, for all clusters the ratio of the calibrated and the energy at the electromagnetic scale is considered both in data and in Monte Carlo simulations. This procedure reduces the dependency on the absolute energy difference before calibration between data and Monte Carlo. The average of the distribution of this ratio is shown versus the cluster pseudorapidity in Figure 4.16(a) for the hadronic weight corrections. The same study is shown in Figure 4.16(b) for clusters calibrated with hadronic weights and out of cluster corrections. Finally the same study is performed after hadronic weights, out of cluster corrections and dead material corrections are applied to the clusters, as shown in Figure 4.16(c). Only clusters with a transverse energy larger than 500 MeV are considered. Since the selected minimum bias sample is dominated by low energy clusters, the corrections applied for energy lost outside clusters and in dead material are large with respect to the hadronic compensation weights. The double ratio between data and Monte Carlo is shown at the bottom of Figures 4.16(a), 4.16(b) and 4.16(c). The value of the corrections is larger in data than in Monte Carlo simulations by $\approx 2\%$ in the central region of the detector. This difference is likely due to incorrect noise description in the simulation, which

is already under investigation. For the out of cluster and dead material corrections around $|\eta| = 3.1$ the data and the simulation show a difference of $\approx 4\%$. This region corresponds to the transition between the end-cap and the forward calorimeter, where a large amount of dead material due to the forward calorimeter support structure is present. For this reason incorrect dead material description in the simulation is the likely cause of the disagreement, which can be evaluated and corrected with more data available.

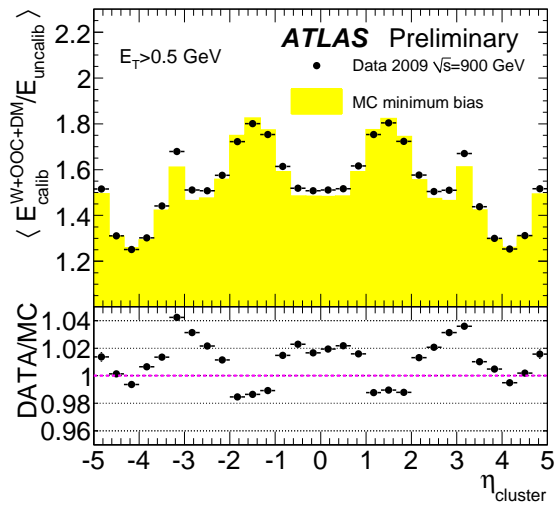
These first results on Local Hadron Calibration applied to ATLAS data show that the Monte Carlo simulations describe the data very well. Further tests in this direction are ongoing in order to validate the jet level corrections using multi-jet events. By performing these studies with an increasing amount of integrated luminosity of data, it will be possible to correct the Monte Carlo simulations in order to obtain the jet energy scale accuracy of 1% desired by the ATLAS physics programme.



(a)



(b)



(c)

Figure 4.16: Mean of the distribution of the ratio of the calibrated cluster energy over the electromagnetic cluster energy in data (points) and Monte Carlo simulations (histogram) versus η . Cluster energy is considered after hadronic weights are applied (a), after hadronic weights and out of cluster corrections are applied (b) and after hadronic weights, out of cluster corrections and dead material corrections are (c). Only clusters with transverse energy larger than 500 MeV are considered. The lower plot shows the ratio of data over Monte Carlo simulations.

Chapter 5

All-Hadronic Top Quark Mass

Top quark physics is of primary importance at the LHC. As discussed in Chapter 1 the top quark is a very interesting object to study and the large statistics expected at the LHC allows for an extended programme of very accurate measurements. Some of these studies are feasible right from the beginning of data taking and first results on the $t\bar{t}$ production cross section at $\sqrt{s} = 7$ TeV of centre of mass energy are already available [95].

In this Chapter the all-hadronic $t\bar{t}$ decay channel is studied. In the all-hadronic mode both top quarks decay into a b quark and a W boson and both W bosons decay into quarks, as shown in Figure 5.1. Therefore the final state is characterised by 6 highly energetic jets, two of which are b -jets, no MET and no high energetic isolated lepton. The all-hadronic channel is the one with the highest branching ratio, but suffers from a huge background contamination coming from QCD multi-jet events. These are $2 \rightarrow n$ processes involving all quarks but top quarks and gluons, which can give rise to a final state very similar to the $t\bar{t}$ all-hadronic final state, especially when two of the produced partons are a $b\bar{b}$ pair. Nevertheless it is possible to distinguish $t\bar{t}$ all-hadronic events from the QCD background by exploiting the intrinsic different nature of the two types of events. Despite of the difficulty of the task, studying the top quark in the all hadronic channel is fundamental in order to provide a complementary measurement of the top quark properties with respect to the measurement performed using semi-leptonic and di-leptonic events. Furthermore, $t\bar{t}$ all-hadronic events are a benchmark for developing methods to control QCD events, which are one of the main source of background for new physics discoveries at the LHC.

In this Chapter a study on the measurement of the top quark mass in the $t\bar{t}$ all-

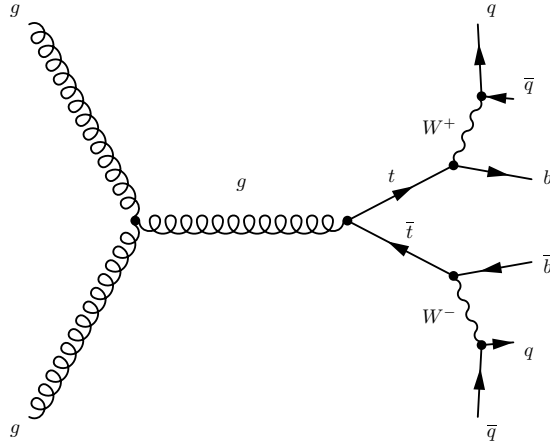


Figure 5.1: All-hadronic $t\bar{t}$ decay channel shown in the case of gluon fusion production mechanism. Both W bosons decay hadronically.

hadronic channel is presented. Monte Carlo simulations at centre of mass energy of $\sqrt{s} = 10$ TeV are used assuming an integrated luminosity of 200 pb^{-1} . Details on the simulations are given in Section 5.1. The analysis requires a refined event selection in order to isolate the signal from the QCD background. The event selection is based on the use of b -tagging information and on cuts performed on a set of variables, which exploit the different topology of $t\bar{t}$ and QCD events. The event selection and the trigger efficiency are discussed in Section 5.2. Top quark candidates are then reconstructed taking care of the complex combinatorics due to the high jet multiplicity, as discussed in Section 5.3. A distribution of the invariant mass of the three jets forming the top quark candidate can be built and is used as an estimator of the top quark pole mass. Because of the very low simulated statistics for the background samples, it is necessary to extract the shape of the background from the distribution obtained with no b -tagging requirement. The procedure adopted for the background shape extraction is described in Section 5.3.3. From the Monte Carlo invariant mass distribution, pseudo-experiments can be built in order to develop a fit procedure to extract the top mass estimator, as described in Section 5.4. Systematic uncertainty on this result are estimated with respect to the uncertainty on the background shape extraction, on the jet energy scale and on the b -tagging efficiency. Finally, in Section 5.6, the fit procedure is tested with respect to the true Monte Carlo top mass with the use of a pull distribution.

Dataset Name	p_T min (GeV)	p_T max (GeV)	σ (pb)
J0	8	17	-
J1	17	35	1.35E+008
J2	35	70	4.07E+007
J3	70	140	3.07E+006
J4	140	280	1.70E+005
J5	280	560	6.30E+004
J6	560	1120	150
J7	1120	2240	1.5
J8	2240	-	0.001
J5+	280	-	6.40E+003

Table 5.1: Definition of Alpgen QCD slices in p_T of the leading jet.

5.1 Monte Carlo samples

The datasets used for developing the top mass analysis presented in this Chapter are simulated for pp collisions at a centre of mass energy of $\sqrt{s} = 10$ TeV, which was the energy foreseen for the LHC start up in September 2008, before the accident due to the faulty magnet interconnect occurred. The Monte Carlo generators used are introduced in Chapter 1. The samples are simulated using the ATLAS software Athena version 14.2.10.1. The analysis is performed using a standalone Athena class and is run on the Grid using Athena version 15.6.9.12.

The processes of interest for the all-hadronic analysis are:

1. $t\bar{t}$ events with all-hadronic decay;
2. $t\bar{t}$ events with NON-all-hadronic decay, including all semi-leptonic and di-leptonic decays;
3. $2 \rightarrow n$ events (QCD +jets), where only light quarks (u, d, s, c , treated as massless) are included at the matrix element level and pairs of $b\bar{b}$ quarks are introduced through the gluon splitting process $g \rightarrow b\bar{b}$ in the parton shower;
4. $2 \rightarrow n$ events (QCD $b\bar{b}$ +jets), where a pair of $b\bar{b}$ quarks is produced at the matrix element level together with light quarks;

All $t\bar{t}$ events (datasets 1. and 2.) are generated with MC@NLO [49] version 3.1 and the CTEQ6M [33] parton distribution function. The parton shower is simulated with

HERWIG and the underlying event with JIMMY [45]. The NLO $t\bar{t}$ cross section is then scaled with a k -factor of 1.07 to the NNLO value $\sigma_{t\bar{t}} = 401.60_{-4.3\%}^{\pm 3.7\%(\text{scales})+4.6\%(\text{PDFs})}$ pb [96]. This cross section is valid for $\sqrt{s} = 10$ TeV and is reduced by 55% with respect to the value for $\sqrt{s} = 14$ TeV. The reference top quark mass value used is $m_t^{MC} = 172.5$ GeV. The GEANT4 [40] package is used to simulate the interaction of the produced particles with the ATLAS detector.

Both QCD +jets and QCD $b\bar{b}$ +jets events (datasets 3. and 4.) are simulated with Alpgen [46], which provide full LO matrix element calculation. Alpgen uses the LO compatible parton distribution function CTEQ6L. The parton shower is simulated with HERWIG, the underlying event with JIMMY and the MLM matching schema is used to interface the parton configurations from the parton shower with the parton configurations from the matrix element. The total Alpgen cross section of QCD +jets and QCD $b\bar{b}$ +jets events together is about 6 billion pb (for $p_T(\text{jet}) > 10$ GeV), thus these datasets cannot be produced inclusively in useful amounts of integrated luminosity. Instead a p_T slicing strategy that is similar to the one used in Chapter 4 for the Pythia QCD di-jet samples is used. In the Alpgen case the p_T of the leading jet is used for the dataset definition, because there are more than two partons at the matrix element level. Details on the sample naming convention, slicing boundaries and cross sections are given in Table 5.1. An integrated luminosity of 10 pb^{-1} is generated for slices J2, J3 and J4. For slices J5 through J8, an integrated luminosity of 300 pb^{-1} is generated and combined into a single super-slice labeled J5+ to simplify physics analysis use. Each Alpgen JX slice is divided into sub-samples (Npy) for which $y=2, 3, 4, 5$ and 6 partons are present in the finale state at the matrix element level. All sub-samples have to be added together to get the complete description of a p_T slice. The Np6 samples are omitted for slices J2 and J3, because their generation time was disproportionate (e.g. 6000 CPU-days for J2Np6). This is an acceptable compromise because the 6-jets topology can emerge with 5 partons at the matrix element through parton showering. The J2 and J3 samples are generated with a filter applied to the true particle jets (obtained from stable particles after hadronisation). This prevents the simulation through GEANT4 of events that are of little impact on the analysis. The filter is based on true particle jets, reconstructed with the Cone algorithm with parameter $R = 0.4$ and requires at least 4 jets with $p_T > 17$ GeV of which at least 3 jets with $p_T > 35$ GeV. It is important to notice that the integrated luminosity of 10 pb^{-1} refers to the samples after filtering. The filter efficiency is of 0.8% (J2) and 13.66% (J3) for the QCD +jets events and of 1.91% (J2) and 22.05% (J3) for the QCD $b\bar{b}$

+jets events. These figures are obtained summing over all the Npy sub-samples. The true filter overlaps well with the event selection described in Section 5.2. No events are generated for the J0 and J1 slices because, by definition, none of them would pass the true jet filter, which is needed for large cross section samples. In fact, the true jet filter asks for the leading jet in the event to have $p_T > 35$ GeV, but, as reported in Table 5.1, such an event belongs at least to the J2 slice.

A systematic uncertainty of $\pm 50\%$ on the background normalisation is included in the final result of the analysis in order to account for various sources of uncertainties in the multi-jet event simulation. These include the possibility that events discarded by the true filter or belonging to the J0 and J1 samples may pass the event selection as well as the uncertainty on the calculation (LO only) of the cross section for multi-jet events.

5.2 Event selection

The event selection is a vital step in the $t\bar{t}$ all-hadronic analysis. The interesting events have to be saved at the trigger level by keeping an acceptable trigger rate with no prescale. Then the $t\bar{t}$ all-hadronic events have to be carefully isolated from the QCD background during the event selection. The development of an efficient event selection for this analysis has been very challenging. The result achieved with a simple cut-based procedure is very satisfactory in terms of signal over background ratio and in terms of stability with respect to systematic variations. The reconstruction of the objects used in the event selection is described in Section 5.2.1. The set of variables used in the event selection and the optimisation of the cuts are described in Section 5.2.2. Finally, in Section 5.2.3, the trigger efficiency for all relevant trigger items is presented.

5.2.1 Object reconstruction

The input objects to the analysis are jets with b -tagging information, electrons, muons and MET. Jets are the key ingredient of the analysis. They are used in the event selection to distinguish $t\bar{t}$ all-hadronic events from the QCD multi-jet background and in the reconstruction to select the top quark candidates. Electrons, muons and MET are used only in the event selection to discard $t\bar{t}$ NON-all-hadronic events.

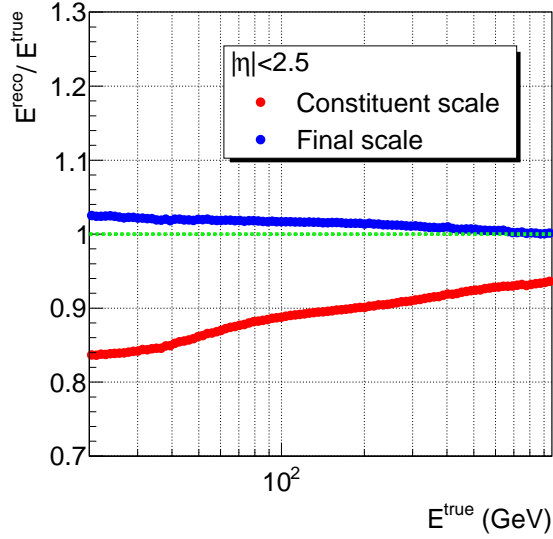


Figure 5.2: Jet energy linearity for Anti- K_T ($R = 0.4$) jets calibrated with Local Hadron Calibration using cluster level corrections only (in red) and including constituent based jet level corrections (in blue). The study is performed on $t\bar{t}$ all-hadronic events.

Jets

Jets are reconstructed using the Anti- K_T algorithm with radius parameter $R = 0.4$ [70]. They are calibrated with Local Hadron Calibration, applying both cluster level and constituent based jet level corrections, as described in Chapter 3. This calibration approach restores the energy linearity with respect to the true particle jet within 1% for QCD events [82]. The jet energy linearity in the case of $t\bar{t}$ all-hadronic events is shown in Figure 5.2 for jets calibrated with cluster level corrections only (in red) and for jets calibrated with cluster level and jet level corrections (in blue). The histograms are obtained with the same set of conventions described in Section 4.2, for true jet $|\eta| < 2.5$. The final performance in linearity shows an overshoot of about 2% for low energies. This effect is due to the difference between the sample on which the jet level corrections are calculated (QCD $2 \rightarrow 2$) that is dominated by gluon jets and the $t\bar{t}$ sample that is dominated by quark jets. Studies are on going in order to remove this residual difference. This effect is accounted for in the jet energy scale systematic error, included in the final top mass result.

In order to be included in the event selection, jets are required to have $p_T > 20$ GeV, $|\eta| < 2.5$ and to not overlap with an electron within a cone of $\Delta R = 0.2$. The cut on the jet momentum is due to the lack of available jet level corrections for lower energies and

it is very powerful in removing QCD events with lower energetic jets (and larger cross sections). The cut on the pseudorapidity is motivated by the lack of tracking (and thus b -tagging) information for larger $|\eta|$ values. The electron matching procedure aims at removing electrons that are reconstructed both as jets and as electrons.

Missing transverse energy

Missing transverse energy is reconstructed using the METRefFinal algorithm [76], which shows the best linearity performance on $t\bar{t}$ events, as discussed in Chapter 4. The missing transverse energy vector is obtained as the opposite of the vectorial sum of all transverse energy deposits in the detector.

In the METRefFinal approach the energy deposited in the calorimeter is considered on a cell basis. In order to suppress noisy cells, only cells included into calorimeter clusters are used in the calculation. The calorimeter cell energy is corrected for non-compensation effects using the global cell energy-density calibration (GC), described in Chapter 3. The cell energy is corrected for the energy lost in the cryostat with dead material corrections. A dedicated calibration is applied to the energy of cells included into clusters but not into jets, in order to properly calibrate all energy deposits in the event. For all calorimeter cells, a cell-by-cell overlap removal is performed in order to exclude from the calorimeter term the cells belonging to electrons or photons or taus. The energy deposited in the detector by electrons, photons and τ -leptons is then considered separately as provided by the optimised e , γ and τ reconstruction algorithms. Finally the energy deposited in the muon detector is considered and the small amount of energy deposited by muons into the calorimeter is removed from the calorimeter term.

The norm of the missing transverse energy vector, indicated as MET, is used in the analysis together with the scalar sum of the transverse energy of all calorimeter cells included into clusters, indicated as Sumet. The Sumet term is related to the MET resolution by the function $\sigma_{\text{MET}} = 0.5 \cdot \sqrt{\text{Sumet}}$ [76].

b -tagging

The identification of b -jets can take advantage from several properties that distinguish jets originating from b -quarks from jets originating from light quarks. The most important property is the long lifetime of hadrons containing b -quarks, which translates into a significant path length inside the detector (~ 3 mm for $p_T = 50$ GeV) before

	mis-tag rate	rejection factor
light jets	0.002	587
c -quarks	0.099	10
τ -leptons	0.014	70

Table 5.2: Mis-tag rate and rejection factor corresponding to a b -tagging efficiency of 55% for $t\bar{t}$ all-hadronic events.

decay. For this reason, the decay of a B -hadron gives rise to a secondary vertex, displaced with respect to the primary pp interaction vertex. The secondary vertex can be either reconstructed explicitly using tracking information or identified using impact parameter information. The transverse impact parameter is defined as the distance of closest approach of a track to the primary vertex, calculated in the $R - \phi$ plane. The longitudinal impact parameter is the corresponding z coordinate at the point of closest approach in $R - \phi$. Tracks originating from the secondary vertex tend to have larger impact parameters than tracks originating directly from the primary vertex.

The most advanced ATLAS b -tagging algorithm combines both secondary vertex and impact parameter information with a likelihood ratio approach (IP3D+SV1) [76]. Discriminating variables are compared to distributions obtained for both b -jets and light jets. Then the ratio of the probability for the b -jet case over the probability for the light jet case is used to calculate a b -tagging weight. Different values of the b -tagging weight correspond to different values for the b -tagging efficiency and b -tagging rejection factor.

The b -tagging efficiency is defined as the ratio of the number of jets that are originating from a b -quark and that are tagged as b -jets over the number of all jets originating from a b -quark. The rejection factor is calculated as the inverse of the mis-tag rate, which is calculated as the ratio of the number of jets that are not originating from a b -quark and that are tagged as b -jets over the number of all jets not originating from a b -quark. The mis-tag rate can as well be calculated for jets not originating from a b -quark but from c -quarks, τ -leptons and light jets, separately.

In this analysis jets are tagged as originating from a b -quark if their IP3D+SV1 weight is larger than 6, which is the ATLAS default b -tagging requirement. In order to evaluate the b -tagging performance for this b -tagging weight working point a standard jet labelling procedure is used. A jet is labeled as originating from a b -quark if a b -quark with $p_T > 5$ GeV is found in a $\Delta R = 0.3$ cone. The same is repeated for c -quarks and

τ -leptons. If no match is found the jet is considered a light jet.

The chosen b -tagging weight working point for jets reconstructed with the Anti- K_T ($R = 0.4$) algorithm, calibrated with Local Hadron Calibration, with $p_T > 15$ GeV and $|\eta| < 2.5$, corresponds to a b -tagging efficiency of 55% in $t\bar{t}$ all-hadronic events. The corresponding mis-tag rate and rejection factor for c -quarks, τ -leptons and light jets are shown in Table 5.2. The b -tagging algorithm shows very good performance in rejecting light jets (only $\sim 1/1000$ light jet is tagged as a b -jet), while the rejection of τ -leptons is more difficult ($\sim 1/100$ τ -lepton is tagged as a b -jet). The rejection of c -jets is the poorest ($\sim 1/10$ c -jet is tagged as a b -jet) and is naturally very limited by the long c -lifetime.

The b -tagging performance in terms of efficiency and mis-tag rate is overall very satisfactory for $t\bar{t}$ all-hadronic events. The use of b -tagging information is fundamental for the analysis presented in this Chapter. In fact, both event selection and top quark candidate reconstruction are based on b -jet identification. For this reason, a systematic uncertainty related to the b -tagging efficiency variation is included in the final result, as discussed in Section 5.5.

Electrons

Electrons are reconstructed with the so called egamma algorithm, which combines calorimeter information like cluster shape and cluster energy with tracking information [76]. Electrons enter the event selection if they have $p_T > 20$ GeV and $|\eta| < 2.5$. Electrons coming from semi-leptonic b -decays are excluded from this definition by requiring an isolation criteria: the energy around the electron in a cone of $\Delta R = 0.2$ has to be less than 6 GeV. This definition is developed to identify electrons coming from W leptonic decays and is used to discard $t\bar{t}$ NON-all-hadronic events.

Muons

Muons are reconstructed with the so called StacoMuon algorithm, which uses a statistical combination of the muon chambers and of the tracker information [76]. As for electrons, muons are considered in the event selection if they have $p_T > 20$ GeV and $|\eta| < 2.5$ and if they are isolated. Muons coming from semi-leptonic b -decays are excluded from this definition by requiring no overlap with a jet within a $\Delta R = 0.3$. As in the electron case, this definition is developed to identify muons coming from W leptonic decays and is used to discard $t\bar{t}$ NON-all-hadronic events.

Offline Cut	# of events $t\bar{t}$ all-had	# of events $t\bar{t}$ NON-all-had	# of events QCD +jets	# of events QCD $b\bar{b}$ +jets
no cuts	36538	43412	1.96E+008	5.11E+006
6 jets $p_T > 20$ GeV	22389	8477	1.24E+007	441021
no leptons	22193	5010	1.24E+007	439941
METsig < 6.5	22131	3051	1.24E+007	438824
Sum $E_T3 > 170$ GeV	16038	1835	3.11E+006	133685
Centrality > 0.6	10249	993	1.08E+006	48489
5 th jet $p_T > 30$ GeV	9489	889	862252	40245
4 th jet $p_T > 40$ GeV	8888	828	754790	35983
1 b -tag	7058	676	77913	28271
2 b -tag	2929	264	7657	9917
ΔR b -jets > 1.5	2130	212	2653	4775

Table 5.3: Number of events for signal and background samples after each event selection cut. An integrated luminosity of 200 pb^{-1} is assumed.

5.2.2 Event selection

The event selection for $t\bar{t}$ all-hadronic events is based on cuts on a set of variables, which exploit the different physical nature of $t\bar{t}$ events and QCD multi-jet events and of $t\bar{t}$ all-hadronic and $t\bar{t}$ NON-all-hadronic events. For each variable used in the event selection a plot is built to show the signal distribution ($t\bar{t}$ all-hadronic in red), and the background distributions ($t\bar{t}$ NON-all-hadronic in green, QCD +jets in blue, QCD $b\bar{b}$ +plus jets in magenta). Both signal and background distributions are normalised to unity in order to be able to appreciate the difference in shape among them. A black line indicating the value of the cut on the specific variable is superimposed on top of all distributions. It is important to notice that each plot is produced by taking into account the cuts applied before, in order to show the discriminating power of the variable under study. Each plot will be described separately in the following.

The cut values for the different variables are optimised simultaneously with respect to the signal significance, calculated as S/\sqrt{B} , where S indicates the number of signal events and B the number of background events. This is robust and efficient method to reject background events by keeping as many signal events as possible. The optimisation is performed by building a S/\sqrt{B} matrix in bins of cut values for 4 variables at the time. A set of 10 bins is considered for each variable, with refined bin spacing in various iterations. This is the reason why all cuts applied are round numbers. The

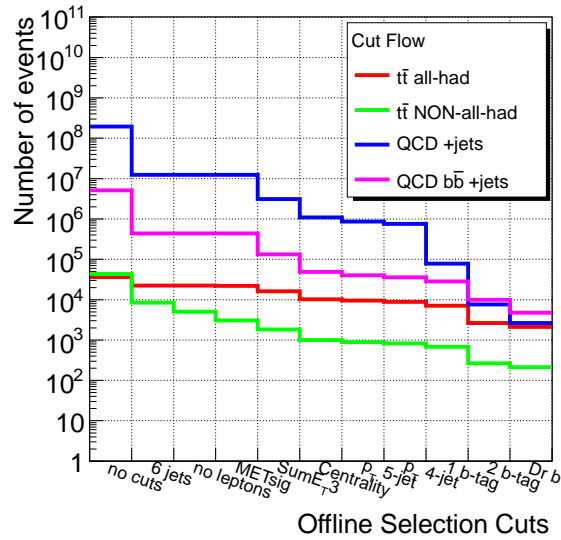


Figure 5.3: Cut Flow for the event selection.

final set of cut values is summarised in Table 5.3, where the number of events surviving each cut is reported for signal and background samples. The cut flow effect is shown in Figure 5.3, where the number of events is plotted on a logarithmic scale.

A basic pre-selection is achieved by requiring at least 6 jets and no electron or muon. All objects have to fulfil the conditions described in the previous Section (mainly $p_T > 20$ GeV and $|\eta| < 2.5$). A larger jet multiplicity than 6 is allowed, in order to take into account additional jets arising from jet splitting or gluon radiation. The veto of highly energetic isolated leptons is set to reject $t\bar{t}$ NON-all-hadronic events.

In order to fully control the separation of all-hadronic and NON-all-hadronic events, a cut on the missing transverse energy is considered, which is aimed at discarding events where the W boson decays into τ -leptons and events where electrons and muons are not well reconstructed. A cut on the MET itself (MET > 20 GeV) has shown to be less effective than a cut on the MET significance (METsig), which is defined as the ratio of MET over MET resolution. This is because fake large values of MET can arise in $t\bar{t}$ all-hadronic events, but the corresponding value of METsig is low. From the METsig distributions shown in Figure 5.4, it is possible to see that this variable has a very good discriminating power. The chosen cut value (METsig < 6.5) is very loose, because the $t\bar{t}$ NON-all-hadronic events are not a dangerous background for this analysis and a tighter cut would cost the loss of too many signal events. Nevertheless a tighter cut can be applied for an analysis based on a larger statistics or in case the final result has

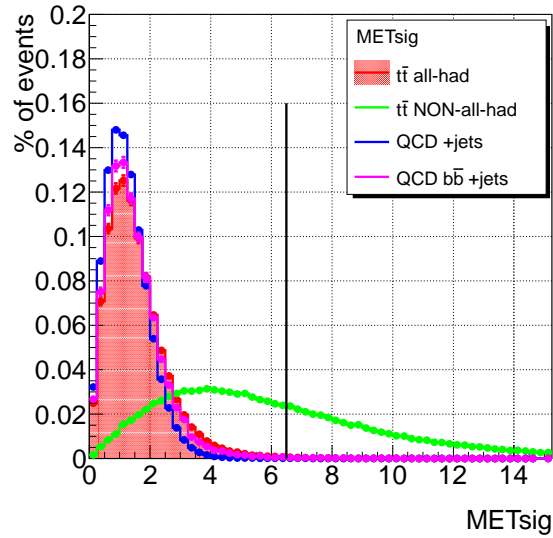


Figure 5.4: Distributions of the missing transverse energy significance for signal and background events, normalised to unity. The black line indicates the event selection cut: $\text{METsig} < 6.5$.

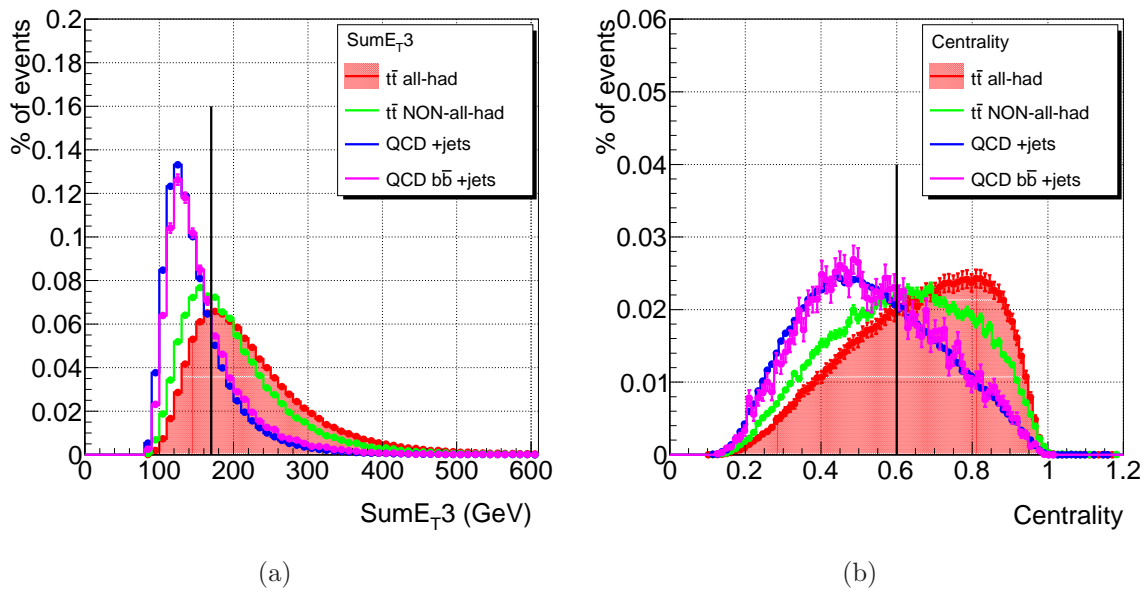


Figure 5.5: Distributions of the SumE_{T3} (a) and of the Centrality (b) for signal and background events, normalised to unity. The black line indicates the event selection cut: $\text{SumE}_{T3} > 170$ GeV (a) and Centrality > 0.6 (b).

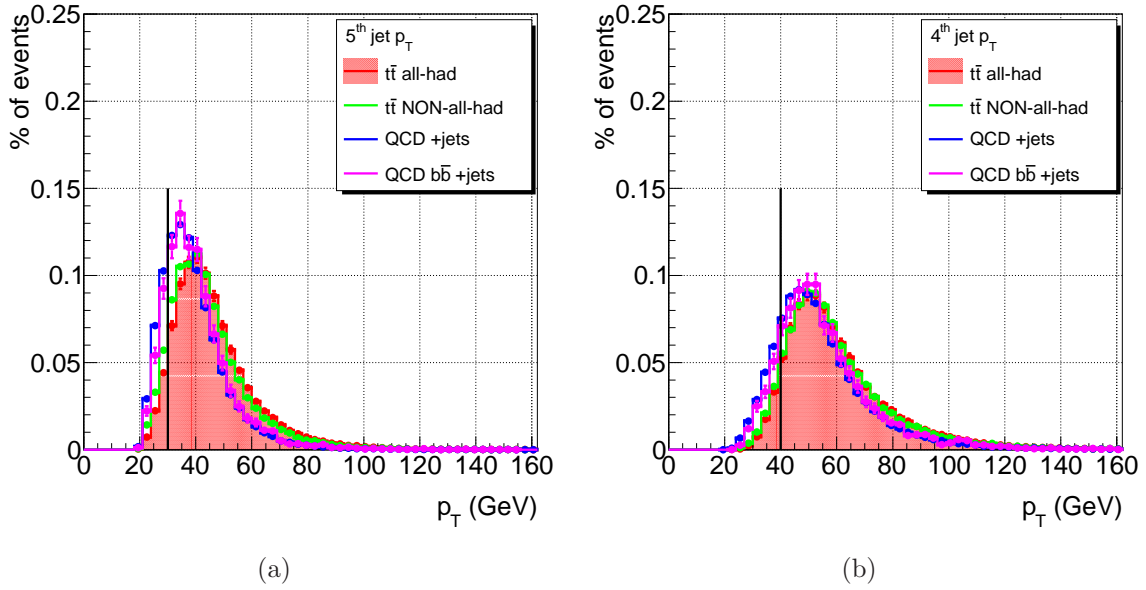


Figure 5.6: Distributions of the p_T of the 5th (a) and 4th (b) jet for signal and background events, normalised to unity. The black line indicates the event selection cut: $p_T > 30$ GeV (a) and $p_T > 40$ GeV (b).

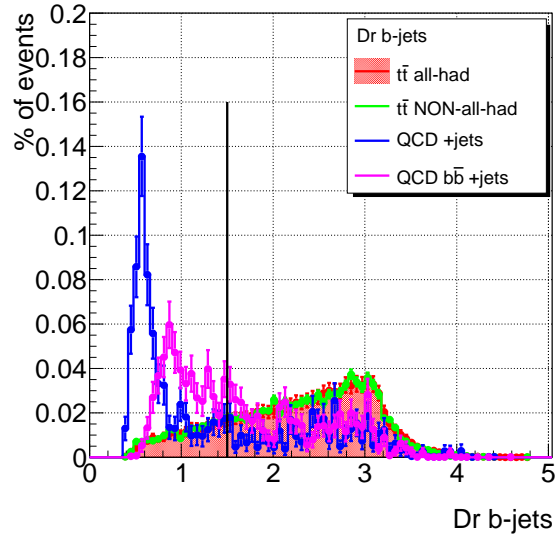


Figure 5.7: Distributions of the ΔR between the two b -tagged jets for signal and background events, normalised to unity. The black line indicates the event selection cut: $\Delta R_{b\text{-jets}} > 1.5$.

to be combined with the one obtained on $t\bar{t}$ NON-all-hadronic events.

In order to separate the $t\bar{t}$ all-hadronic events from the QCD multi-jet background topological variables are used. The $\text{Sum}E_T$ variable is calculated as the scalar sum of the transverse energy of all jets passing the reconstruction cuts. The $\text{Sum}E_{T3}$ variable is calculated by removing from $\text{Sum}E_T$ the contribution of the two jets with the highest E_T . The Centrality variable is calculated as the ratio of $\text{Sum}E_T$ over the invariant mass of all jets, which can be taken as a measure of the energy of the hard scattering. The combination of $\text{Sum}E_{T3}$ and Centrality shows the better performance in terms of S/\sqrt{B} optimisation and thus is used in the final event selection. The distributions for signal and background events are shown in Figure 5.5(a) for $\text{Sum}E_{T3}$ and in Figure 5.5(b) for Centrality. The $t\bar{t}$ all-hadronic events (and partially the $t\bar{t}$ NON-all-hadronic) tend to have larger values of $\text{Sum}E_{T3}$, because the jets with lower E_T have higher E_T in $t\bar{t}$ events than in QCD events. In fact, in $t\bar{t}$ events they come from the decay of heavy objects, while in QCD events they mainly come from parton shower. The $t\bar{t}$ all-hadronic events (and partially the $t\bar{t}$ NON-all-hadronic) have larger values of Centrality with respect to QCD events, which indicates that in $t\bar{t}$ events most of the energy is emitted in the central region of the detector. The optimised cuts for these two variables are: $\text{Sum}E_{T3} > 170$ GeV and Centrality > 0.6 .

In order to further exploit the difference in transverse energy between jets coming from $t\bar{t}$ all-hadronic and QCD events, the distribution in p_T of all 6 most energetic jets is tested. After the cut on the $\text{Sum}E_{T3}$ is applied, the jet p_T doesn't have a large discriminating power, a part from the p_T of the 5th jet (in p_T order). A cut on the p_T of the 4th jet is set in order to keep a safe margin with respect to the trigger used, as discussed in the next Section. The distributions for signal and background events are shown in Figure 5.6(a) for the p_T of the 5th jet and in Figure 5.6(b) for the p_T of the 4th jet.

After having exploited the kinematic difference between $t\bar{t}$ all-hadronic and QCD events, b -tagging information is used to reduce the number of QCD +jets events. Exactly two b -tagged jets are required in the event selection. The use of b -tagging information improves the S/B ratio from 10^{-2} to $1.6 \cdot 10^{-1}$ and it is a fundamental tool for selecting $t\bar{t}$ all-hadronic events. On the other hand, it would not be sufficient alone. In fact, by only requesting two b -tagged jets, the S/B ratio would be $7 \cdot 10^{-3}$.

In order to further improve the signal significance, the different nature of b -jets in $t\bar{t}$, QCD $b\bar{b}$ + jets and QCD +jets events can be used. In fact, b -jets in $t\bar{t}$ events are somewhat uncorrelated: they come from the separate decay of the two top quarks.

Trigger Item	Trigger Efficiency
EF_3j20	0.999
EF_3j40	0.999
EF_3j80	0.606
EF_4j20	0.999
EF_4j30	0.999
EF_4j40	0.978
EF_1b40_2b20_3L1J10	0.516
EF_1b40_2b20_3L1J20	0.516

Table 5.4: Trigger efficiency with respect to the offline event selection reported in Table 5.3. The trigger item EF_4j20 has been used for event reconstruction.

In QCD $b\bar{b}$ + jets, b -jets come from the two prompt b -quark and in QCD +jets they are produced via gluon splitting in the parton shower. For this reason, b -jets tend to be closer in ΔR in QCD $b\bar{b}$ + jets and QCD +jets events than in $t\bar{t}$ events and the ΔR between the two b -tagged jets can be used as a discriminating variable. The distributions for signal and background events for the ΔR between the two b -tagged jets are shown in Figure 5.7, in case more than two b -tagged jets are present, the two more energetic ones are considered. The optimised cut for ΔR between the two b -tagged jets is: ΔR b -jets > 1.5 .

This cut-based event selection is very powerful. It brings the S/B ratio from $\sim 10^{-4}$ to $2.8 \cdot 10^{-1}$, by keeping a signal efficiency of 6%. This result is due to the choice of variables, which have a strong discriminating power on separating signal from background events. In a future version of this analysis, after the distribution of the selection variables will be validated with data, it will be possible to use them as input to multivariate analysis techniques in order to further improve the event selection procedure.

5.2.3 Trigger

During the trigger event selection, the larger number possible of signal events has to be recorded, by keeping the trigger event rate acceptable and by avoiding prescales. The maximum trigger rate accepted depends on the instantaneous luminosity and on the fraction of trigger capability assigned to the specific trigger configuration (trigger item). Because of the very large QCD cross-section, the trigger rate for a specific trigger item can easily become too high and prescale factors become necessary. This

means that (randomly) only some of the events which fulfil the trigger selection are recorded.

The trigger selection for $t\bar{t}$ all-hadronic events is based on trigger jet objects. Trigger jets are initially defined at level 1 as the sum of trigger towers with a granularity in the $\eta - \phi$ space of 0.2×0.2 for $|\eta| < 3.2$ and of 0.4×0.4 for $|\eta| > 3.2$. The towers are combined into proto-jets by using a sliding window algorithm [76]. Trigger jets are then reconstructed at the event filter using the Cone algorithm with parameter $R = 0.7$ and are calibrated for non-compensation and dead material corrections [76].

In order to fulfil the necessity of an high signal efficiency combined with a low trigger rate, the best solution is to use multi-jet triggers. A maximum multiplicity of 4 is available in the ATLAS trigger menu. Already at the trigger level it is possible to use b -tagging information. The algorithm used is very similar to the offline b -tagging algorithm, but it uses only impact parameters as discriminating variables [76].

The performance of a trigger item for a specific analysis is evaluated in terms of the trigger efficiency with respect to the offline event selection. This is defined as the number of events passing both trigger and event selection over the number of events passing the event selection only. The trigger efficiency with respect to the offline selection described in the previous Section is reported in Table 5.4 for all available multi-jet and b -jet triggers. An acronym of the type EF_xjy has to be interpreted as trigger at the event filter level, for which x jets with $p_T > y$ GeV are requested. The acronym EF_xby means trigger at the event filter, for which x b -tagged jets with $p_T > y$ GeV are requested. For the b -jet triggers the initial level 1 trigger item is reported and is of the type xL1Jy, which means x jets at L1 with $p_T > y$ GeV.

The trigger item chosen for the rest of the analysis is EF_4j20, because it has an excellent trigger efficiency ($> 99\%$) and because it was considered unprescaled at the time of the development of these studies. Since the trigger jet calibration shows a poorer performance (offset of 10% for $p_T > 20$ GeV [76]) with respect to offline jet calibrations, the safety cut of 40 GeV on the p_T of the 4th jet is set in the offline selection. In case the trigger item EF_4j20 would be prescaled, the next choice would be EF_4j40, which would still have a very good trigger efficiency (98%) and a lower trigger rate than EF_4j20. From the loss in trigger efficiency shown by the item EF_3j80, it is possible to see that larger jet p_T values than 40 GeV have to be chosen only in case of necessity. For both b -tagging trigger items the trigger efficiency is about 50%. This effect can be explained considering the differences between the online and offline b -tagging algorithms. In order to improve the overlap of b -jets between the trigger and

the offline selection, an higher value (of at least 10% for one b -tag) of the b -tagging efficiency should be used in the trigger b -tagging algorithm with respect to the offline b -tagging algorithm [76]. In these studies the b -tagging efficiency at the event filter was about 60%, which is too low with respect to 55% in the offline analysis.

5.3 Top quark reconstruction

In order to measure the top quark mass the first step is the reconstruction of the top quark candidate four vector. This is calculated by combining the four vectors of three jets, one of which is considered to be the b -jet and the other two the W boson decay products. The case of an event selection without b -tagging (0 b -jet) is considered and includes all the requirements summarised in table Table 5.3, prior to the 1 b -tag condition. In the same way, an event selection with only 1 b -jet is considered and includes all the requirements summarised in table Table 5.3, prior to the 2 b -tag condition. Finally the complete event selection is considered (2 b -jet), which implies all requirements summarised in table Table 5.3, including the cut on the ΔR between the two b -jets. In all cases the trigger veto EF_4j20 is applied. In the events considered 6 or more jets are present. In order to allow for jet splitting or gluon radiation effects in the reconstruction of the top quark candidates, up to 7 jets that fulfil the jet reconstruction conditions (described in Section 5.2.1) are considered. These are always the jets with the highest p_T in the event. In order to identify the top quark candidates in an event, all possible jet combinations have to be considered. The calculation of the number of combinations for selecting 3 jets out of 6(7), by considering either 0,1 or 2 b -tagged jets is described in Section 5.3.1. Among these combinations, the correct ones that correspond to the top or anti-top quarks have to be selected. Various methods that can be used to identify the correct top quark candidate are described in Section 5.3.2. The top quark candidate invariant mass distribution is then investigated for the 0, 1 and 2 b -jet event selection cases and a method to extract the shape of the distribution for the QCD +jets and QCD $b\bar{b}$ + jets events in the 2 b -jet event selection case is discussed in Section 5.3.3.

5.3.1 Combinatorics

In the case of $t\bar{t}$ all-hadronic events all decay products from the two top quarks are fully reconstructed. Therefore it is possible to either reconstruct one top quark candidate

	one top with W	one top no W	top pair with W	top pair no W
0 b -tag, 6 jets	60	20	90	10
0 b -tag, 7 jets	105	35	630	70
1 b -tag, 6 jets	10	10	30	10
1 b -tag, 7 jets	15	15	180	60
2 b -tag, 6 jets	12	12	6	6
2 b -tag, 7 jets	20	20	30	30

Table 5.5: Number of jet combinations for top quark candidate reconstruction in $t\bar{t}$ all-hadronic events. Both cases of one top quark candidate and two top quark candidates (top pair) per event are considered.

or two top quark candidates per event. Among the three jets that compose one of the top quark candidates it is possible to distinguish the two jets which form the W boson candidate. In both cases the order of the jets that form the top quark candidate or the W boson candidate doesn't matter. Therefore this problem can be solved as the combination of k distinct elements out of n distinct elements:

$$C_{n,k} = \frac{n!}{k! \cdot (n-k)!} \equiv \binom{n}{k}. \quad (5.1)$$

The number of combinations corresponding to one top quark candidate per event is 20 ($C_{6,3}$) for 6 jets and 35 ($C_{7,3}$) for 7 jets. In case the W boson candidate is reconstructed, 3 ($C_{3,2}$) combinations for each top quark candidate have to be considered. This translates into 60 ($C_{6,3} \cdot C_{3,2}$) combinations for 6 jets and 105 ($C_{7,3} \cdot C_{3,2}$) combinations for 7 jets.

The number of combinations corresponding to two top quark candidates per event is 10 for 6 jets and 70 ($C_{7,6} \cdot 10$) for 7 jets. The number 10 comes from the fact that having 6 jets, for each combination of one top candidate, the second top quark candidate is automatically defined and cannot be considered separately. The number of combinations corresponding two top quark candidates per event, in case the W candidates are reconstructed, corresponds to 15 ($C_{6,4}$), which is the number of combinations to select 4 jets out of 6 (the other 2 jets are the b -jets), multiplied by 6 ($C_{4,2}$), which is the number of combinations to select the two W jets. A remark can be done on this point: from the moment that having selected a W , the second W is already defined, the actual number of combinations of W pairs is only 3. But this has to be multiplied

by 2, in order to get to the number of combinations for top quark candidates, because the two b -jets can be exchanged. This translates into 90 combinations for 6 jets and 630 ($90 \cdot C_{7,6}$) for 7 jets.

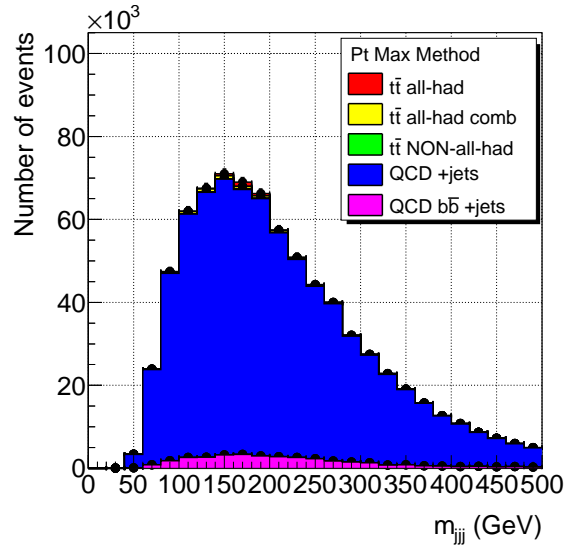
In case b -tagging is used and one or two b -jets are identified by the b -tagging algorithm, the number of combinations is reduced. In case of one top quark per event and one b -tagging, only top quark candidates including the b -jet are considered. In case of two b -tagged jets, only top quark candidates including one b -jet at the time are considered. In case of one top pair per event, the requirement of one b -jet can be used to reduce the permutations if the W candidates are reconstructed (the b -jet can't be part of the W). In case of two b -jets and two top quark candidates, the condition that the two b -jets can't be part of the same top quark candidate is used. As well in this case, only combinations including all identified b -jet are considered, which is relevant in case of 7 jets.

The final number of jet combinations for one top quark or two top quark candidates, for 6 and 7 jets, with 0, 1 or 2 b -jets, with or without W bosons reconstruction are reported in Table 5.5.

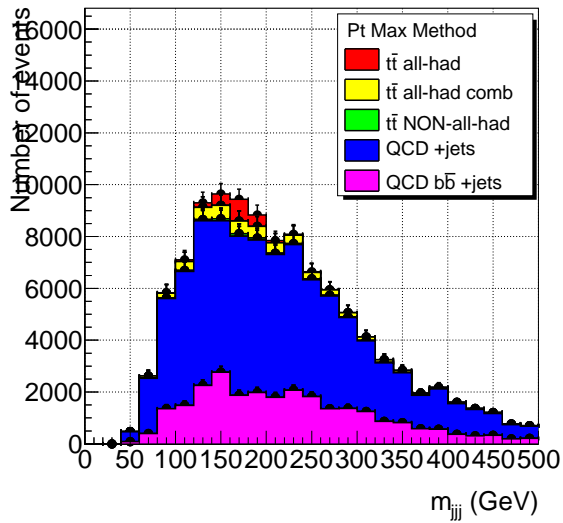
5.3.2 Top quark mass reconstruction

In order to select the correct top quark candidate among the numerous possible combinations (summarised in Table 5.5), various methods are studied. In order to determine the performance of each method in selecting the correct 3 jets combination corresponding to a top quark, a purity criterion is used. A top quark candidate is considered to be the correct choice if the corresponding 3 jet four vector matches with a top or anti-top quark true particle (from Monte Carlo event generation) within a $\Delta R = 0.2$ cone. The purity is then defined as the ratio of the number of top quark candidates selected by a method, which are correct choices, over the total number of top quark candidates selected by the same method. The selection methods studied for the $t\bar{t}$ all-hadronic analysis are described in the following. The purity is calculated using only $t\bar{t}$ all-hadronic events and applying the final event selection including 2 b -tagged jets, as summarised in Table 5.3.

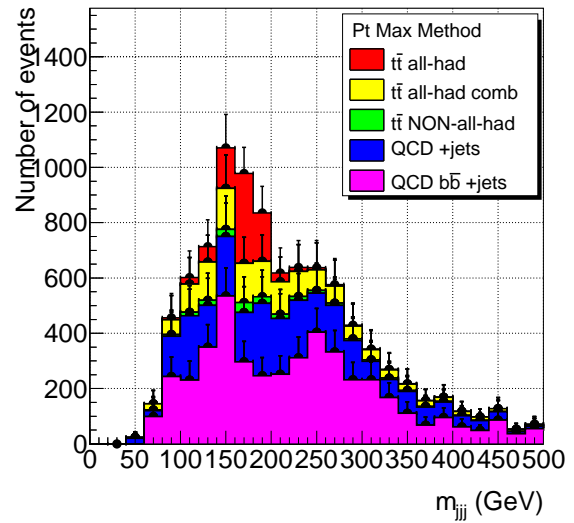
Random Method In this case one top quark candidate is selected with flat probability distribution out of all combinations for one top quark candidate per event. The corresponding purity is 12%. This method is implemented as a reference for methods based on physical criteria.



(a)



(b)



(c)

Figure 5.8: Reconstructed top quark candidate invariant mass with the Pt Max Method for events selected using the 0 b -jet event selection (a), the 1 b -jet event selection (b) and the 2 b -jet event selection (c), from Monte Carlo simulations normalised to 200 pb^{-1} of integrated luminosity.

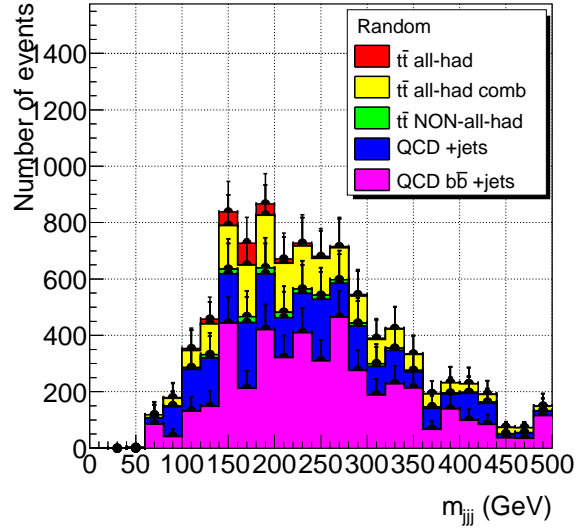


Figure 5.9: Reconstructed top quark candidate invariant mass with the Random method for events selected using the 2 b -jet event selection, from Monte Carlo simulations normalised to 200 pb^{-1} of integrated luminosity.

Pt Max Method In this case the chosen top quark candidate is the 3 jet combination with the highest p_T value. The corresponding purity is 38%.

Random Pair Method In this case the combination of two top quark candidates is selected with flat probability distribution out of all combinations for two top quark candidates per event. The corresponding purity is 11%. This method is implemented as a reference for methods based on physical criteria.

Pt Max Pair Method In this case the chosen combination of two top quark candidates is the one for which the scalar sum of the p_T of the two top quark candidates is the highest. The corresponding purity is 34%.

Min Dm Pair Method In this case the chosen combination of two top quark candidates is the one for which the difference in invariant mass between the two top quark candidates is the lowest. The corresponding purity is 21%.

The method that shows the highest purity is the Pt Max Method and it is the method chosen to select the top quark candidates for the top quark mass measurement. This method selects only one of the two top quarks reconstructed in a $t\bar{t}$ all-hadronic event. The implementation of the same strategy in case of two top quark candidates per event

(Pt Max Pair Method) shows as well very good purity performance with respect to the Random Pair Method and is a viable alternative. Adopting a method that selects pairs of top quarks can be very helpful in case the analysis is performed with a low amount of integrated luminosity of data. On the other hand it can introduce event-by-event correlations between the two top quark candidates coming from the same event, which have to be carefully evaluated.

As discussed in Chapter 1, the invariant mass of the top quark decay products corresponds to the top quark pole mass m_t^{pole} . In $t\bar{t}$ all-hadronic events the decay products are always jets and the invariant mass is calculated from the 3 jets forming the top quark candidate four vector (m_{jjj}). The distribution for m_{jjj} is used to estimate the top quark mass. The distribution for m_{jjj} obtained with the Pt Max Method on Monte Carlo simulations normalised to 200 pb^{-1} of integrated luminosity is shown in Figure 5.8, for events that pass the 0 b -jet event selection (a), the 1 b -jet event selection (b) and the 2 b -jet event selection (c). The distribution for m_{jjj} obtained with the Radom method on events that pass the 2 b -jet event selection is shown in Figure 5.9. In each distribution the contribution from $t\bar{t}$ all-hadronic events for which the top quark candidate is the correct choice is shown in red, the contribution from $t\bar{t}$ all-hadronic events for which the top quark candidate is not the correct choice (combinatorics) is shown in yellow, the contribution from $t\bar{t}$ NON-all-hadronic events is shown in green, the contribution from QCD +jets events is shown in blue and the contribution from QCD $b\bar{b}$ +jets is shown in magenta. From the distributions of Figure 5.8 it is evident that the top quark mass peak can be isolated only by using 2 b -tagged jets. At the same time, by comparing the distributions of Figure 5.8(c) and of Figure 5.9 it is possible to appreciate the impact of the purity of the top candidate selection method in isolating the top mass peak. Both plots obtained by applying the final event selection show unphysical spikes, coming mainly from the QCD $b\bar{b}$ +jets distribution. These spikes are due to the low amount of simulated integrated luminosity for the Alpgen samples and will not appear in data. In order to be able to appreciate the top quark mass peak and to develop a fit strategy by using Monte Carlo simulations, a method to extract the shape of the m_{jjj} distribution for QCD +jets and QCD $b\bar{b}$ +jets events is developed, as described in the next Section.

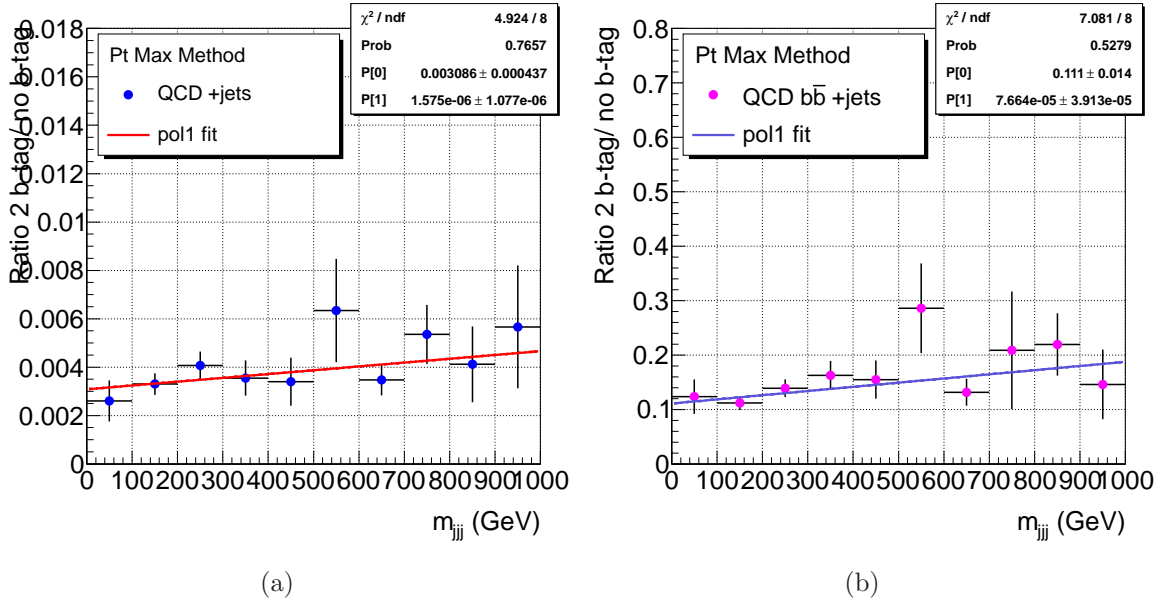


Figure 5.10: Ratio of the m_{jjj} distribution obtained by applying the 2 b -jet event selection over the m_{jjj} distribution obtained by applying the 0 b -jet event selection, fitted with a polynomial of order 1, for QCD +jets events (a) and for QCD $b\bar{b}$ +jets events (b).

5.3.3 Background shape

In order to deduce the shape of the m_{jjj} distribution for the 2 b -jet event selection, the corresponding distribution obtained with the 0 b -jet event selection is used for both QCD +jets and QCD $b\bar{b}$ +jets events. In fact, the histograms in the 0 b -jet case include enough statistics to describe the shape of the m_{jjj} distribution, as visible in Figure 5.8 (a). A ratio of the m_{jjj} distribution for the 2 b -jet case over the m_{jjj} distribution for the 0 b -jet case is constructed and then a χ^2 fit procedure is performed by using as function polynomial of order 1 ($P[0] + P[1]x$), as shown in Figure 5.10 (a) for QCD +jets and in Figure 5.10 (b) for QCD $b\bar{b}$ +jets events. The fit function is then used to rescale the 0 b -jet m_{jjj} distribution in order to derive the 2 b -jet m_{jjj} distribution with correct shape. The fit procedure takes into account the m_{jjj} shape differences introduced both by the b -tagging cuts and by the different combinatorics calculation in the two cases.

The m_{jjj} distribution obtained in case of QCD $b\bar{b}$ +jets events shows statistical fluctuations, which are still too large for the assumed integrated luminosity, as shown in Figure 5.11. In order to remove this effect, a χ^2 fit procedure is performed to model its shape information. The fit function is a linear combination of Legendre

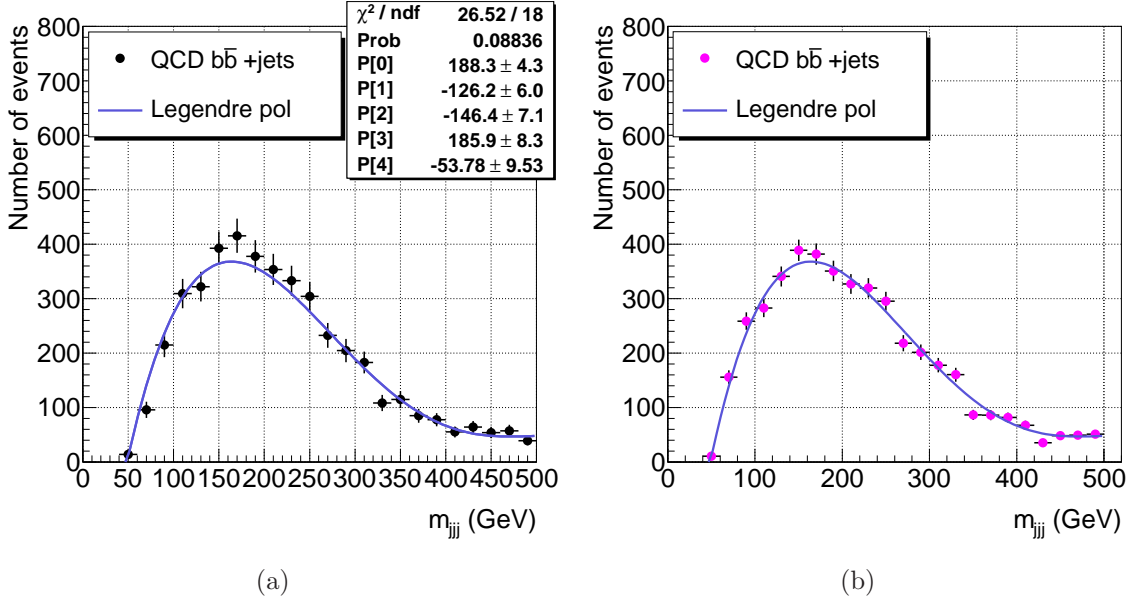


Figure 5.11: Distribution of m_{jjj} for QCD $b\bar{b}$ +jets events for the 2 b -jet event selection derived from the 0 b -jet event selection distribution, normalised to 200 pb^{-1} of integrated luminosity, with a polynomial fit (a). A m_{jjj} distribution for QCD $b\bar{b}$ +jets events, obtained from the fit function by randomly smearing the expectation value with Poissonian distribution probability (b).

polynomials [97]. The Legendre polynomials form a basis of orthogonal polynomials in the range $[-1, 1]$, with respect to the condition:

$$\int_{-1}^{+1} L_n(x) \cdot L_m(x) dx = \frac{2}{2n+1} \delta_{mn} \quad (5.2)$$

where $L_n(x)$ is the Legendre polynomial of order n and δ_{mn} is the Kronecker delta. Legendre polynomials are to be preferred to the standard basis of polynomials $(1, x, x^2, x^3 \dots)$ for fit functions that need high orders, because they are less correlated with each other and therefore allow for a better control on the convergence of the fit and on the parameter errors. The Legendre Polynomials up to the 4th order are:

$$\begin{aligned} L_0(x) &= 1, \\ L_1(x) &= x, \\ L_2(x) &= \frac{1}{2} \cdot (3x^2 - 1), \\ L_3(x) &= \frac{1}{2} \cdot (5x^3 - 3x), \\ L_4(x) &= \frac{1}{8} \cdot (35x^4 - 30x^2 + 3). \end{aligned} \quad (5.3)$$

In order to guarantee the validity of Equation 5.2, the variable x has been defined in the range $[-1, 1]$ as $x = a * m_{jjj} + b$, where $a = 2 / (m_{jjj}^{MAX} - m_{jjj}^{MIN})$, $b = 1 - a * m_{jjj}^{MAX}$ and $m_{jjj}^{MIN} = 40$ GeV, $m_{jjj}^{MAX} = 500$ GeV are the fit extremes. A linear combination of the Legendre Polynomials up to the 4th order ($\sum_i P[i] \cdot L_i$, where the $P[i]$ are the coefficient to be determined by the fit) describes the m_{jjj} distribution for QCD $b\bar{b}$ +jets events very well, as shown in Figure 5.11 (a). The fit function can then be used in order to derive typical distributions for m_{jjj} by smearing the expectation value (from the fit function) with Poissonian probability distribution. An example of how the typical distribution looks like is shown in 5.11 (b).

5.4 Pseudo-experiments and fit

In order to develop a fit procedure to be used on ATLAS data for measuring the top quark mass, pseudo-experiments are used. The top candidate invariant mass distributions for signal and background events, obtained as described in the previous Section by using the Pt Max Method, are randomly smeared around the expectation value with a Poissonian probability distribution. For the QCD $b\bar{b}$ +jets events the fit function shown in Figure 5.11 is used instead of the original distribution. The resulting distribution is a typical example of how the top quark candidate invariant mass distribution can appear in data for 200 pb^{-1} of integrated luminosity. A χ^2 fit procedure using as fit function the convolution of a Gaussian distribution for the signal (N, μ, σ fit parameters) with a linear combination of Legendre polynomials up to the 4th order for the background ($P[i]$ fit parameters) is then used in order to estimate the top quark mass: the mean of the Gaussian distribution μ is to be identified with the measured top quark mass m_t . In Figure 5.12 (a) a m_{jjj} pseudo-experiment distribution is shown together with the combined fit function (in black), the Legendre polynomial part (in blue) and the Gaussian part (in red). The fit performs very well ($\chi^2/ndf = 1.2$) and the estimated value for the top quark mass is $m_t = 168.8 \pm 2.1$ GeV. In Figure 5.12 (b) the contribution to the m_{jjj} pseudo-experiment distribution from $t\bar{t}$ all-hadronic events for which the top quark candidate is the correct choice is shown in red, the contribution from $t\bar{t}$ all-hadronic events for which the top quark candidate is not the correct choice (combinatorics) is shown in yellow, the contribution from $t\bar{t}$ NON-all-hadronic events is shown in green, the contribution from QCD +jets events is shown in blue and the contribution from QCD $b\bar{b}$ +jets events is shown in magenta. The combined fit function (in black) together with the background (in blue) and signal (in red) functions

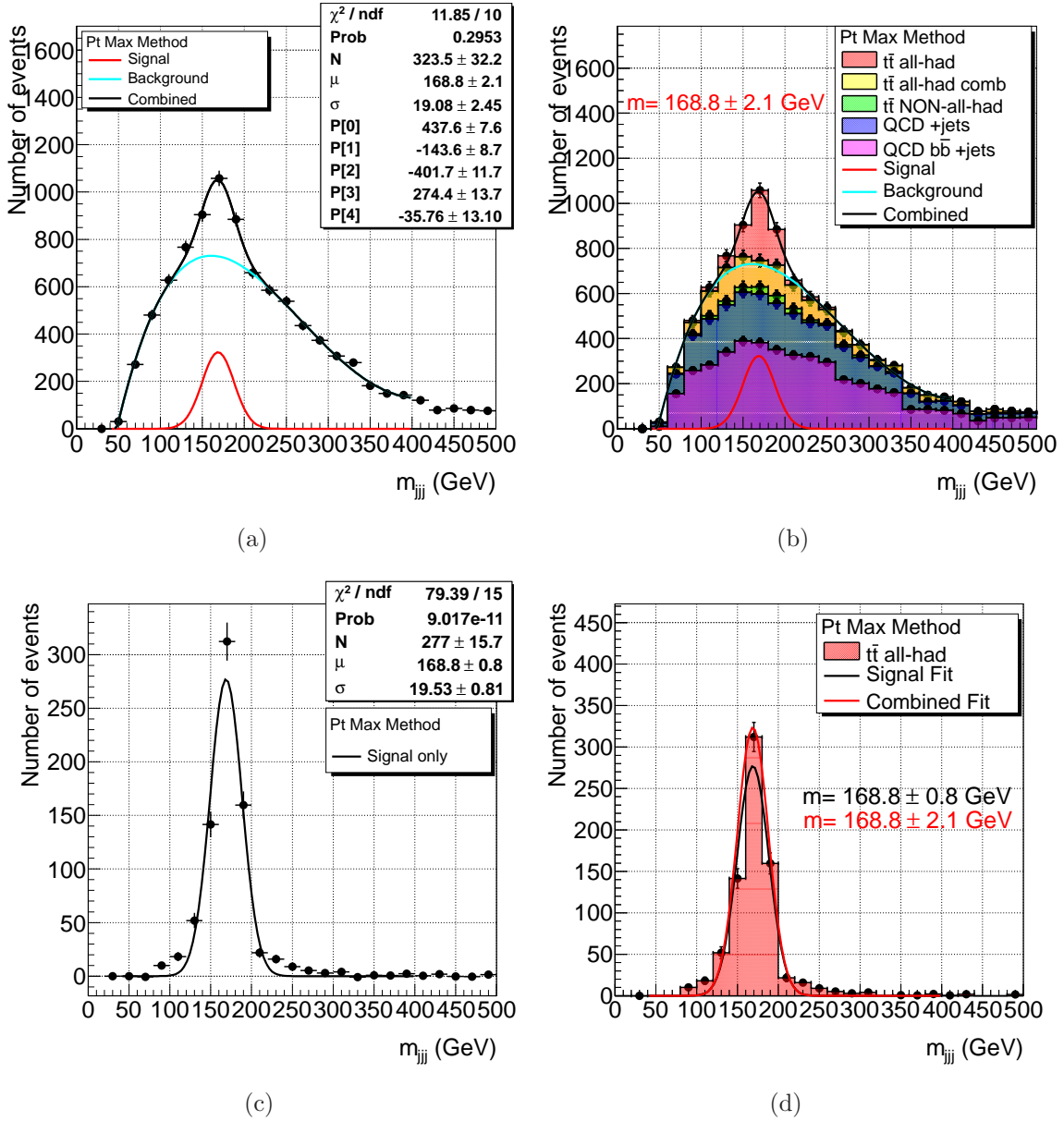


Figure 5.12: Distribution for the top quark candidate invariant mass from a Poissonian fluctuated pseudo-experiment for 200 pb^{-1} of integrated luminosity. (a) A combined fit is performed on the final distribution (in black), by using a convolution of a Gaussian function for the signal (in red) and a linear combination of Legendre polynomials for the background (in blue). (b) The various contribution to the invariant mass distribution, coming from $t\bar{t}$ events and QCD events are shown together with the result of the fit procedure. (c) Contribution to the invariant mass distribution from $t\bar{t}$ all-hadronic events for which the top quark candidate is the correct choice. A fit with a Gaussian function is performed (in black). (d) The result of the fit is shown (in black) together with the Gaussian component of the combined fit (in red) on top of the invariant mass distribution (in red).

are superimposed to the m_{jjj} distribution. The background fit function follows the shape of the background distribution quite closely; in fact the $t\bar{t}$ all-hadronic combinatorics is considered a background with respect to the top quark mass estimation. This agreement can be partially attributed to the fact that a combination of Legendre polynomials up to the 4th order is used to model the shape information of the m_{jjj} distribution from QCD $b\bar{b}$ +jets events. In order to assess the impact of this choice on the final result a systematic uncertainty is calculated by varying of ± 1 the order of the Legendre polynomials of the combination used to model the shape information of the m_{jjj} distribution from QCD $b\bar{b}$ +jets. For the signal as well the fit function follows the shape of the signal distribution closely. In order to focus on the signal only, the pseudo-experiment distribution of m_{jjj} for the $t\bar{t}$ all-hadronic events for which the top quark candidate is the correct choice is shown in Figure 5.12 (c-d). A χ^2 fit procedure using a Gaussian function is performed on the m_{jjj} signal only distribution, giving a result of $m_t = 168.8 \pm 0.8$ GeV, which confirms that the combined fit correctly describes the backgrounds. The difference of the result obtained with the signal only events to true top quark mass $m_t^{MC} = 172.5$ GeV can be interpreted as a bias due to missing b -jet energy calibration, as discussed in Section 5.6. In Figure 5.12 (c) the Gaussian fit is shown and in Figure 5.12 (d) the m_{jjj} distribution for the signal is shown together with the Gaussian function from the combined fit (in red) and the Gaussian function from the signal only fit (in black).

The systematic errors on the result of the fit procedure are estimated as discussed in the next Section. The compatibility of the result of the fitting procedure with respect to the Monte Carlo true top quark mass is then discussed in terms of its pull distribution as a conclusion to this Chapter, in Section 5.6.

5.5 Systematic uncertainties

In order to estimate the systematic uncertainty on the measurement of the top quark mass obtained by using the fit procedure described in Section 5.4, different parameters of the analysis are varied and the final result is recalculated. When possible the parameter under consideration is varied by $\pm 1\sigma$ with respect to the default case. For each considered effect the systematic error on m_t is calculated as the maximum of the absolute difference between the result obtained with the reference parameter and the value obtained with the varied parameter $\text{Max}(|m_t^{ref} - m_t^{sys+\sigma}|, |m_t^{ref} - m_t^{sys-\sigma}|)$. The reference value $m_t^{ref} = 168.8 \pm 2.1$ GeV is given by the fit performed on the

Source of Uncertainty	Systematic Uncertainty on m_t (GeV)
background shape	± 0.6
background normalisation ($\pm 50\%$)	± 0.3
jet energy scale ($\pm 5\%$)	± 7.1
b -jet energy scale ($\pm 2.5\%$)	± 1.6
b -tagging efficiency ($\pm 5\%$)	± 0.5
Total	± 7.3

Table 5.6: Various sources of systematic uncertainty on m_t and their contribution.

pseudo-experiment shown in Figure 5.12 and each $m_t^{sys\pm\sigma}$ is obtained under the same pseudo-experiment conditions. The effects considered for the estimation of the systematic uncertainty are the uncertainty on the methods used to estimate the shape of the m_{jjj} distribution for the backgrounds, the uncertainty on the background normalisation, the uncertainty on the light jet and b -jet energy scale and the uncertainty on the b -tagging efficiency. A summary of the systematic uncertainty on the measurement of m_t from the various sources considered is provided in Table 5.6. The total systematic uncertainty is calculated by summing all contribution, considered statistically independent, in quadrature and amounts to ± 7.3 GeV. The estimation of the uncertainty from the individual contributions is described in the following.

Background shape

Because of the lack of simulated statistics for the QCD +jets and QCD $b\bar{b}$ +jets events, it is necessary to estimate the systematic error on m_t due to the fit procedure used to extract the shape of the m_{jjj} distribution after the final event selection, which is described in Section 5.3.3. This procedure implies a fit to the ratio of the 2 b -jet m_{jjj} distribution over the 0 b -jet m_{jjj} distribution and then a fit to the derived QCD $b\bar{b}$ +jets m_{jjj} distribution. In order to estimate the systematic error on m_t due to the background shape extraction, in both cases each of the fit parameters should be varied inside the error given by the fit procedure. In order to vary the parameter values correctly, the correlations among them have to be accounted for. These correlations are contained in the fit error covariance matrix, which is a symmetric matrix by definition [98]. For a symmetric matrix A the following properties hold [99]:

- an orthogonal matrix V exists, such that $A = VDV^{-1} = VDV^T$;

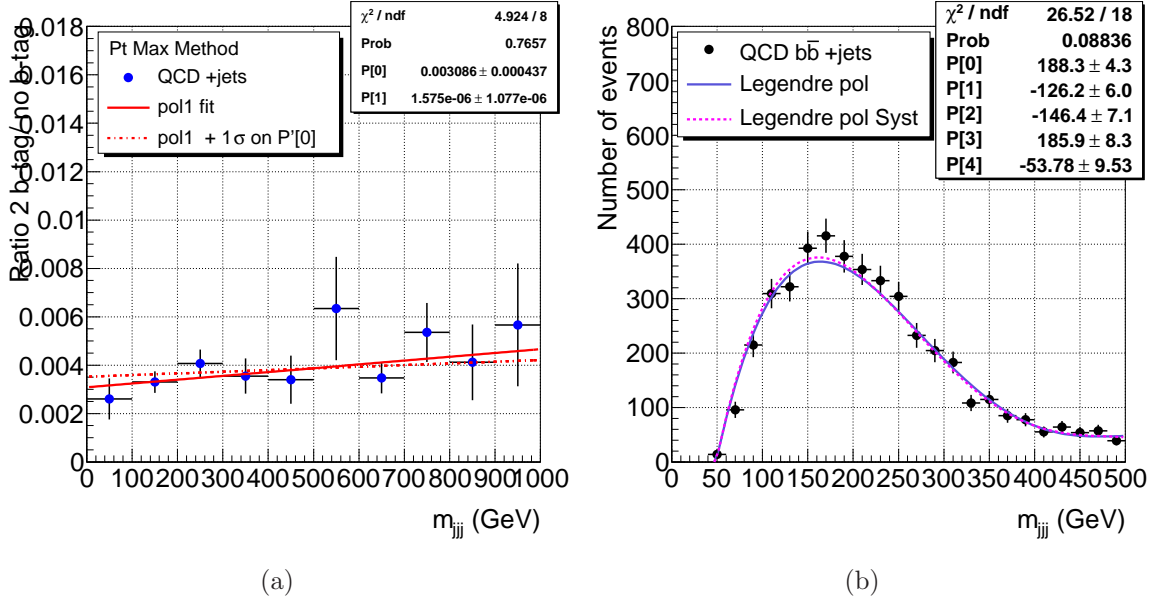


Figure 5.13: Impact of the variation of the fit parameter $P'[0]$ by $+\sigma$ for the fit to the ratio of the 2 b -jet m_{jjj} distribution over the 0 b -jet m_{jjj} distribution, in case of QCD + jets events (a). Impact of the variation of the fit parameter $P'[0]$ by $-\sigma$ for the fit to derived QCD $b\bar{b}$ +jets m_{jjj} distribution. The original fit function is drawn as a solid line and the varied fit function is drawn as a dashed line.

- the eigenvalues of A , which appear on the diagonal of D , are real;
- the columns of V are a basis of orthonormal eigenvector of A .

Therefore it is possible to diagonalise the covariance matrix, obtaining the corresponding basis of orthonormal eigenvectors. This basis is used to transform the vector of the fit parameters \mathbf{P} into its corresponding vector in the space of the orthonormal eigenvectors \mathbf{P}' . Then, separately, each new fit parameter is varied by $\pm\sigma$, where σ is obtained as $\sqrt{D_{ii}}$. After the variation takes place, the parameter vector \mathbf{P}' is transformed back into the parameter vector \mathbf{P} and the analysis is repeated [100]. The effect of varying the parameter $P'[0]$ by $+\sigma$ for the ratio of the 2 b -jet over the 0 b -jet m_{jjj} distribution is shown in Figure 5.13 (a), for the QCD +jets events. The original fit function is drawn in red and the varied fit function in dashed red. In the same way the effect of varying the parameter $P'[0]$ by $-\sigma$ for the derived QCD $b\bar{b}$ +jets m_{jjj} distribution is shown in Figure 5.13 (b). The original fit function is drawn in violet and the varied fit function in dashed magenta. This exercise is repeated for the 2 fit parameters of the polynomial of order 1 used for the ratio distribution, for both QCD +jets and QCD $b\bar{b}$ +jets events. The new m_t obtained in each case and its difference from the reference

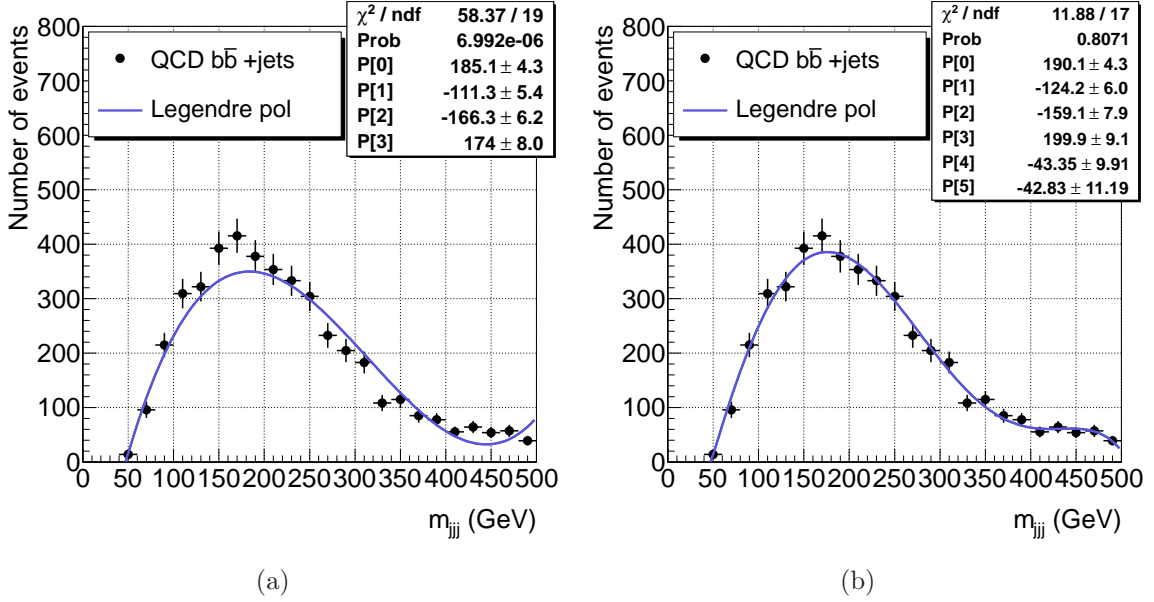


Figure 5.14: Impact of the variation of the order of the Legendre polynomials used to describe the QCD $b\bar{b}$ + jets m_{jjj} distribution. Legendre polynomials up to the 3rd order are considered in (a) and Legendre polynomials up to the 5th order are considered in (b).

value are reported in Table 5.7. In the same way, the 5 fit parameters of the linear combination of Legendre polynomials used for the fit to the QCD $b\bar{b}$ + jets distribution are varied and the results are reported in Table 5.8.

A combination of Legendre polynomials up to the 4th order is used both to extract the background shape of the m_{jjj} distribution for QCD $b\bar{b}$ + jets events and to describe all backgrounds in the combined fit. The impact of this choice on the final result is assessed by varying of ± 1 the order of the combination used to model the QCD $b\bar{b}$ + jets distribution. The fits to the QCD $b\bar{b}$ + jets distribution obtained in the two cases are shown in Figure 5.14. The new m_t obtained in each case and its difference from the reference value are reported in Table 5.9.

For both types of variation the impact on the m_t estimation is small: by summing up all contributions, the systematic uncertainty is ± 0.6 GeV. This is an indication that the errors on the fit parameters are calculated correctly and that the fit procedure is stable with respect to the considered variations of the background shape.

With respect to this study, it is important to stress why, even if a set of orthogonal polynomials is used for the initial fit, the fit parameters are correlated. In order to

	QCD +jets $P'[0] +1\sigma$	QCD +jets $P'[0] -1\sigma$	QCD +jets $P'[1] +1\sigma$	QCD +jets $P'[1] -1\sigma$
m_t^{sys} (GeV)	168.7 ± 2.1	168.8 ± 2.1	168.8 ± 2.1	168.7 ± 2.1
$m_t^{sys} - m_t^{ref}$ (GeV)	-0.1	-	-	-0.1
	QCD $b\bar{b}$ +jets $P'[0] +1\sigma$	QCD $b\bar{b}$ +jets $P'[0] -1\sigma$	QCD $b\bar{b}$ +jets $P'[1] +1\sigma$	QCD $b\bar{b}$ +jets $P'[1] -1\sigma$
m_t^{sys} (GeV)	168.7 ± 2.2	168.8 ± 2.1	168.8 ± 2.1	168.7 ± 2.1
$m_t^{sys} - m_t^{ref}$ (GeV)	-0.1	-	-	-0.1

Table 5.7: Systematic uncertainty obtained by varying the parameters (\mathbf{P}') of the fit to the ratio of the 2 b -jet m_{jjj} distribution over the 0 b -jet m_{jjj} distribution, for both QCD +jets and QCD $b\bar{b}$ +jets events. The value of m_t^{sys} obtained for each variation and its difference to the reference value $m_t^{sys} - m_t^{ref}$ are reported.

	QCD $b\bar{b}$ +jets $P'[0] +1\sigma$	QCD $b\bar{b}$ +jets $P'[0] -1\sigma$	QCD $b\bar{b}$ +jets $P'[1] +1\sigma$	QCD $b\bar{b}$ +jets $P'[1] -1\sigma$
m_t^{sys} (GeV)	168.7 ± 2.1	168.8 ± 2.1	168.8 ± 2.1	168.7 ± 2.1
$m_t^{sys} - m_t^{ref}$ (GeV)	-0.1	-	-	-0.1
	QCD $b\bar{b}$ +jets $P'[2] +1\sigma$	QCD $b\bar{b}$ +jets $P'[2] -1\sigma$	QCD $b\bar{b}$ +jets $P'[3] +1\sigma$	QCD $b\bar{b}$ +jets $P'[3] -1\sigma$
m_t^{sys} (GeV)	168.8 ± 2.1	168.8 ± 2.1	168.8 ± 2.1	168.7 ± 2.1
$m_t^{sys} - m_t^{ref}$ (GeV)	-	-	-	-0.1
	QCD $b\bar{b}$ +jets $P'[4] +1\sigma$	QCD $b\bar{b}$ +jets $P'[4] -1\sigma$		
m_t^{sys} (GeV)	168.8 ± 2.1	168.8 ± 2.1		
$m_t^{sys} - m_t^{ref}$ (GeV)	-	-		

Table 5.8: Systematic uncertainty obtained by varying the parameters (\mathbf{P}') of the fit to the derived QCD $b\bar{b}$ +jets m_{jjj} distribution. The value of m_t^{sys} obtained for each variation and its difference to the reference value $m_t^{sys} - m_t^{ref}$ are reported.

	QCD $b\bar{b}$ +jets - 1 order	QCD $b\bar{b}$ +jets + 1 order
m_t^{sys} (GeV)	168.7 ± 2.2	168.3 ± 2.1
$m_t^{sys} - m_t^{ref}$ (GeV)	-0.1	-0.5

Table 5.9: Systematic uncertainty obtained by varying of ± 1 the order of the Legendre polynomials considered to describe the m_{jjj} distribution from QCD $b\bar{b}$ +jets events. The value of m_t^{sys} obtained for each variation and its difference to the reference value $m_t^{sys} - m_t^{ref}$ are reported.

have a set of uncorrelated parameters, and therefore a diagonal covariant matrix, the polynomials used in the fit should satisfy the following condition [98]:

$$\sum_{n=0}^N P_i(x_n) \cdot P_j(x_n) = c_{ij} \delta_{ij} \quad (5.4)$$

where $\{x_n\}$ is the set of measurements for which the fit is performed. For any set of $\{x_n\}$, it is possible to find a basis of polynomials for which Equation 5.4 is valid [98], which can be calculated by using a Gram-Schmidt orthonormalization procedure [101]. The covariant matrix of the fit with the Legendre polynomials is not diagonal because the integral relation given by Equation 5.2, which defines the polynomial orthogonality, is not equivalent to the discrete relation given by Equation 5.4. It is as well interesting to notice that the Chebyshev polynomials of the first kind, which can be a choice for the fit to the background of the m_{jjj} distribution, obey the relation [102]:

$$\sum_{k=1}^N C_i(x_k) \cdot C_j(x_k) = \begin{cases} \frac{1}{2}N\delta_{ij} & i, j \neq 0 \\ N & i, j = 0 \end{cases}, \quad (5.5)$$

where $C_i(x)$ is a Chebyshev polynomial of order i and $\{x_k\}$ is the set of zeros of the polynomial $C_N(x)$. Despite of the misleading resemblance, Equation 5.4 and Equation 5.5 are not equivalent and should not be confused.

Background normalisation

The predicted rate for QCD multi-jet events at the LHC suffers from a large theoretical uncertainty. The calculations are possible at LO only and the Monte Carlo simulations used are generated for collisions at a centre of mass energy (10 TeV), which is not yet

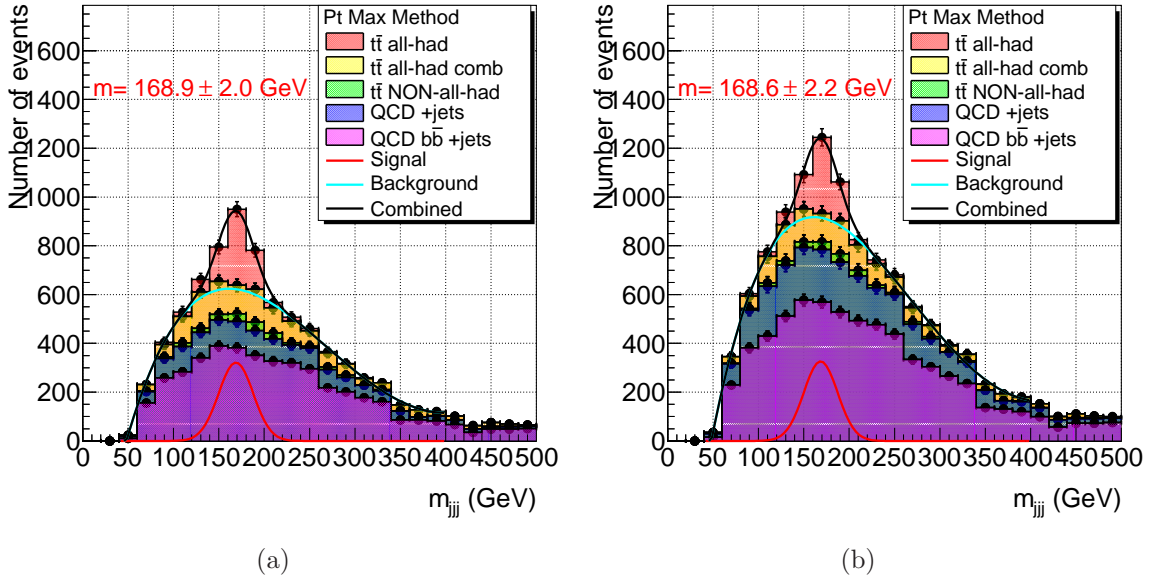


Figure 5.15: Distribution for the top quark candidate invariant mass from a Poissonian fluctuated pseudo-experiment for 200 pb^{-1} of integrated luminosity. The various contributions to the invariant mass distribution, coming from $t\bar{t}$ events and QCD events are shown together with the result of the fit procedure. The effect of scaling the QCD +jets normalisation by -50% is shown in (a) and the effect of scaling the QCD $b\bar{b}$ +jets normalisation by $+50\%$ is shown in (b).

probed experimentally. Once the analysis will be performed on data, the rate can be measured directly, the simulations can be tuned with respect to the measured rate and the uncertainty can be reduced.

In order to estimate the impact of the QCD multi-jet rate uncertainty, the normalisation of each of the QCD +jets and QCD $b\bar{b}$ +jets m_{jjj} distributions is varied by $\pm 50\%$. The effect of this variation on the final pseudo-experiment distribution is shown in Figure 5.15 (a) for scaling the QCD +jets normalisation by -50% and in (b) for scaling the QCD $b\bar{b}$ +jets normalisation by $+50\%$. The m_t obtained in each case and its difference from the reference value are reported in Table 5.10.

The impact of the QCD multi-jet rate uncertainty on the measurement of m_t is small and amounts to $\pm 0.3 \text{ GeV}$. This is an indication that the S/B ratio obtained with the final event selection is sufficiently high to make the analysis stable with respect to the QCD multi-jet rate uncertainty.

	QCD +jets # +1 σ	QCD +jets # -1 σ	QCD $b\bar{b}$ +jets # +1 σ	QCD $b\bar{b}$ +jets # -1 σ
m_t^{sys} (GeV)	168.6 ± 2.3	168.9 ± 2.0	168.6 ± 2.2	168.9 ± 2.0
$m_t^{sys} - m_t^{ref}$ (GeV)	-0.2	+0.1	-0.2	+0.1

Table 5.10: Systematic uncertainty obtained by varying the normalisation of the QCD +jets and of the QCD $b\bar{b}$ +jets m_{jjj} distribution by $\pm 50\%$. The value of m_t^{sys} obtained for each variation and its difference to the reference value $m_t^{sys} - m_t^{ref}$ are reported.

	JES +1 σ	JES -1 σ	b -JES +1 σ	b -JES -1 σ
m_t^{sys} (GeV)	175.8 ± 2.6	161.7 ± 2.0	170.4 ± 2.2	167.5 ± 2.0
$m_t^{sys} - m_t^{ref}$ (GeV)	+7.0	-7.1	+1.6	-1.3

Table 5.11: Systematic uncertainty obtained by varying the jet energy scale by $\pm 5\%$ and the b -jet energy scale by $\pm 2.5\%$. The value of m_t^{sys} obtained for each variation and its difference to the reference value $m_t^{sys} - m_t^{ref}$ are reported.

Jet energy scale

The uncertainty on the jet energy scale is the most important contribution to the systematic uncertainty on the measurement of m_t . In first instance, the jet energy plays a very important role in the event selection, which is based on variables built from the jet transverse energy. Then the calculation of the invariant mass (m_{jjj}) for each top candidate depends directly on the energy of the three jets involved. In order to estimate the impact of the jet energy scale uncertainty, the energy of all jets in the event is scaled by $\pm 5\%$ and the whole analysis is repeated. A larger impact on the measurement of m_t is expected to derive from the b -jet energy scale. In fact, b -jets can include semi-leptonic decays from b or c quarks, which imply the deposit of part of the jet energy as muons or neutrinos. No corrections are included in the Local Hadron Calibration schema for these effects, because the definition of the true particle jet does not include muons and neutrinos. In order to estimate the impact of the b -jet energy scale uncertainty, the energy of the jets that match with a b -quark in a cone of $\Delta R = 0.3$ is scaled by $\pm 2.5\%$ and the whole analysis is repeated. The effect of these variations on the final pseudo-experiment distribution is shown in Figure 5.15 (a) for scaling the jet energy by +5% and in (b) for scaling the jet energy by -5%. The m_t obtained in each case and its difference from the reference value are reported in Table 5.11. The impact

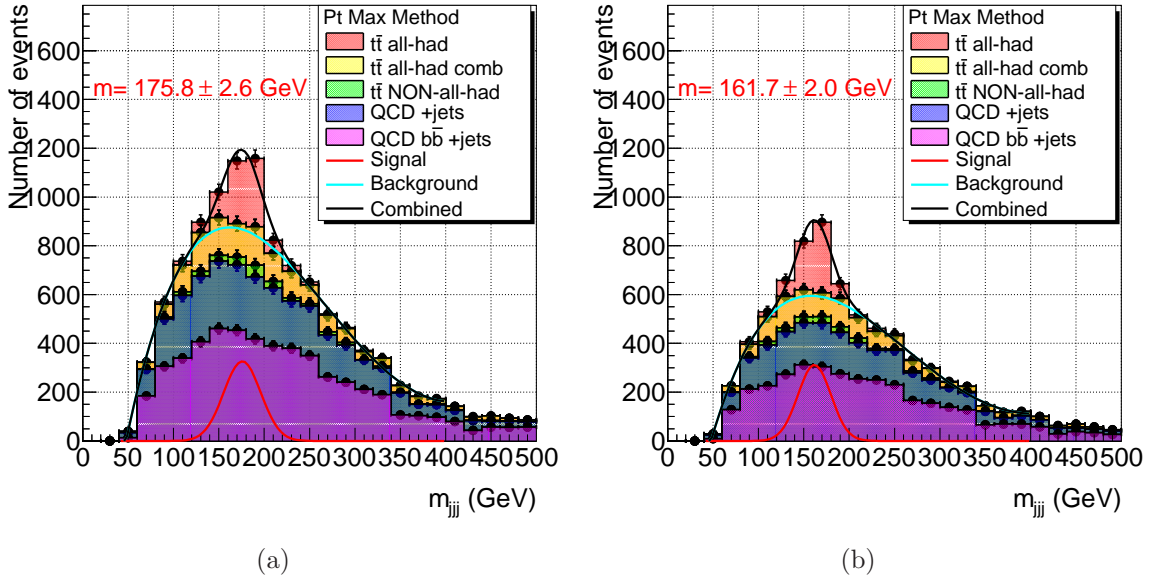


Figure 5.16: Distribution for the top quark candidate invariant mass from a Poissonian fluctuated pseudo-experiment for 200 pb^{-1} of integrated luminosity. The various contribution to the invariant mass distribution, coming from $t\bar{t}$ events and QCD events are shown together with the result of the fit procedure. The effect of scaling the jet energy scale by +5% is shown in (a) and the effect of scaling the jet energy scale by -5% is shown in (b).

of the jet energy scale uncertainty on the measurement of m_t is very large and amounts to $\pm 7.1 \text{ GeV}$. An additional uncertainty of $\pm 1.6 \text{ GeV}$ comes from the b -jet energy scale. In order to reduce these uncertainties, the distribution of the stabilised invariant mass can be considered as an estimator for m_t [103]. This consists in dividing the invariant mass of the top quark candidate m_{jjj} by the invariant mass of the corresponding W boson candidate and then in multiplying the ratio by the known value of the W boson mass. This method has shown to reduce the systematic uncertainty to 4 GeV for the top mass analysis in the $t\bar{t}$ semi-leptonic channel. Concerning the b -jet energy scale contribution, it can be reduced with dedicated jet energy corrections. It is as well possible to optimise the jet and b -jet energy scale together while performing the top quark mass measurement, by using multi-dimensional template methods or the matrix element method [104].

	BTAG $+1\sigma$	BTAG -1σ
m_t^{sys} (GeV)	168.3 ± 2.1	168.9 ± 2.1
$m_t^{sys} - m_t^{ref}$ (GeV)	-0.5	+0.1

Table 5.12: Systematic uncertainty obtained by varying the b -tagging efficiency by $\pm 5\%$. The value of m_t^{sys} obtained for each variation and its difference to the reference value $m_t^{sys} - m_t^{ref}$ are reported.

b -tagging efficiency

The use of b -tagging information is fundamental for this analysis. In first instance, as discussed in Section 5.2.2, b -tagging information is vital for the event selection. Moreover the request for 2 b -jets helps in reducing the number of combinations per event and therefore the combinatorics background.

In order to estimate the impact of b -tagging algorithm uncertainties, the b -tagging efficiency is varied by $\pm 5\%$ and the whole analysis is repeated. The m_t obtained in each case and its difference from the reference value are reported in Table 5.12. The systematic uncertainty due to this effect amounts to ± 0.5 GeV. This derives mainly from raising the b -tagging efficiency, which corresponds to higher mis-tag rates. The impact of the b -tagging efficiency uncertainty on the measurement of m_t is very small. This is an indication that the analysis is stable with respect to the uncertainty on the b -tagging algorithm efficiency.

5.6 Results

In this Chapter the prospects for measuring the top quark mass in the $t\bar{t}$ all-hadronic channel with the ATLAS detector are investigated. A study is performed on Monte Carlo simulations for pp collisions at a centre of mass energy of 10 TeV, considering 200 pb^{-1} of integrated luminosity. The analysis includes the use of a cut-based event selection with two b -tagged jets and is based on a χ^2 fitting procedure performed on the top quark candidate invariant mass. With a true top quark mass of $m_t^{MC} = 172.5$ GeV as input to the simulation, the measured top quark mass for a typical pseudo-experiment is:

$$m_t = 168.8 \pm 2.1|_{stat} \pm 7.3|_{sys} \text{ GeV} . \quad (5.6)$$

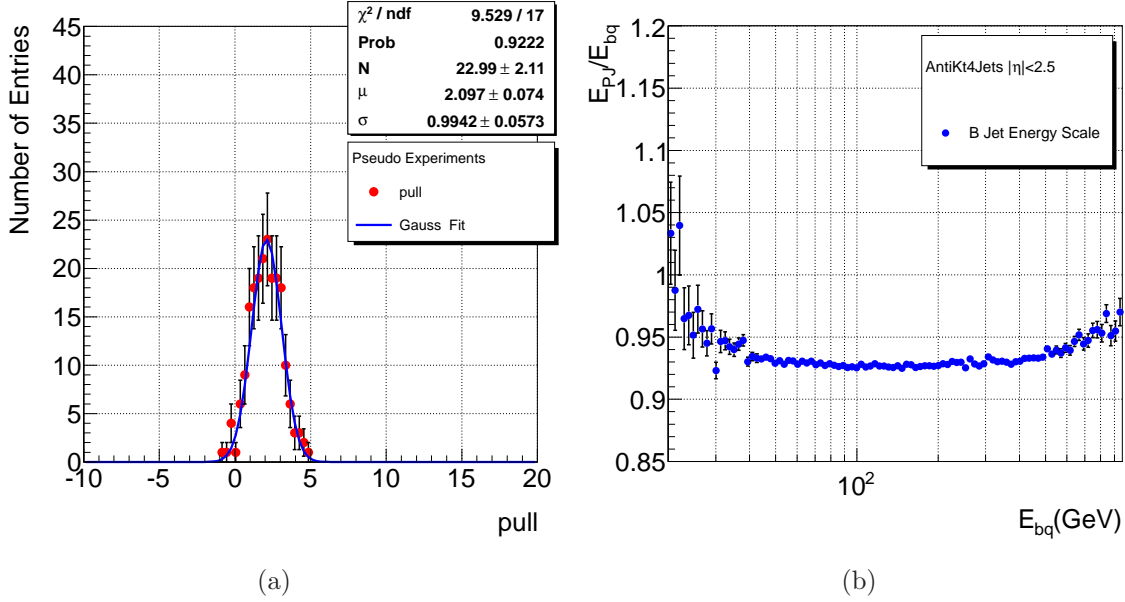


Figure 5.17: Pull distribution for m_t with respect to the true Monte Carlo mass $m_t^{MC} = 172.5$ GeV for 200 Poissonian fluctuated pseudo-experiments (a). Jet energy linearity for true particle jets matching with a b -quark, with respect to the b -quark energy (b).

In order to test the consistency of the result obtained by using the fitting procedure with respect to the true top quark Monte Carlo mass, a pull distribution is used [105]. The pull variable is defined as:

$$\frac{m_t^{MC} - m_t}{\sigma_{stat}}, \quad (5.7)$$

where σ_{stat} indicates the statistical error from the fitting procedure. For a large number of measurements of m_t , the pull variable has to be distributed as a standard Gaussian (with mean 0 and width 1). For the measurement of m_t with the fitting procedure described in Section 5.4, the pull distribution is obtained by randomly generating 200 Poissonian fluctuated pseudo-experiments. The resulting distribution is shown in Figure 5.17 (a) together with a Gaussian fit. The width of the distribution ($\sigma_p = 0.99 \pm 0.06$) is consistent with unity and therefore it is possible to say that the statistical error on m_t is calculated correctly. The mean of the pull distribution ($\mu_p = 2.10 \pm 0.07$) is not consistent with 0. This indicates the presence of a systematic bias in the analysis. The bias can be estimated by considering that the mean of the statistical uncertainty on m_t over the 200 pseudo-experiments is 2.25 GeV and therefore the shift of m_t with respect to m_t^{MC} given by the pull distribution is about (-)4.7 GeV.

The cause of this bias can be explained in terms of missing b -jet energy scale cor-

rections. In order to estimate the magnitude of the effect, the b -jet energy linearity is studied. This is calculated as the mean of the ratio of the true particle jet energy over the true b -quark energy (E_{PJ}/E_{bq}) versus the b -quark energy (E_{bq}). Only true jets which match with a b -quark (with $E_T > 14$ GeV and $|\eta| < 2.5$) within a cone of $\Delta R = 0.1$ are considered. The b -jet energy scale linearity is shown in Figure 5.17 (b). The linearity shows a raising tale for low energies, which is due to the fact that the cut on the b -quark transverse energy is loose. The average linearity undershoot is about 7% for the whole energy spectrum. This figure can be explained mainly in terms of the b -quarks and cascade c -quarks semi-leptonic decay products, as muons or neutrinos, not included in the definition of the true particle jet. The effect on the measurement of m_t due to scaling only the b -jet energy of 7% can be estimated by considering that the maximum shift in m_t corresponding to scaling the b -jet energy of 2.5% is 1.6 GeV. This translates into a shift of about (-)4.5 GeV for a scaling of (-)7%, which is comparable to the shift of (-)4.7 GeV given by the pull distribution.

The bias estimated from the pull distribution has to be accounted for in order to measure the top quark mass with the method presented in this thesis. In first approximation, the bias can be added as:

$$m_t^f = m_t + k , \quad (5.8)$$

where m_t^f is the final top quark mass, m_t is the result of the fitting procedure and $k = 4.7$ GeV is the bias estimated from the pull distribution. This equation derives from the pull variable definition if $m_t^f = m_t^{MC}$. In order to apply the correction in a form that is as more independent as possible from the specific value of m_t^{MC} used to estimate the bias, the final top quark mass can be obtained as:

$$m_t^f = m_t \cdot \left(1 + \frac{k}{m_t^{MC}}\right) . \quad (5.9)$$

Equation 5.9 can be obtained from Equation 5.8 for small values of the ratio k/m_t^{MC} , which is a valid approximation for the values of k and m_t^{MC} considered.

The dependency of Equation 5.9 and 5.8 from m_t^{MC} can be studied by using kinematical arguments in the top quark rest frame. The bias on the top quark mass due to the b -jet energy scale can be written as $k = j_b \cdot f_b \cdot m_t^{MC}$, where j_b is the b -jet energy scale offset (7%) that is independent of the top quark mass and f_b is the fraction of the top quark energy carried by the b -quark. The factor f_b depends on the top quark

mass as:

$$f_b = \frac{(m_t^{MC})^2 - (m_W^{MC})^2}{2 \cdot (m_t^{MC})^2} , \quad (5.10)$$

where m_W^{MC} is the W boson mass and the b -quark mass is neglected, because it is very small with respect to m_t and m_W . The dependency of the ratio k/m_t^{MC} on m_t^{MC} is only due to the factor f_b and is very weak. Therefore Equation 5.9 can be applied to correct for the b -jet energy scale bias, by introducing only a very weak dependency on the specific value of m_t^{MC} used in the Monte Carlo simulations. A more sophisticated correction method can be studied with Monte Carlo simulations obtained for different values of m_t^{MC} , which were not available for the studies presented in this thesis.

After correcting for the b -jet energy scale bias, the measured top quark mass in the typical pseudo-experiment considered above is:

$$m_t = 173.4 \pm 2.1|_{stat} \pm 7.3|_{sys} \text{ GeV} . \quad (5.11)$$

It is possible to say that the result obtained with the method described is compatible with the true top quark Monte Carlo mass and that the method can be used on ATLAS data. The precision of the method can be further improved by including dedicated b -jet energy corrections and by providing a better jet energy scale precision.

The analysis presented in this Chapter is one of the very few studies [106] [107] on the $t\bar{t}$ all-hadronic channel using the ATLAS detector. This study definitely proves the feasibility of the measurement and sets the guidelines for performing it on real data. The top quark mass measurement in the $t\bar{t}$ all-hadronic channel has not been possible with very first data, because of the lack of precision of the b -tagging algorithm and because of the low integrated luminosity collected (35 pb⁻¹ at 7 TeV at the moment of writing). Instead, the prospects for data taking in 2011 are very promising: the performance of the b -tagging algorithm is being refined and the excellent performance of the LHC machine encourage to think that sufficient data can be collected to make this measurement possible.

Conclusions

In this thesis two main topics were addressed. Studies on the jet energy calibration with Local Hadron Calibration and studies on the top quark mass measurement in the $t\bar{t}$ all-hadronic channel were presented. The two subjects of study are intrinsically related by the fact that the precision on the top quark mass measurement is mainly limited by the uncertainty on the jet energy scale.

The performance of the Local Hadron Calibration was studied with data and with Monte Carlo simulations. In both cases the focus was put on the cluster level corrections. The performance for jet energy reconstruction was evaluated with respect to the true particle jet. For a typical jet of 100 GeV in the barrel region, the energy linearity was found to be within 10% after cluster corrections. This figure suggested the need for jet level corrections, which were developed in parallel to this work. A study on the systematic uncertainty on the jet energy scale after cluster level corrections was performed. The uncertainty on the hadronic shower description and on the dead material description led to a combined 4% systematic uncertainty. In order to evaluate the improvement in resolution due to the cluster level corrections, the residual nonlinear effects were removed for each cluster correction for comparing them on equal basis. For a typical jet of 100 GeV in the barrel region, the cluster corrections were found to improve the jet energy resolution by 12% with respect to the electromagnetic scale. Studies on the energy linearity with respect to the true cluster energy, as defined from GEANT4 simulation information, were shown. This type of comparison was found to be useful to study the different cluster corrections in a modular way.

The potential of the Local Hadron Calibration in reconstructing Missing Transverse Energy (MET) was studied as well. By considering only the calorimeter term calibrated with Local Hadron Calibration at the cluster level and the muon term, the MET linearity was found to be better than 8%. With the addition of MET terms depending on the jet level corrections and on the optimized calibration of e , γ and τ , this figure

can be improved.

Validation studies were performed for the cluster level corrections on minimum bias data collected for pp collisions at a centre of mass energy of $\sqrt{s} = 900$ GeV. The cluster energy was compared at the electromagnetic scale and after each cluster correction, between data and Monte Carlo simulations. The Monte Carlo simulations were found to describe the data very well: inside $\approx 2\%$ in the central region and inside $\approx 4\%$ in the end-cap and forward region. Further tests in this direction are ongoing in order to validate the jet level corrections using multi-jet events. By performing these studies with an increasing amount of integrated luminosity of data, it will be possible to correct the Monte Carlo simulations in order to obtain the jet energy scale accuracy of 1% desired by the ATLAS physics programme.

The prospects for measuring the top quark mass in the $t\bar{t}$ all-hadronic channel with the ATLAS detector were investigated. The study was performed on Monte Carlo simulations for pp collisions at a centre of mass energy of 10 TeV, considering 200 pb^{-1} of integrated luminosity. A cut based event selection was optimized with respect to the signal significance. The final event selection was based on a set of topological variables and on the request of two b -tagged jets. The event selection was found to improve the S/B fraction from 10^{-4} to $2.8 \cdot 10^{-1}$, by keeping a signal efficiency of 6%. The reconstruction of the top quark invariant mass was performed by calculating all possible combinations of 6(7) jets in groups of 3, accounting for the b -tagging information. Among the possible combinations, the top quark candidate was chosen as the combination with the largest transverse momentum p_T . This criterion showed a purity of 38% in selecting the right combination in comparison to a 12% purity showed by a random choice. A method was developed to extract the shape of the invariant mass distribution for the QCD multi-jet background after the final event selection by making use of the invariant mass distribution obtained without b -tagging requirements. A χ^2 fitting procedure was then developed on typical pseudo-experiment distributions of the top quark candidate invariant mass, in order to extract the measured top quark mass. The systematic uncertainty on this measurement was assessed by considering the uncertainty deriving from the background shape extraction method, the background normalisation, the jet and b -jet energy scale and the b -tagging efficiency. The final uncertainty was found to be 7.3 GeV with the jet energy scale uncertainty as the dominating source. The validity of the method was then tested with respect to the true top quark mass $m_t^{MC} = 172.5$ GeV with the use of a pull distribution.

The width of the pull distribution was found to be consistent with 1, proving that the statistical error on the measurement was correctly calculated by the fitting procedure. The pull distribution showed a shift corresponding to a bias of $k = -4.7$ GeV that was interpreted in terms of an offset of the b -jet energy scale. After correcting for this bias, the result for the measured top quark mass for a typical pseudo experiment was found to be:

$$m_t = 173.4 \pm 2.1|_{stat} \pm 7.3|_{sys} \text{ GeV} .$$

This result is compatible with the true top quark mass value $m_t^{MC} = 172.5$ GeV. The precision of the measurement can be further improved by reducing the uncertainty on the jet energy scale and by developing dedicated b -jet energy corrections. The uncertainty on the background shape and normalisation can be reduced by measuring them on data directly. Finally, with the use of Monte Carlo simulations for different values of the true top quark mass value m_t^{MC} , a more sophisticated method to calibrate the measurement of the top quark mass m_t with respect to m_t^{MC} can be studied.

This study definitely proves the feasibility of the top quark mass measurement in the $t\bar{t}$ all-hadronic channel with the ATLAS detector and sets the guidelines for performing it on real data. This measurement has not been possible with very first data, because of the lack of precision of the b -tagging algorithm and because of the low integrated luminosity collected (35 pb^{-1} at 7 TeV at the moment of writing). Instead, the prospects for data taking in 2011 are very promising: the performance of the b -tagging algorithm is being refined and the excellent performance of the LHC machine encourages to think that sufficient data can be collected to make this measurement possible.

Appendix A

Derivation of resolution relations

In Chapter 4 the problem of how the energy resolution changes with nonlinear energy corrections is discussed. In this Appendix the details of how this effect can be explained in terms of error propagation are presented.

Let's consider a function f such that:

$$y = f(x) , \quad (\text{A.1})$$

then if $f(x)$ is derivable, the law of error propagation states that [98]:

$$\sigma_y = \frac{df(x)}{dx} \cdot \sigma_x , \quad (\text{A.2})$$

where σ_y indicates the error on y and σ_x the error on x . The absolute energy resolution σ is the estimation of the error on the energy measurement and thus is subject to the rules of error propagation. Recalling that E^T indicates the true energy, E^M the energy measured in the calorimeter, E^C the energy corrected for nonlinear response, σ^M and σ^C the errors on the measurement of E^M and E^C respectively, it is possible to define:

$$\begin{aligned} E^M &= s(E^T) \cdot E^T , \\ E^C &= w(E^M) \cdot E^M , \end{aligned} \quad (\text{A.3})$$

where $s(E^T)$ is the calorimeter response function and $w(E^M)$ is the calibration function. Then, by applying the law of error propagation to the equation for E^C , it is possible to write:

$$\begin{aligned} \sigma^C &= \frac{d(w(E^M) \cdot E^M)}{dE^M} \cdot \sigma^M \\ &= (w(E^M) + E^M \cdot \frac{dw(E^M)}{dE^M}) \cdot \sigma^M . \end{aligned} \quad (\text{A.4})$$

Dividing the second expression in Equation A.4 by $E^C = w(E^M) \cdot E^M$, the resolution for the corrected energy reads:

$$\frac{\sigma^C}{E^C} = \left(1 + \frac{E^M}{w(E^M)} \cdot \frac{dw(E^M)}{dE^M} \right) \cdot \frac{\sigma^M}{E^M} . \quad (\text{A.5})$$

From Equation A.5 (Equation 4.2 in Chapter 4) it is possible to see that the resolution of the measured energy and the resolution of the corrected energy are related by a factor that depends on the derivative of the correction function w .

Equation A.5 contains the full relation between the resolution before and after nonlinear energy corrections are applied. Nevertheless it is not useful in performance studies, because it is not expressed in terms of the true energy E^T . This can easily be done in few steps. Let's consider the theorem of the derivative of the inverse of a function [108]. Let's consider a function f , defined in an interval I , f being continuous and strictly monotonic, thus invertible. Let's consider a point c , belonging to the interval I . If f is derivable in c , with $D(f(c)) \neq 0$, then the inverse function is derivable in the point $d = f(c)$ and:

$$\begin{aligned} D(f^{-1}(f(c))) &= \frac{1}{Df(c)} , \\ D(f^{-1}(d)) &= \frac{1}{Df(f^{-1}(d))} . \end{aligned} \quad (\text{A.6})$$

Going back to Equation A.3, it is possible to introduce the function f such that:

$$\begin{aligned} E^M &= s(E^T) \cdot E^T \equiv f(E^T) , \\ E^C &= w(E^M) \cdot E^M \equiv f^{-1}(E^M) , \end{aligned} \quad (\text{A.7})$$

where the equivalence $E^C = E^T$ is implicit and is valid in the limit for which E^C is the best experimental knowledge of E^T . Dividing the first expression of Equation A.4 by $E^C = w(E^M) \cdot E^M$, it is possible to write:

$$\begin{aligned} \frac{\sigma^C}{E^C} &= \frac{d(w(E^M) \cdot E^M)}{dE^M} \cdot \frac{1}{w(E^M) \cdot E^M} \cdot \sigma^M \\ &= \frac{df^{-1}(E^M)}{dE^M} \cdot \frac{1}{f^{-1}(E^M)} \cdot \sigma^M \\ &= \frac{df^{-1}(E^M)}{dE^M} \cdot \frac{1}{f^{-1}(E^M)} \cdot E^M \cdot \frac{\sigma^M}{E^M} . \end{aligned} \quad (\text{A.8})$$

Applying the theorem of the derivative of the inverse of a function and changing variable

into E^T , Equation A.8 becomes:

$$\frac{\sigma^C}{E^C} = \frac{1}{\frac{df(E^T)}{dE^T}} \cdot \frac{f(E^T)}{E^T} \cdot \frac{\sigma^M}{E^M}, \quad (\text{A.9})$$

and in terms of the response function $s(E^T)$:

$$\frac{\sigma^C}{E^C} = \frac{s(E^T)}{s(E^T) + \frac{ds(E^T)}{dE^T} \cdot E^T} \cdot \frac{\sigma^M}{E^M}. \quad (\text{A.10})$$

Equation A.10 (Equation 4.3 in Chapter 4) sets an analytical correspondence between the measured and corrected energy resolution, in terms of the true energy E^T . If the response function s is not known analytically, it can be useful to write a discrete version of Equation A.10 by exploiting the incremental definition of the derivative of a function:

$$\frac{\sigma^C}{E^C} = \frac{s(E^T) \cdot \Delta E^T}{s(E^T + \Delta E^T) \cdot (E^T + \Delta E^T) - s(E^T) \cdot E^T} \cdot \frac{\sigma^M}{E^M}. \quad (\text{A.11})$$

Equation A.11 (Equation 4.4 in Chapter 4) can easily be implemented by approximating $\Delta E^T \sim \frac{\sigma^M}{E^M} \cdot E^T$.

Bibliography

- [1] E. Hobsbawm, *Il Secolo breve - 1914-1991*. Rizzoli, 1995. Translation of Brunello Lotti. Original title: Age of Extremes, the Short Twentieth Century 1914-1991.
- [2] M. Kobayashi and T. Maskawa, *CP Violation in the Renormalizable Theory of Weak Interaction*, *Prog. Theor. Phys.* **49** (1973) 652–657.
- [3] **CDF** Collaboration, F. Abe *et. al.*, *Observation of top quark production in $p\bar{p}$ collisions with the collider detector at fermilab*, *Phys. Rev. Lett.* **74** (Apr, 1995) 2626–2631.
- [4] **D0** Collaboration, S. Abachi *et. al.*, *Observation of the top quark*, *Phys. Rev. Lett.* **74** (Apr, 1995) 2632–2637.
- [5] **Particle Data Group** Collaboration, K. Nakamura, *Review of particle physics*, *J. Phys.* **G37** (2010) 075021.
- [6] G. Rajasekaran, *Are Neutrinos Majorana Particles?*, [arXiv:0803.4387](https://arxiv.org/abs/0803.4387).
- [7] S. Weinberg, *A Model of Leptons*, *Phys. Rev. Lett.* **19** (1967) 1264–1266.
- [8] A. Salam, *Weak and Electromagnetic Interactions*, . Originally printed in *Svartholm: Elementary Particle Theory, Proceedings Of The Nobel Symposium Held 1968 At Lerum, Sweden*, Stockholm 1968, 367-377.
- [9] S. L. Glashow, *Partial Symmetries of Weak Interactions*, *Nucl. Phys.* **22** (1961) 579–588.
- [10] S. L. Glashow, J. Iliopoulos, and L. Maiani, *Weak Interactions with Lepton-Hadron Symmetry*, *Phys. Rev.* **D2** (1970) 1285–1292.

- [11] P. W. Higgs, *Broken symmetries, massless particles and gauge fields*, *Phys. Lett.* **12** (1964) 132–133.
- [12] P. W. Higgs, *Broken symmetries and the masses of gauge bosons*, *Phys. Rev. Lett.* **13** (1964) 508–509.
- [13] P. W. Higgs, *Spontaneous Symmetry Breakdown Without Massless Bosons*, *Phys. Rev.* **145** (1966) 1156–1163.
- [14] F. Englert and R. Brout, *Broken symmetry and the mass of gauge vector mesons*, *Phys. Rev. Lett.* **13** (1964) 321–322.
- [15] T. W. B. Kibble, *Symmetry breaking in non-Abelian gauge theories*, *Phys. Rev.* **155** (1967) 1554–1561.
- [16] R. P. Feynman, *Space-time approach to quantum electrodynamics*, *Phys. Rev.* **76** (1949) 769–789.
- [17] R. P. Feynman, *Mathematical formulation of the quantum theory of electromagnetic interaction*, *Phys. Rev.* **80** (1950) 440–457.
- [18] D. J. Gross and F. Wilczek, *Asymptotically Free Gauge Theories. 1*, *Phys. Rev.* **D8** (1973) 3633–3652.
- [19] D. J. Gross and F. Wilczek, *Ultraviolet behavior of non-Abelian gauge theories*, *Phys. Rev. Lett.* **30** (1973) 1343–1346.
- [20] D. J. Gross and F. Wilczek, *Asymptotically free gauge theories. 2*, *Phys. Rev.* **D9** (1974) 980–993.
- [21] O. W. Greenberg, *Spin and Unitary Spin Independence in a Paraquark Model of Baryons and Mesons*, *Phys. Rev. Lett.* **13** (1964) 598–602.
- [22] H. D. Politzer, *Reliable perturbative results for strong interactions?*, *Phys. Rev. Lett.* **30** (1973) 1346–1349.
- [23] H. Fritzsch, M. Gell-Mann, and H. Leutwyler, *Advantages of the Color Octet Gluon Picture*, *Phys. Lett.* **B47** (1973) 365–368.
- [24] T. Morii, L. C. S, and S. N. Mukherjee, *The physics of the standard model and beyond*. World Scientific, Singapore, 2004.

- [25] S. Willenbrock, *The Standard model and the top quark*, hep-ph/0211067.
- [26] N. Cabibbo, *Unitary Symmetry and Leptonic Decays*, *Phys. Rev. Lett.* **10** (1963) 531–533.
- [27] S. Bethke, *The 2009 World Average of $\alpha(s)$* , *Eur.Phys.J.* **C64** (2009) 689–703, [0908.1135].
- [28] P. Langacker, *The standard model and beyond*. High Energy Physics, Cosmology and Gravitation. Taylor and Francis, Boca Raton, FL, 2010.
- [29] J. D. Lykken, *Beyond the Standard Model*, arXiv:1005.1676.
- [30] J. R. Ellis, *Beyond the standard model with the LHC*, *Nature* **448** (2007) 297–301.
- [31] J. R. Incandela, A. Quadt, W. Wagner, and D. Wicke, *Status and Prospects of Top-Quark Physics*, *Prog. Part. Nucl. Phys.* **63** (2009) 239–292, [arXiv:0904.2499].
- [32] **D0** Collaboration, V. Abazov *et. al.*, *Experimental discrimination between charge $2e/3$ top quark and charge $4e/3$ exotic quark production scenarios*, *Phys. Rev. Lett.* **98** (Jan, 2007) 041801.
- [33] P. M. Nadolsky, H.-L. Lai, Q.-H. Cao, J. Huston, J. Pumplin, D. Stump, W.-K. Tung, and C.-P. Yuan, *Implications of cteq global analysis for collider observables*, *Phys. Rev. D* **78** (Jul, 2008) 013004.
- [34] M. R. Whalley, “Pdf generator.”
<http://durpdg.dur.ac.uk/hepdata/pdf3.html>.
- [35] **CDF** Collaboration, T. Aaltonen *et. al.*, *Observation of electroweak single top-quark production*, *Phys. Rev. Lett.* **103** (Aug, 2009) 092002.
- [36] **D0** Collaboration, V. Abazov *et. al.*, *Observation of single top-quark production*, *Phys. Rev. Lett.* **103** (Aug, 2009) 092001.
- [37] R. Bonciani, S. Catani, M. L. Mangano, and P. Nason, *NLL resummation of the heavy-quark hadroproduction cross-section*, *Nucl. Phys.* **B529** (1998) 424–450, [hep-ph/9801375].

- [38] N. Kidonakis, *Higher-order soft gluon corrections in single top quark production at the cern lhc*, *Phys. Rev. D* **75** (Apr, 2007) 071501.
- [39] A. H. Hoang and I. W. Stewart, *Top Mass Measurements from Jets and the Tevatron Top-Quark Mass*, *Nucl. Phys. Proc. Suppl.* **185** (2008) 220–226, [arXiv:0808.0222].
- [40] S. Agostinelli *et al.*, *Geant4 a simulation toolkit*, *Nucl. Instr. and Meth. A* **506** (2003), no. 3 250 – 303.
- [41] M. L. Mangano, *Qcd tools for the lhc*, Tech. Rep. hep-ph/0312117. CERN-TH-2003-303, Dec, 2003.
- [42] T. Sjostrand, *Monte Carlo Tools*, arXiv:0911.5286.
- [43] R. K. Ellis, W. J. Stirling, and B. R. Webber, *QCD and Collider Physics*. Cambridge monographs on particle physics, nuclear physics, and cosmology. Cambridge Univ. Press, Cambridge, 2003. Photography by S. Vascotto.
- [44] T. Sjostrand, *High-energy physics event generation with PYTHIA 5.7 and JETSET 7.4*, *Comput. Phys. Commun.* **82** (1994) 74–90.
- [45] G. Marchesini, B. Webber, G. Abbiendi, I. Knowles, M. Seymour, *et al.*, *HERWIG: A Monte Carlo event generator for simulating hadron emission reactions with interfering gluons. Version 5.1 - April 1991*, *Comput.Phys.Commun.* **67** (1992) 465–508.
- [46] M. L. Mangano, M. Moretti, F. Piccinini, R. Pittau, and A. D. Polosa, *ALPGEN, a generator for hard multiparton processes in hadronic collisions*, *JHEP* **07** (2003) 001, [hep-ph/0206293].
- [47] S. Catani, F. Krauss, R. Kuhn, and B. Webber, *QCD matrix elements + parton showers*, *JHEP* **0111** (2001) 063, [hep-ph/0109231].
- [48] J. Alwall, S. Hoeche, F. Krauss, N. Lavesson, L. Lonnblad, *et al.*, *Comparative study of various algorithms for the merging of parton showers and matrix elements in hadronic collisions*, *Eur.Phys.J.* **C53** (2008) 473–500, [0706.2569].
- [49] S. Frixione and B. R. Webber, *Matching NLO QCD computations and parton shower simulations*, *JHEP* **0206** (2002) 029, [hep-ph/0204244].

- [50] *ATLAS detector and physics performance: Technical Design Report, 1.* Technical Design Report ATLAS. CERN, Geneva, 1999.
- [51] *ATLAS detector and physics performance: Technical Design Report, 2.* Technical Design Report ATLAS. CERN, Geneva, 1999.
- [52] **ATLAS** Collaboration, G. Aad *et. al.*, *The ATLAS Experiment at the CERN Large Hadron Collider*, *JINST* **3** (2008) S08003.
- [53] E. Bruning, Oliver S., E. Collier, P., E. Lebrun, P., E. Myers, S., E. Ostojic, R., *et. al.*, *LHC Design Report. 1. The LHC Main Ring*, .
- [54] E. Buning, O., E. Collier, P., E. Lebrun, P., E. Myers, S., E. Ostojic, R., *et. al.*, *LHC Design Report. 2. The LHC infrastructure and general services*, .
- [55] E. Benedikt, M., E. Collier, P., E. Mertens, V., E. Poole, J., and E. Schindl, K., *LHC Design Report. 3. The LHC injector chain*, .
- [56] **ALICE** Collaboration, K. Aamodt *et. al.*, *The ALICE experiment at the CERN LHC*, *JINST* **3** (2008) S08002.
- [57] **CMS** Collaboration, R. Adolphi *et. al.*, *The CMS experiment at the CERN LHC*, *JINST* **3** (2008) S08004.
- [58] **LHCb** Collaboration, A. Alves *et. al.*, *The LHCb Detector at the LHC*, *JINST* **3** (2008) S08005.
- [59] C. Eck *et. al.*, *LHC computing Grid: Technical Design Report. Version 1.06 (20 Jun 2005)*. Technical Design Report LCG. CERN, Geneva, 2005.
- [60] “Worldwide lhc computing grid.” <http://lcg.web.cern.ch/LCG/Default.htm>.
- [61] K. Harrison, W. Lavrijsen, C. Tull, P. Mato, A. Soroko, *et. al.*, *GANGA: A User Grid interface for Atlas and LHCb*, *cs/0306085*.
- [62] G. P. Salam, *Towards Jetography*, *Eur.Phys.J.* **C67** (2010) 637–686, [[arXiv:0906.1833](https://arxiv.org/abs/0906.1833)].
- [63] G. P. Salam and G. Soyez, *A Practical Seedless Infrared-Safe Cone jet algorithm*, *JHEP* **0705** (2007) 086, [[arXiv:0704.0292](https://arxiv.org/abs/0704.0292)].

- [64] M. Cacciari and G. P. Salam, *Dispelling the N^{*3} myth for the $k(t)$ jet-finder*, *Phys.Lett.* **B641** (2006) 57–61, [[hep-ph/0512210](#)].
- [65] M. C. G. P. Salam and G. Soyez, “Fastjet.”
<http://www.lpthe.jussieu.fr/salam/fastjet/>.
- [66] S. Catani, Y. L. Dokshitzer, M. H. Seymour, and B. R. Webber, *Longitudinally invariant K_t clustering algorithms for hadron hadron collisions*, *Nucl. Phys.* **B406** (1993) 187–224.
- [67] S. D. Ellis and D. E. Soper, *Successive combination jet algorithm for hadron collisions*, *Phys.Rev.* **D48** (1993) 3160–3166, [[hep-ph/9305266](#)].
- [68] Y. L. Dokshitzer, G. Leder, S. Moretti, and B. Webber, *Better jet clustering algorithms*, *JHEP* **9708** (1997) 001, [[hep-ph/9707323](#)].
- [69] M. Wobisch and T. Wengler, *Hadronization corrections to jet cross-sections in deep inelastic scattering*, [hep-ph/9907280](#).
- [70] M. Cacciari, G. P. Salam, and G. Soyez, *The anti- $k(t)$ jet clustering algorithm*, *JHEP* **04** (2008) 063, [[arXiv:0802.1189](#)].
- [71] ATLAS Jet MET performance group, Private communication, 2010.
- [72] **ATLAS** Collaboration, T. Barillari *et. al.*, *Local hadronic calibration*, .
ATL-LARG-PUB-2009-001.
- [73] S. Agostinelli *et. al.*, *Geant4 a simulation toolkit*, *Nucl. Instr. and Meth. A* **506** (2003), no. 3 250 – 303.
- [74] R. Wigmans, *On the energy resolution of uranium and other hadron calorimeters.*, *Nucl. Instrum. Methods Phys. Res., A* **259** (Sep, 1986) 389–429.
106 p.
- [75] R. K. Bock and A. Vasilescu, *The Particle Detector Briefbook*. Accelerator Physics. Springer, Berlin, 1998.
- [76] **ATLAS** Collaboration, *Expected Performance of the ATLAS Experiment - Detector, Trigger and Physics*, [arXiv:0901.0512](#).

- [77] **ATLAS** Collaboration, *Readiness of the ATLAS Liquid Argon Calorimeter for LHC Collisions*, *Eur. Phys. J. C* (2010) [[arXiv:0912.2642](#)].
- [78] **ATLAS** Collaboration, *Readiness of the ATLAS Tile Calorimeter for LHC collisions*, [arXiv:1007.5423](#).
- [79] W. Lampl *et. al.*, *Calorimeter clustering algorithms: Description and performance*, . ATL-LARG-PUB-2008-002.
- [80] G. Pospelov. Private communication, 2010.
- [81] *Jet energy scale and its systematic uncertainty for jets produced in proton-proton collisions at $\sqrt{s} = 7$ tev and measured with the atlas detector*, Tech. Rep. ATLAS-CONF-2010-056, CERN, Geneva, Jul, 2010.
- [82] *Inputs to jet reconstruction and calibration with the atlas detector using proton-proton collisions at $\sqrt{s} = 900$ gev*, Tech. Rep. ATLAS-CONF-2010-016. ATLAS-COM-CONF-2010-016, CERN, Geneva, Jul, 2010.
- [83] K. Grahn, A. Kiryunin, and G. Pospelov, *Tests of local hadron calibration approaches in atlas combined beam tests*, Tech. Rep. ATL-LARG-PROC-2010-011, CERN, Geneva, Sep, 2010.
- [84] A. Jantsch, *Studies on the top quark mass measurement in the $t\bar{t}$ semi-leptonic channel with ATLAS*. PhD thesis, Technische Universität München, Work in progress.
- [85] G. Folger and J. Wellisch, *String parton models in GEANT4*, [nucl-th/0306007](#).
- [86] H. W. Bertini, *Intranuclear-cascade calculation of the secondary nucleon spectra from nucleon-nucleus interactions in the energy range 340 to 2900 mev and comparisons with experiment*, *Phys. Rev.* **188** (Dec, 1969) 1711–1730.
- [87] E. Abat *et. al.*, *Response and shower topology of 2 to 180 gev pions measured with the atlas barrel calorimeter at the cern test-beam and comparison to monte carlo simulations*, Tech. Rep. ATL-CAL-PUB-2010-001, CERN, Geneva, May, 2010.
- [88] P. Adragna *et. al.*, *Measurement of pion and proton response and longitudinal shower profiles up to 20 nuclear interaction lengths with the atlas tile*

- calorimeter, Nucl. Instrum. Methods Phys. Res., A* **615** (Oct, 2009) 158–181. 60 p.
- [89] E. Abat *et. al.*, *Study of the response of the atlas central calorimeter to pions of energies from 3 to 9gev, Nuclear Instruments and Methods in Physics Research Section A: Accelerators, Spectrometers, Detectors and Associated Equipment* **607** (2009), no. 2 372 – 386.
- [90] J. Pinfeld *et. al.*, *Performance of the atlas liquid argon endcap calorimeter in the pseudorapidity region $2.5 < [\eta] < 4.0$ in beam tests, Nuclear Instruments and Methods in Physics Research Section A: Accelerators, Spectrometers, Detectors and Associated Equipment* **593** (2008), no. 3 324 – 342.
- [91] D. Gingrich *et. al.*, *Construction, assembly and testing of the atlas hadronic end-cap calorimeter*, Tech. Rep. ATL-LARG-PUB-2007-009. CERN-ATL-COM-LARG-2007-006, CERN, Geneva, Apr, 2007.
- [92] B. Andersson, G. Gustafson, and B. Nilsson-Almqvist, *A model for low- p_T hadronic reactions with generalizations to hadron-nucleus and nucleus-nucleus collisions, Nuclear Physics B* **281** (Jan., 1987) 289–309.
- [93] G. Unal. Private communication, 2010.
- [94] *Atlas monte carlo tunes for mc09*, Tech. Rep. ATL-PHYS-PUB-2010-002. ATL-COM-PHYS-2010-033, CERN, Geneva, Mar, 2010.
- [95] **ATLAS** Collaboration, G. Aad *et. al.*, *Measurement of the top quark-pair production cross section with ATLAS in pp collisions at $\sqrt{s} = 7$ TeV*, arXiv:1012.1792.
- [96] S. Moch and P. Uwer, *Theoretical status and prospects for top-quark pair production at hadron colliders, Phys.Rev.* **D78** (2008) 034003, [arXiv:0804.1476].
- [97] E. W. Weisstein, “Legendre polynomial.” <http://mathworld.wolfram.com/LegendrePolynomial.html>.
- [98] R. J. Barlow, *Statistics: a guide to the use of statistical methods in the physical sciences*. Manchester physics series. Wiley, Chichester, 1989.

- [99] P. J. Olver and C. Shakiban, *Applied linear algebra*. Prentice-Hall, Upper Saddle River, NJ, 2006.
- [100] W. T. Eadie, D. Drijard, F. E. James, M. Roos, and B. Sadoulet, *Statistical methods in experimental physics*. North-Holland, Amsterdam, 1971.
- [101] E. W. Weisstein, “Gram-schmidt orthonormalization.”
<http://mathworld.wolfram.com/Gram-SchmidtOrthonormalization.html>.
- [102] E. W. Weisstein, “Chebyshev polynomial of the first kind.” <http://mathworld.wolfram.com/ChebyshevPolynomialoftheFirstKind.html>.
- [103] G. Cortiana and R. Nisius, *Measurement of the top-quark mass using the stabilized mass variable via the template method in the $t\bar{t}$ lepton+jets channel at atlas*, Tech. Rep. ATL-PHYS-INT-2010-027, CERN, Geneva, Mar, 2010.
- [104] A. Quadt, *Top quark physics at hadron colliders*, *The European Physical Journal C - Particles and Fields* **48** (2006) 835–1000. 10.1140/epjc/s2006-02631-6.
- [105] L. Demortier and L. Lyons, “Everything you always wanted to know about pulls.” http://www-cdf.fnal.gov/publications/cdf5776_pulls.ps.gz.
- [106] M. Lambacher, *Study of fully hadronic $t\bar{t}$ decays and their separation from QCD multijet background events in the first year of the ATLAS experiment*. PhD thesis, Ludwig-Maximilians-Universität München, July 2007.
- [107] K. Edmonds, *Prospects for top quark mass measurement through the fully hadronic decay of top-antitop events with the atlas detector*, Master’s thesis, University of Victoria, 2007.
- [108] E. Giusti, *Analisi Matematica 1*. Bollati Boringhieri, 1996.